creative commons
COMMONS DEED

저작자표시-비영리-변경금지 2.0 대한민국

이용자는 아래의 조건을 따르는 경우에 한하여 자유롭게

- 이 저작물을 복제, 배포, 전송, 전시, 공연 및 방송할 수 있습니다.

다음과 같은 조건을 따라야 합니다:

저작자표시. 귀하는 원저작자를 표시하여야 합니다.

비영리. 귀하는 이 저작물을 영리 목적으로 이용할 수 없습니다.

변경금지. 귀하는 이 저작물을 개작, 변형 또는 가공할 수 없습니다.

- 귀하는, 이 저작물의 재이용이나 배포의 경우, 이 저작물에 적용된 이용허락조건을 명확하게 나타내어야 합니다.
- 저작권자로부터 별도의 허가를 받으면 이러한 조건들은 적용되지 않습니다.

저작권법에 따른 이용자의 권리는 위의 내용에 의하여 영향을 받지 않습니다.

이것은 이용허락규약(Legal Code)을 이해하기 쉽게 요약한 것입니다.

Disclaimer

dCollection

理 學 碩 士 學 位 論 文

Studies on environment-friendly catalytic reactions through combined experimental and computational approaches

(친환경적인 촉매 반응에 대한 실험 및 전산 연구)

蔚 山 大 學 校 大 學 院

化 學 科

朴 世 訓

Studies on environment-friendly catalytic reactions through combined experimental and computational approaches.

指 導 敎 授 정 재 훈

指 導 敎 授 우 상 국

이 論文을 理學碩士 學位 論文으로 제출함

2022年 2月

蔚 山 大 學 校 大 學 院

化 學 科

朴 世 訓

朴 世 訓의 理學碩士 學位 論文을 認准함

審査委員 김 범 진 印

審査委員 우 상 국 印

審査委員 정 재 훈 印

蔚 山 大 學 校 大 學 院

2022年 2月

Contents

. *Abstract*

Green chemistry is a relatively new field working at the molecular level to achieve sustainability. This field has received widespread attention over the past two decades due to its ability to leverage chemical innovations to simultaneously achieve environmental and economic goals. Among them, organic experiments using eco-friendly catalysts are being actively conducted, and through this, the use of substances harmful to the environment and strong toxicity is reduced, and desired products are made without using high temperature and high pressure conditions. Based on these goals, we conducted two eco-friendly studies.

We conducted a study to increase the economic value of the simultaneous conversion of CO_2 by designing a high-efficiency catalyst, a study to synthesize oxaziridines into amides under eco-friendly conditions using a photocatalyst, and obtained experimental data from the designed study through organic experiments. Data on the reaction mechanism and catalyst efficiency were obtained through computational experiments.

In the CO_2 conversion experiment, a reaction in which C1 source and glycerol are simultaneously converted to formic acid and lactic acid, respectively, was studied using a catalyst combining bis-Carbene ligand with an Ir(I) atom. The reaction mechanism in which β-hydride elimination occurs by catalytic transfer hydrogenation was identified through computational research, and usable formic acid and lactic acid, respectively, were obtained in high yield using reusable C1 source and waste glycerol.

In the oxaziridines to amides experiment, amides were produced by selective rearrangement of oxaziridine under eco-friendly conditions using Acr^+-Mes visible light photocatalyst under weak-base conditions. What happens was found through the calculation of reaction energy and pKa through control experiment and DFT calculation, and the related reaction mechanism was studied. Based on this, we succeeded in synthesizing amides with various functional groups in good yield.

2. Introduction

2.1. Rearrangement of Oxaziridines to Amides

Oxaziridines are three-membered heterocyclic compounds comprising oxygen, nitrogen, and carbon atoms with an electronegativity difference in the ring.[1] Oxaziridines are useful in organic synthesis because they can be easily prepared and used for various reactions. Their reactivity is derived from the presence of two electronegative heteroatoms in a strained three-membered ring. Oxaziridines are typically employed as electrophilic oxygen- and nitrogen-atom transfer reagents and are converted into nitrones, amides, imines, aldehydes, and ketones via rearrangement. The reactions of oxaziridines involve ring-opening by C–O, C–N, and N–O bond cleavage. In particular, the selective rearrangement of oxaziridines to amides is crucial for exploring a "green method" for producing various high-value amide compounds[2] from an atom economy perspective. Recently, photo or electrochemical methods have been reported for amides synthesis from aldehydes and amines.[3] However, green methods for the rearrangement of oxaziridines to amides require further development. Amides are formed by selective N–O bond cleavage instead of the C–O bond cleavage of oxaziridines (Scheme 1a). The selective rearrangements of oxaziridines to amides have been developed using photo,[4] thermal,[5] Lewis or Brønsted–Lowry acid–base,[6] and transition metal reagents[7] or catalysts.[8] Moreover, considerable efforts have been devoted to devise ecofriendly synthesis methods that address the problems encountered in conventional methods, such as the use of toxic and expensive reagents, the consumption of excess quantities of reagents, and the generation of waste. A photoinduced reaction is a potential route for developing green methods for synthesizing versatile compounds by inducing the rearrangement of oxaziridines. The rearrangement of oxaziridines to both nitrones and amides has been developed in classical photochemistry. A single electron transfer (SET) mechanism using photosensitizers has been employed to synthesize nitrones by the C–O bond cleavage of oxaziridines[9], and homolytic N–O bond cleavage in photoexcited oxaziridines under ultraviolet irradiation was exploited to produce amides.[10] However, the previously reported photoinduced reactions should be improved to overcome weak features, such as low conversion and yield, narrow substrate

scope, and ultraviolet (UV) as a light source for photoreactions. Visible-light photoredox catalysis as an alternative to traditional photochemistry is attracting attention.[11] Visible light is an inexpensive, infinite, and clean energy source; thus, reaction conditions are mild with good functional group tolerance. Recently, we developed a visible-light photoredox catalyzed [3+2] cycloaddition of oxaziridines and alkynes via the *in situ* generation of nitrones.[12] However, the switch of photocatalytic selectivity in the rearrangement of oxaziridines, i.e., their conversion to amides instead of nitrones based on the SET mechanism, has not yet been achieved under visible-light irradiation. The transition state of C–O bond cleavage in single electron oxidized oxaziridines formed via the SET mechanism is lower in energy than that of N–O bond cleavage accompanying hydride shift. Thus, the conversion of oxaziridines to nitrones is the preferred pathway for their conversion to amides (Scheme 1b).[10] Herein, we present the weak base-promoted selective rearrangement of oxaziridines to amides via visible-light photoredox catalysis to resolve the selectivity switch in the SET mechanism (Scheme 1c).

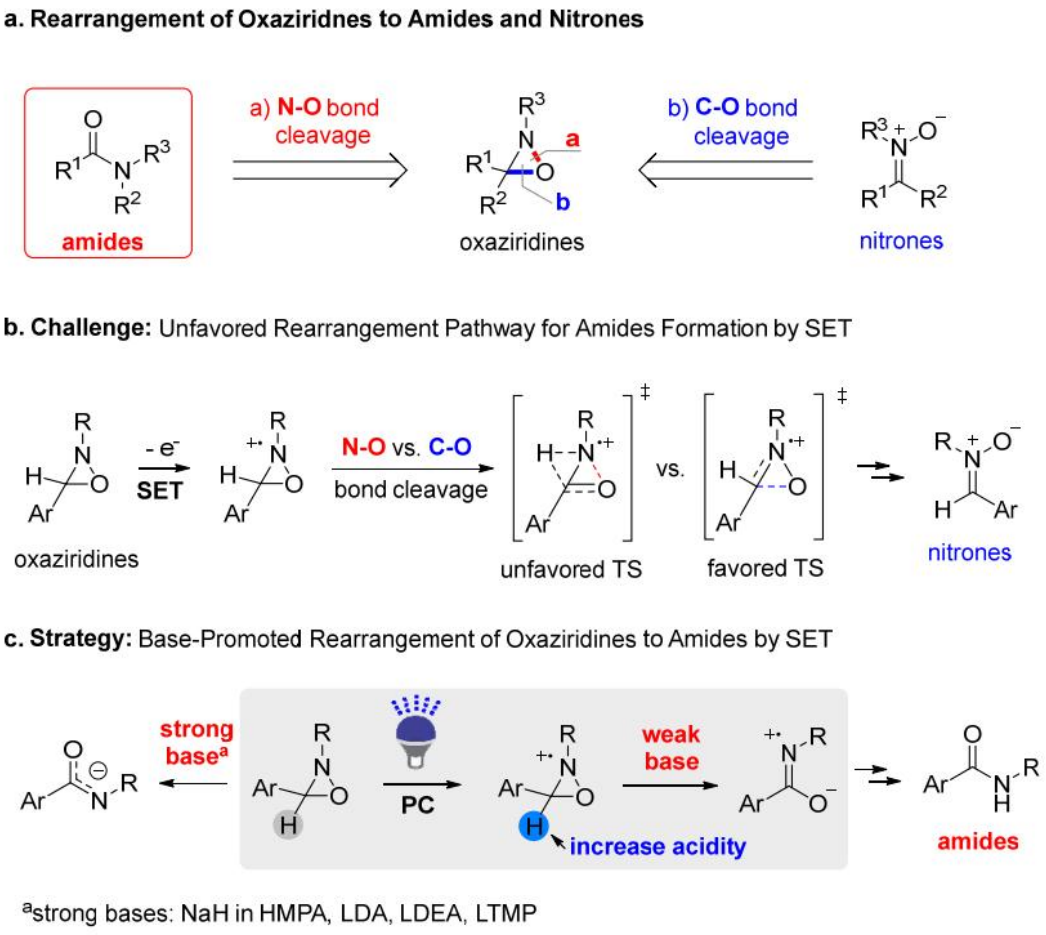

Scheme 1. Base□promoted rearrangement of oxaziridines to amides via visible□light photoredox catalysis

Moreover, our approach provides an efficient way to improve the previous method for converting oxaziridines into amides under harsh conditions. Rubottom and Newcomb reported the formation of strong base-mediated (NaH in HMPA, LDA, LDEA, and LTMP) amides from oxaziridines via the concerted deprotonation and ring opening of oxaziridines and a subsequent protonation, in which a strong base was employed because of the low acidity of oxaziridines.[6a,b] We envisioned that the photocatalytic single-electron oxidation of oxaziridines may increase their acidity, thus facilitating the application of a weak base feasible for converting oxaziridines to amides.

2.2. Simultaneous CO_2 conversion

Chemical processes using renewable feed stocks have been actively developed in accordance with the social demands for environmentally benign and cost-effective industrial processes. Converting renewable C1 resources (e.g., CO_2, CO, and carbonates) into valuable chemicals is an important sustainable process, as it improves the carbon balance and enables making a profit out of using wastes.[13−15] Among various C1 resources, this study focuses on inorganic carbonates (e.g., K_2CO_3, $KHCO_3$, Na_2CO_3, and $NaHCO_3$) derived from CO_2. Compared with the use of CO_2, the reactions involving inorganic carbonates do not require a high-pressure reactor or gas-feeding equipment, and their reaction yield can be increased by increasing solubility in the reaction media. In addition, inorganic carbonates function as a base and a carbon source, and thus, it is convenient to perform a process in which a base is required. Developing efficient and practical catalytic processes to convert inorganic carbonates to versatile chemicals is an alternative solution to mitigate global warming by expanding the chemical utility of inorganic carbonates, in addition to the conventional uses of inorganic carbonates such as in the glass and battery industries.[16-18] Glycerol chemistry involves green chemical processes that use renewable biowaste generated as a byproduct in the biodiesel industry.[19−22] The amount of glycerol produced is expected to increase abruptly with the rapid growth of the biodiesel industry.[23] Various glycerol applications ranging from chemical feedstocks to solvents have been reported owing to the nontoxicity, nonvolatility, and biodegradability of glycerol. In particular, glycerol has been used in metal-catalyzed dehydrogenation[24−28] and transfer hydrogenation.[29−32] While glycerol functions as a hydride source converting carbonates to formates, glycerol itself is also transformed to lactic acid, and these are useful monomers in the polylactic acid process. In this study, we investigated efficient Ir-catalyzed green processes for converting inorganic carbonates/glycerol to formates/lactates. The inorganic carbonate functioned as a C1 source and a base; carbonates were converted to formates, a valuable chemical in chemical industries,[33,34] and the basic property of carbonates is crucial for the conversion of glycerol to lactates. Glycerol also played the roles of a hydride source, lactate precursor, and solvent. To promote the efficient simultaneous conversion of carbonates and glycerol to formates and lactates, the catalytic activity of hydride transfer from glycerol to carbonates along with the stability of catalysts

under highly basic and harsh reaction conditions should be improved. The iridium complex possessing monodentate carbene ligands has shown good catalytic activities in the dehydrogenation of glycerol to form an iridium hydride,[24,35] but the formation of three carbene coordinated iridium complexes is the reason for the catalyst deactivation of monodentate carbene complexes.[36,37] Thus, iridium catalysts possessing chelating biscarbene ligands are expected to promote the efficient hydride transfer from glycerol to carbonates while preventing catalyst deactivation by the ligand chelation. Recently, Voutchkova-Kostal's research group has reported the Ru(II)-catalyzed transfer hydrogenation of CO_2 (and K_2CO_3) with glycerol in water (Scheme 1). This is a pioneering work demonstrating excellent catalytic activities for the formation of lactates, but formates were formed with lower TONs and TOFs.[38] Choudhury's group also reported that Ir catalysts possessing an abnormal carbene ligand (aNHC) promoted the conversion of CO_2 to formate with a TOF value of 149 h^{-1}.[39] Here, the contribution of our study is the development of the sustainable transfer hydrogenation of inorganic carbonates in glycerol by employing highly efficient biscarbene-modified Ir(I) complexes varied with different linker lengths to improve the formate formation. The effect of the chelate ligand was demonstrated by comparing it with the result of the monodentate carbene catalyst (Scheme 1). Based on theoretical calculations, biscarbene ligands possessing hydrocarbons of different tether lengths induce the geometrical changes of Ir catalysts, resulting in different catalytic activities in the formation of formates.

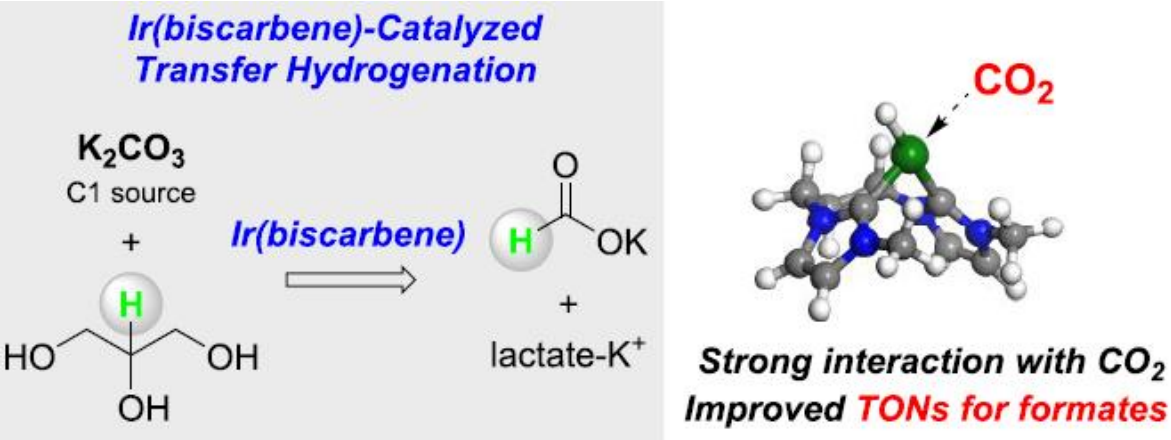

3. Methodological background

3.1. Photocatalysis

In organic chemistry, a radical is an atom or molecule with unpaired valence electron. These unpaired electrons cause the radical's high reactivity. For this reason, radical chemistry was interested of many researchers in the field of organic synthesis. However, radical's lifetime is short, that is difficult to make radical species[40]. To solve these problems, photoredox catalysis have been actively studied recently to make radicals easily. Photocatalysis is environmental-friedly, economical and efficient method **(Figure 1)**. Many researchers in chemistry using the photoredox catalysis method as a mild condition for chemical reactions. Photocatalysis often provides effective access to the reactive intermediates that cannot be readily generated through other strategies. Therefore, most of the electronically excited organic compounds and practical synthetic strategies involving radical ions rely on the use of photocatalyst.

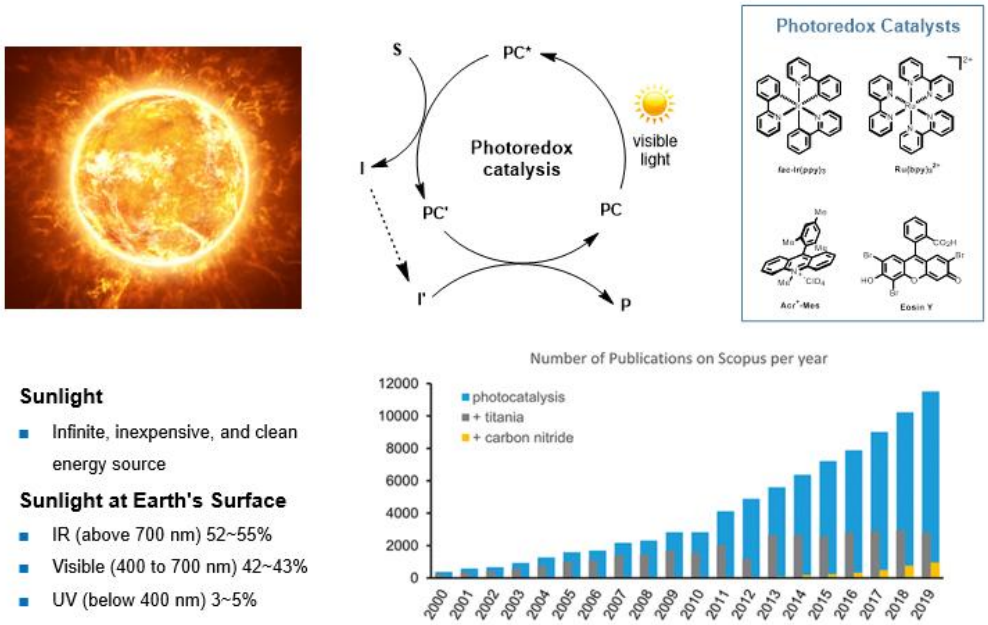

Figure 1. Advantage and tendancy of visible-light photoredox catalysis

The interaction between excited photocatalyst by visible-light and an organic substrate can provide the occurrence of active radical species that can be used for a various organic synthesis. There are three general reaction mechanism for photoredox catalysis[41] **(Figure 2)**. First, the "Electron Transfer" proceeded to an excited photocatalyst that generates the activation process through single electron oxidation or reduction of an organic substrate. The generating organic radical species can react directly with the coupler in a number of various bond-forming reaction. Second, the "Atom Transfer" is the transfer of atoms (almost hydrogen) from an organic substrate to a photocatalyst. Third, the "Energy Transfer" can activated an organic substrate through electronically excited photocatalysts. In this study, interaction pathway between organic substrate and photocatalyst is the single electron transfer (SET). One of two mechanistic process is used for SET photoredox catalysis reaction. According to the main direction of electrons transfer from the excited photocatalyst to the substrate, SET cycle is classified how to react. In the oxidative quenching cycle, the excited photocatalyst is quenched to donate an electron either the substrate or the oxidant, and in the reductive quenching cycle, that is quenched to accept an electron either substrate or reductant. To regenerate the ground state of the photocatalyst, the photocatalyst's oxidized cation radical in the oxidative quenching cycle has reduction and the reduced anionic radical of the photocatalyst in the reductive quenching cycle has oxidation, respectively[42] **(Figure 3)**.

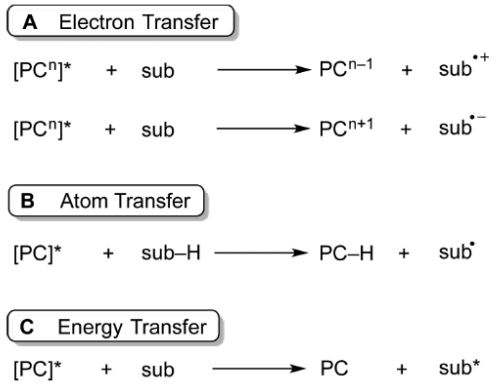

Figure 2. General mechanism for photoredox catalysis

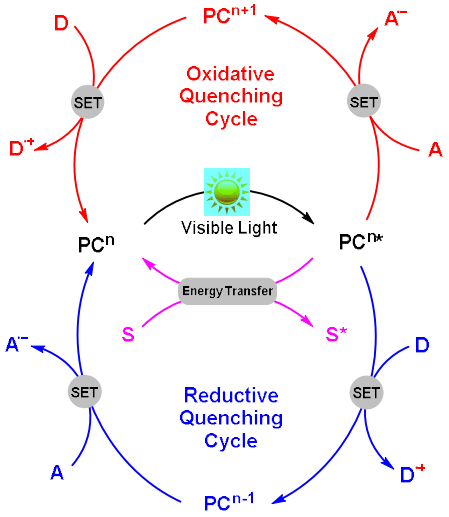

Figure 3. Oxidative and reductive quenching cycles of a photoredox catalyst

In the electron transfer reaction of the photocatalyst, thermodynamic spontaneity can be predicted through Gibbs energy according to Rehm-Weller equation[43] **(Equation 1)**.

Rehm–Weller equation

$$\Delta G_{eT} = E^{ox}_{1/2}(D) - E^{red}_{1/2}(A) + \Delta E_{Coulombic}$$

$\Delta G_{eT} < 0$: spontaneous
$\Delta G_{eT} > 0$: non-spontaneous

Equation 1. Rehm-Weller equation

Redox potential of catalysts and substrates can be easily obtained from literature data and cyclic voltammetry measurements. Redox potential of various photocatalyst and organic substrate are showed in **Figure 4**. The oxidation potential of the excited catalyst and the reduction potential of the substrate are both negative value in the oxidative quenching cycle, and if the oxidation potential of the excited catalyst has a negative value greater than that of the substrate reduction potential, the Gibbs energy has a negative value, and electron transfer occurs spontaneously. Conversely, both the reduction potential of the excited catalyst and the oxidation potential of the substrate have positive values on the reductive quenching cycle. If the reduction potential of the excited catalyst is greater than that of the substrate, the Gibbs free energy is a negative and electron transfer occurs spontaneously.

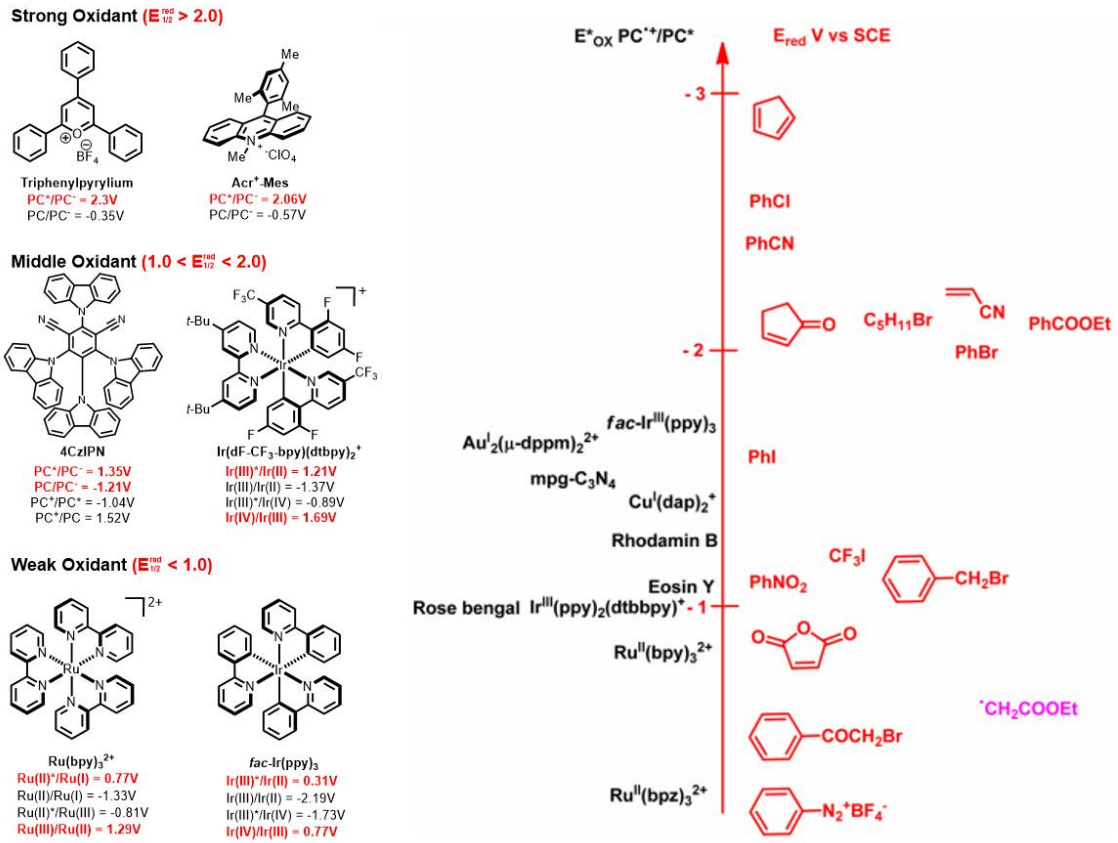

Figure 4. Redox potential parameter of various photoinduced catalyst and organic substrate

3.2. DFT & Aromaticity

Modern density functional theory plays an important role in many fields of science. The main research strategy of this thesis is the computational method based on the density functional theory, which was extensively used to explain various surface phenomena such as adsorption and chemical reactions, via collaboration with experimental research using scanning tunneling microscopy. In this Chapter, the essentials of electronic structure theory are briefly summarized to provide theoretical background from the Schrödinger equation for many-body system to Kohn-Sham density functional equation.[44-46] The mathematical notations used in this Chapter are mainly based on the book written by Richard M. Martin, "Electronic Structure: Basic Theory and Practical Methods".[44] A simple introduction to scanning tunneling microscopy is provided at the last section.[47]

3.2.1. Hohenberg-Kohn theorems

In the fundamental philosophy of DFT, all properties of a system composed of many interacting particles can be determined by a functional of the ground state electron density n0(r). This is based upon the theorems for such functionals as given by P. Hohenberg and W. Kohn in 1964.[50]

- **Theorem I** : For any system of interacting particles in an external potential Vext(r), the potential Vext(r) is determined uniquely, except for a constant, by the ground state particle density n0(r).

Therefore, if the Hamiltonian is uniquely determined by the ground state density n0(r) according to the Hohenberg-Kohn theorem I, the wavefunction of any state can be determined by solving the Schrödinger equation with this Hamiltonian. Thus, all properties of the system are completely determined by ground state density.

- **Theorem II** : A universal functional for the energy E[n] in terms of the density n(r) can be defined, valid for any external potential Vext(r). For any particular Vext(r), the exact ground state energy of the system is the global minimum value of this functional, and the density n(r) that minimizes the functional is the exact ground state density n0(r).

Therefore, if the functional including all internal energies (kinetic and potential energies) of the interacting electron system is known, the exact ground state density of energy by minimizing the total energy of the system using the variational principle with respect to the density function n(r). However, the Hohenberg-Kohn theorem II does not provide any guidance concerning the excited states of the electrons.

3.2.2. The Kohn-Sham approach

The Kohn-Sham approach is to replace the difficult interacting many-body system with a different auxiliary system which can be more easily solved. The *ansatz* of Kohn and Sham assumes that the ground state density of the original interacting system is equal to that of some chosen non-interacting system.[48,49] This leads to independent-particle equations for the non-interacting system that can be considered exactly soluble with all the difficult many-body terms incorporated into an exchange-correlation functional of the density. Therefore, the accuracy of Kohn-Sham approach is only limited by the exchange-correlation functional.

The Kohn-Sham construction of an auxiliary system rests upon two assumptions: (1) The exact ground state density can be represented by the ground state density of an auxiliary system of non-interacting particles. This leads to the relation of the actual and auxiliary systems. (2) The auxiliary Hamiltonian is chosen to have the usual kinetic operator and an effective local potential $V_{\text{eff}}^{\sigma}(\mathbf{r})$ acting on an electron of spin σ at point **r**.

The auxiliary Hamiltonian for the independent-particle system is

$$\hat{H}_{\text{aux}}^{\sigma} = -\frac{1}{2}\nabla^2 + V^{\sigma}(\mathbf{r}) \quad . \tag{2.20}$$

The density of the auxiliary system is given by sums of squares of the orbitals for each spin

$$n(\mathbf{r}) = \sum_{\sigma} n(\mathbf{r},\sigma) = \sum_{\sigma}\sum_{i=1}^{N^{\sigma}} \left|\psi_i^{\sigma}(\mathbf{r})\right|^2 \quad , \tag{2.21}$$

the independent-particle kinetic energy T_s is given by

$$T_s = -\frac{1}{2}\sum_{\sigma}\sum_{i=1}^{N^{\sigma}} \left\langle \psi_i^{\sigma} \middle| \nabla^2 \middle| \psi_i^{\sigma} \right\rangle = \frac{1}{2}\sum_{\sigma}\sum_{i=1}^{N^{\sigma}} \int d^3r \left|\nabla \psi_i^{\sigma}(\mathbf{r})\right|^2 \quad , \tag{2.22}$$

and we define the classical Coulomb interaction energy of the electron density $n(\mathbf{r})$ interacting with itself, i.e., the Hartree energy.

$$E_{\text{Hartree}}[n] = \frac{1}{2}\int \mathrm{d}^3 r \mathrm{d}^3 r' \frac{n(\mathbf{r})n(\mathbf{r}')}{|\mathbf{r}-\mathbf{r}'|} \tag{2.23}$$

The [n] denotes a functional of the density $n(\mathbf{r},\sigma)$ which depends on both position in space $\mathbf{r}$ and spin σ. Now, the Kohn-Sham approach to the full interacting many-body problem is to rewrite the Hohenberg-Kohn expression for the ground state energy functional in the form

$$E_{\text{KS}} = T_s[n] + \int \mathrm{d}\mathbf{r} V_{\text{ext}}(\mathbf{r})n(\mathbf{r}) + E_{\text{Hartree}}[n] + E_{II} + E_{\text{xc}}[n] \tag{2.24}$$

Here, all many-body effects of exchange of correlation are grouped into the exchange-correlation energy E_{xc}.

$$E_{xc}[n] = \left\langle \hat{T} \right\rangle - T_s[n] + \left\langle \hat{V}_{\text{int}} \right\rangle - E_{\text{Hartree}}[n] \tag{2.25}$$

If the universal functional $E_{\text{xc}}[n]$ defined in (2.25) were known, then the exact ground state energy and density of the many-body electron problem could be found by self-consistently solving the Kohn-Sham equations for independent particles.

The Kohn-Sham auxiliary system for the ground state can be viewed as a problem of minimization with respect to density $n(\mathbf{r},\sigma)$. Because T_s is the functional of the orbitals and all other terms are functionals of the density, one can vary the wavefunctions and use the chain rule to derive the variational equation

$$\frac{\delta E_{\text{KS}}}{\delta \psi_i^{\sigma *}(\mathbf{r})} = \frac{\delta T_s}{\delta \psi_i^{\sigma *}(\mathbf{r})} + \left[\frac{\delta E_{\text{ext}}}{\delta n(\mathbf{r},\sigma)} + \frac{\delta E_{\text{Hartree}}}{\delta n(\mathbf{r},\sigma)} + \frac{\delta E_{\text{xc}}}{\delta n(\mathbf{r},\sigma)}\right]\frac{\delta n(\mathbf{r},\sigma)}{\delta \psi_i^{\sigma *}(\mathbf{r})} = 0 \tag{2.26}$$

subject to the orthonormalization constraints

$$\left\langle \psi_i^{\sigma} \middle| \psi_j^{\sigma'} \right\rangle = \delta_{i,j}\delta_{\sigma,\sigma'} \tag{2.27}$$

Using expressions (2.21) and (2.22) for $n^{\sigma}(\mathbf{r})$ and T_s, which give

$$\frac{\delta T_s}{\delta \psi_i^{\sigma *}(\mathbf{r})} = -\frac{1}{2}\nabla^2 \psi_i^{\sigma}(\mathbf{r}) \quad , \quad \frac{\delta n(\mathbf{r},\sigma)}{\delta \psi_i^{\sigma *}(\mathbf{r})} = \psi_i^{\sigma}(\mathbf{r}) \tag{2.28}$$

and using the Lagrange multiplier method leads to Kohn-Sham Schrödinger-like equations:

$$\left(H_{\mathrm{KS}}^{\sigma}-\varepsilon_i^{\sigma}\right)\psi_i^{\sigma}(\mathbf{r})=0 \quad , \tag{2.29}$$

where ε_i are the eigenvalues, and H_{KS} is the effective Hamiltonian

$$H_{\mathrm{KS}}^{\sigma}=-\frac{1}{2}\nabla^2+V_{\mathrm{KS}}^{\sigma}(\mathbf{r}) \quad , \tag{2.30}$$

with

$$V_{\mathrm{KS}}^{\sigma}(\mathbf{r})=V_{\mathrm{ext}}(\mathbf{r})+\frac{\delta E_{\mathrm{Hartree}}}{\delta n(\mathbf{r},\sigma)}+\frac{\delta E_{\mathrm{xc}}}{\delta n(\mathbf{r},\sigma)}=V_{\mathrm{ext}}(\mathbf{r})+V_{\mathrm{Hartree}}(\mathbf{r})+V_{\mathrm{xc}}^{\sigma}(\mathbf{r}) \quad . \tag{2.31}$$

Kohn-Sham equations have the form of independent particle equations with a potential that must be solved self-consistently with the resulting energy or Hellmann-Feynman force. (The typical iterative process is shown in Figure 2.1.) These equations would lead to the exact ground state density and energy for the interaction system, if the exact functional $E_{\mathrm{xc}}[n]$ were known. Therefore, the major problem in DFT is deriving suitable formulas for the exchange-correlation term.

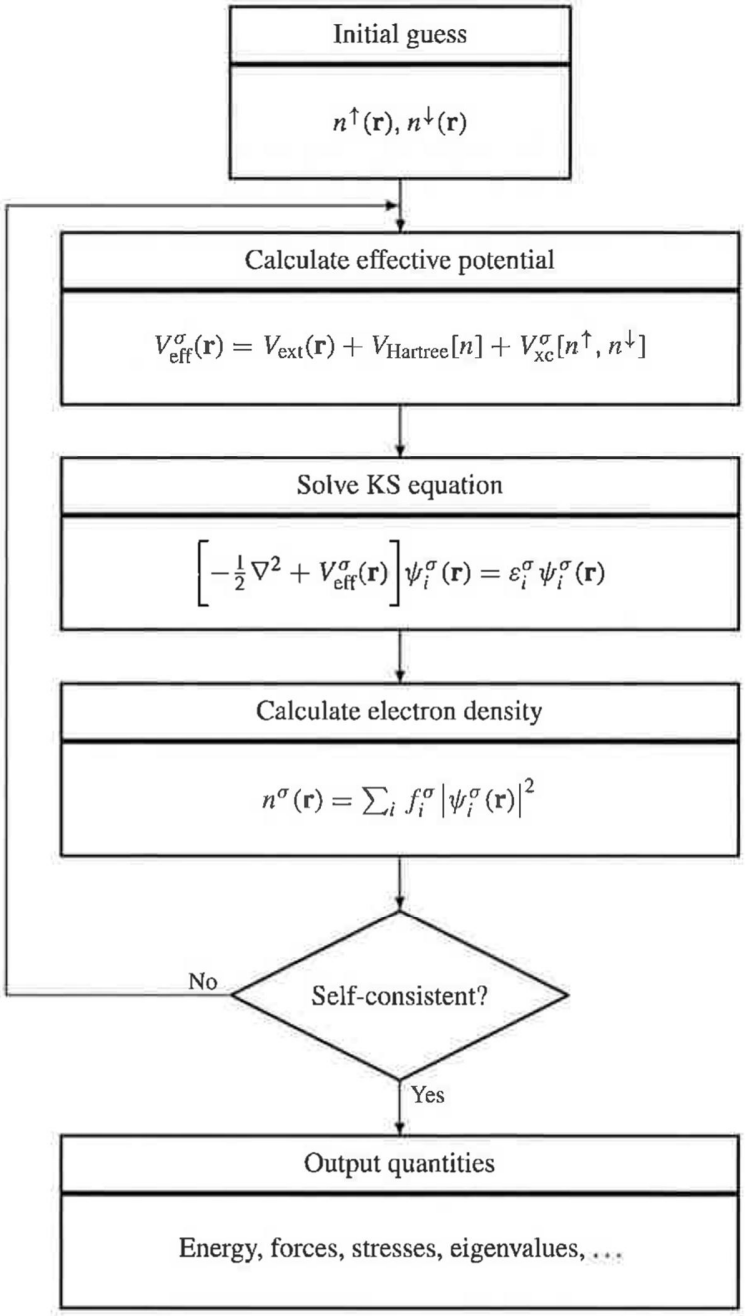

Figure 2.1. Schematic representation of the self-consistent loop for solution of Kohn-Sham equations. [Adapted from Reference 1]

3.2.3. The exchange-correlation functional

In the practical use of DFT, the most general approximations to describe $E_{xc}[n]$ are local density approximation (LDA) (or more generally, the local spin density approximation (LSDA)) and generalized gradient approximation (GGA).

Usually solids can be considered as close to the limit of the homogeneous electron gas. In that limit, the effects of exchange and correlation are local in character. Therefore, in the case of LDA, the exchange-correlation energy is simply an integral over all space with the exchange-correlation energy density at each point assumed to be the same as in a homogenous electron gas with that density,

$$\begin{aligned} E_{xc}^{LSDA}[n^{\uparrow},n^{\downarrow}] &= \int d^3rn(\mathbf{r})\varepsilon_{xc}^{hom}(n^{\uparrow}(\mathbf{r}),n^{\downarrow}(\mathbf{r})) \\ &= \int d^3rn(\mathbf{r})[\varepsilon_{x}^{hom}(n^{\uparrow}(\mathbf{r}),n^{\downarrow}(\mathbf{r}))+\varepsilon_{c}^{hom}(n^{\uparrow}(\mathbf{r}),n^{\downarrow}(\mathbf{r}))]. \end{aligned} \tag{2.32}$$

For unpolarized systems, the LDA is found simply by setting $n^{\uparrow}(\mathbf{r}) = n^{\downarrow}(\mathbf{r}) = n(\mathbf{r})/2$. LDA is best for solids close to a homogeneous gas and worst for very inhomogeneous cases like atoms where the density must go continuously to zero outside the atom. The other approximation is GGA, which is a marked improvement over LDA for many cases. E_{xc} of GGA with a magnitude of the gradient of density $|\nabla n^{\sigma}|$ is written as

$$\begin{aligned} E_{xc}^{GGA}[n^{\uparrow},n^{\downarrow}] &= \int d^3rn(\mathbf{r})\varepsilon_{xc}(n^{\uparrow},n^{\downarrow},|\nabla n^{\uparrow}|,|\nabla n^{\downarrow}|,\ldots) \\ &= \int d^3rn(\mathbf{r})\varepsilon_{x}^{hom}(n)F_{xc}(n^{\uparrow},n^{\downarrow},|\nabla n^{\uparrow}|,|\nabla n^{\downarrow}|,\ldots), \end{aligned} \tag{2.33}$$

where F_{xc} is dimensionless and $\varepsilon_{x}^{hom}(n)$ is the exchange energy of the unpolarized gas. Unlike LDA, the spin-scaling relationship should be considered in GGA, and in particular, for $F_x(n,|\nabla n|)$ of the polarized system. As there are numerous forms that F_x may take, many kinds of GGA methods have been proposed so far, such as Becke (B88),[51] Perdew and Wang (PW91),[52,53] and Perdew, Becke, and Enzerhof (PBE).[54]

4. Results and Discussion

4. 1. Rearrangement of Oxaziridines to Amides

4.1.1. Preliminary results of the selectivity switch of the rearrangement of oxaziridines

To test our hypothesis (Scheme 2), oxaziridine 1a was irradiated under blue LEDs in the presence of Fukuzumi acridinium in various solvents before screening for weak bases. Preliminary studies showed that several solvents act as weak bases for the selective rearrangement of oxaziridine 1a to form amide 2a. Conversely, other solvents with low basicity predominantly afforded nitrone 3a. The selectivity of the rearrangement of oxaziridines is consistent with the basicity order of the solvents. In relatively basic solvents, such as DMF, DMAc, and DMSO, a weak base-promoted rearrangement of oxaziridine occurs via the SET mechanism. Thus, the dependence of reactivity on the basicity of solvents shows the reliability of our hypothesis.

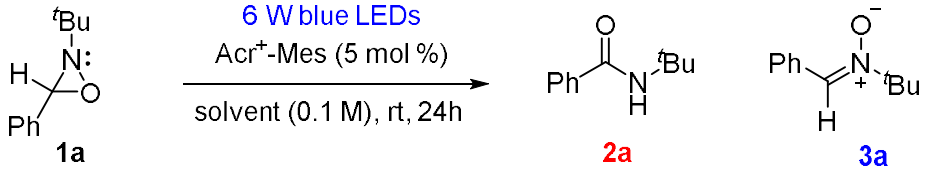

amide 2a as major product

DMF (51%), N,N-Dimethylacetamide (20%), DMSO (22%)

nitrone 3a as major product

MeCN (8%), EtOAc (12%), acetone (8%), MeOH (trace)
EtOH (trace), iPrOH (trace), DCM (9%), chloroform (11%)

pKa value of conjugate acid of solvents

DMF (-0.3), N,N-Dimethylacetamide (-0.19), DMSO (-2.7)
MeCN (-4.3), EtOAc (-6.5), acetone (-7.2), MeOH (-2.2)

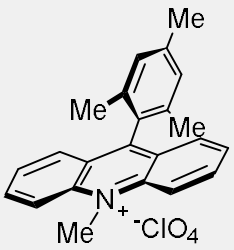

Acr+-Mes

order of basicity of solvents

N,N-Dimethylacetamide > DMF > MeOH > DMSO > MeCN > EtOAc > acetone

Scheme 2. Preliminary results of the selectivity switch of the rearrangementof oxaziridines.

4.1.2. Optimization of rearrangement from oxaziridine to amide

Preliminary results showed that oxaziridine 1a was selectively converted to amide 2a in 51% yield using DMF as a solvent; therefore, further optimization was performed based on this result (Table 1). The DMF concentration and catalyst loading were varied to achieve an improved yield; however, variations in these parameters could not improve the yield of the reaction (Table 1, entries 2–6). Thus, we considered introducing additives to enhance the reactivity, which act as bases and proton sources in the rearrangement of oxaziridine 1a to form amide 2a. We explored carboxylic acids as the additives, which can generate carboxylates as weak bases and donate protons to the reaction intermediates. The trifluoroacetic acid (TFA) additive dramatically improved the yield of amide 1a to 95% under 1 mol % catalytic conditions (Table 1, entry 9). We established the optimized reaction conditions using TFA as the additive. Further control experiments were performed in the absence of a photocatalyst and a light source to confirm the photocatalytic reaction pathway. The desired product was not detected in the absence of a light source (Table 1, entry 10), and only a low yield of amide 2a was achieved under blue LED irradiation without a photocatalyst (Table 1, entry 11). Additionally, the thermal rearrangement of oxaziridines didnot occur at room temperature and a high temperature was required (for details, refer to the ESI†). Therefore, the high reactivity observed in the rearrangement of oxaziridine 1a to form amide 2a using TFA as the additive can be achieved via photocatalysis.

Table 1. Optimization of the reaction conditions[a]

Entry	Acr^+-Mes (mol %)	DMF (M)	Additive (equiv.)	Yield (%)[b]
1	5.0	DMF (0.1)	-	51[c]
2	5.0	DMF (0.2)	-	31
3	5.0	DMF (0.5)	-	34
4	5.0	DMF (1.0)	-	26
5	3.0	DMF (0.1)	-	35
6	1.0	DMF (0.1)	-	30
7	1.0	DMF (0.1)	HCO_2H (0.5)	60
8	1.0	DMF (0.1)	AcOH (0.5)	30
9	**1.0**	**DMF (0.1)**	**TFA (0.5)**	**95**[c]
10[d]	1.0	DMF (0.1)	TFA (0.5)	nd
11	-	DMF (0.1)	TFA (0.5)	25[c]

[a]Reaction conditions: 1a (0.2 mmol), catalyst (quantity noted), DMF (quantity noted) with 6 W blue LEDs (450 nm) irradiation at room temperature under argon in a pressure tube. [b]GC yield (internal standard: decane) [c]Isolated yield via flash column chromatography. [d]In the absence of a light source. nd = not detected.

4.1.3. Substrate scope of various functional group amides

Under these optimized conditions, we explored the scope of various oxaziridines 1 (Table 2). N-tert-Butyl-substituted aryl oxaziridines (1b–1r) were converted to the corresponding amides (2b–2r), achieving good to excellent yields. para-Substituted aryl oxaziridines (1b–1e and 1f–1j) with electron-donating groups (EDGs), electron-withdrawing groups (EWGs), and halogens afforded the desired products (2b–2e and 2f–2j) in 30–99% yield. Lower yields were obtained for tert-butyl, methoxy, and strong EWG substituted aryl oxaziridines (1c, 1e, 1f, and 1i). Notably, ortho- and meta-substituted methyl, methoxy, or chloro aryl oxaziridines (1k–1p) were converted to the corresponding amides (2k–2p) in excellent yields. Moreover, furan and pyridine-substituted oxaziridines (1q and 1r, respectively) were effectively converted to the corresponding amides (2q and 2r, respectively). Next, we investigated the rearrangement of various alkyl oxaziridines (1s–1w), such as linear, branched, and cyclic alkyl oxaziridines. The alkyl oxaziridines were well converted to the corresponding amides in good yields. The styrene moiety in oxaziridine 1x exhibited good tolerance using the developed method. Finally, we tested various N-alkyl-substituted oxaziridines (1y-ab) to synthesize various N-substituted amides and obtained good results.

Table 2. Substrate scopes[a]

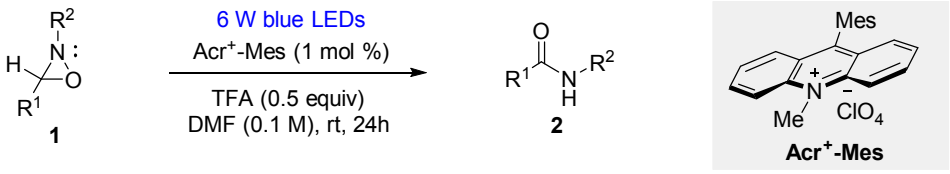

R^1 = Aryl, R^2 = ^{t}Bu

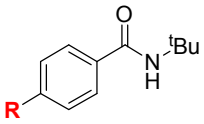

(R : EDG)

2b (70% R = Me)
2c (54% R = ^{t}Bu)
2d (90% R = Ph)
2e (30% R = OMe)

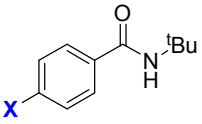

(X : Halogen)

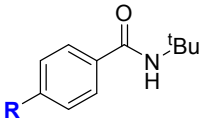

(R : EWG)

2f (64% X = F)
2g (96% X = Cl)
2h (88% X = Br)

2i (76% R = NO_2)
2j (99% R = CO_2Me)

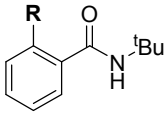

2k (66% R = Me)
2l (90% R = OMe)
2m (88% R = Cl)

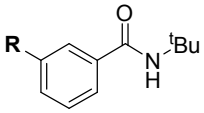

2n (86% R = Me)
2o (97% R = OMe)
2p (90% R = Cl)

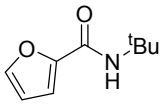

2q (60%)

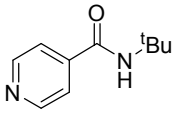

2r (80%)

R^1 = Alkyl or Vinyl, R^2 = ^{t}Bu

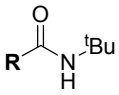

2s (80% R = ^{n}Pentyl)
2t (71% R = ^{n}Hexyl)
2u (54% R = ^{i}Propyl)
2v (60% R = ^{i}Butyl)

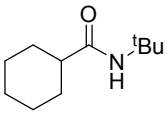

2w (86%)

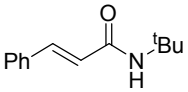

2x (60%)

R^1 = Phenyl, R^2 = Alkyl

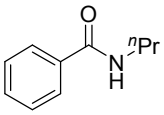

2y (92%)

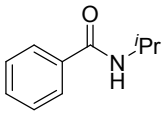

2z (95%)

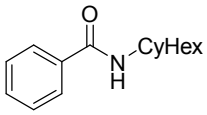

2aa (85%)

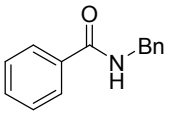

2ab (60%)

[a] Giese reaction conditions: Table 1, entry 9, Isolated yield via flash column chromatography.

4.1.4. Control experiements

We performed control experiments to gain insight into the reaction mechanism. We performed Stern–Volmer luminescence quenching experiments to prove the SET pathway instead of direct photoexcitation by blue light. We measured the CV and UV-vis absorption spectra of 1a and 1a with TFA (see details in the ESI†). These control experiments well elucidated the mechanism of SET via visible-light photoredox catalysis. Subsequently, we tested the deuterium-substituted oxaziridine 1a-D to confirm the proton transfer from carbon to nitrogen by DMF. Consequently, it was confirmed that deuterium shifts from carbon to the nitrogen of the amide 2a-D. The deuterium ratio decreased, possibly owing to the trace amounts of water in the DMF. Furthermore, when methyl (4a) or phenyl (4b) was employed at the position of hydrogen in the carbon of oxaziridine 1a, the desired amides were not formed. These results indicate that to initiate the rearrangement, the deprotonation of hydrogen from the ring carbon with the base species is necessary (Scheme 3a). We proposed that trifluoroacetate and TFA act as the weak base and proton source, respectively, to improve the rearrangement reactivity of oxaziridines to amides. Furthermore, TFA can control the selective formation of amides instead of nitrones in acetonitrile or ethyl acetate (Scheme 3a). Therefore, TFA is instrumental in the base-promoted selective rearrangement. Based on the literature[6a,b,9a,10,12] and control experiments, the proposed mechanism is illustrated in Scheme 3b. The excited photocatalyst oxidizes oxaziridine 1a to generate radical cation intermediate I via the SET mechanism. DMF and TFA are equilibrated with trifluoroacetate and protonated DMF (H-DMF$^+$) based on their pKa values in an acid–base equilibrium. Trifluoroacetate or DMF act as a base to deprotonate the proton of I, which undergoes ring opening to form intermediate II. Intermediate II is converted to intermediate III via proton transfer from TFA or protonated DMF (H-DMF$^+$). Finally, amide 2a is formed by the single-electron reduction of III, followed by amide–iminol tautomerism. In the base-promoted rearrangement of oxaziridines to form amides, TFA improves the reactivity and selectivity by (1) improving the reactivity of the deprotonation step because it is more basic than other solvents and (2) increasing the concentration of protons in the reaction solution to facilitate the protonation step where II is converted to III.

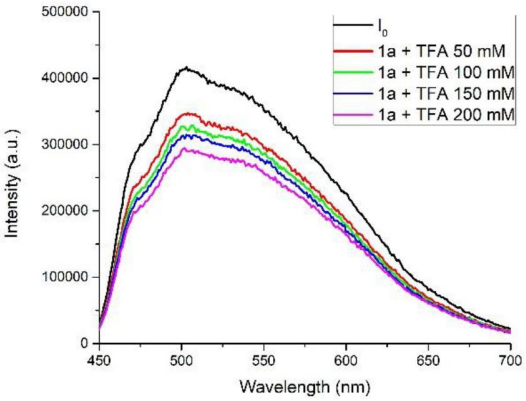

Figure S7. Luminescence quenching by 1a

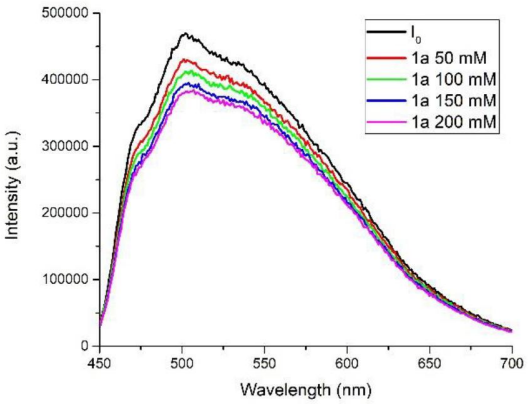

Figure S8. Luminescence quenching by 1a with TFA (0.5 equiv)

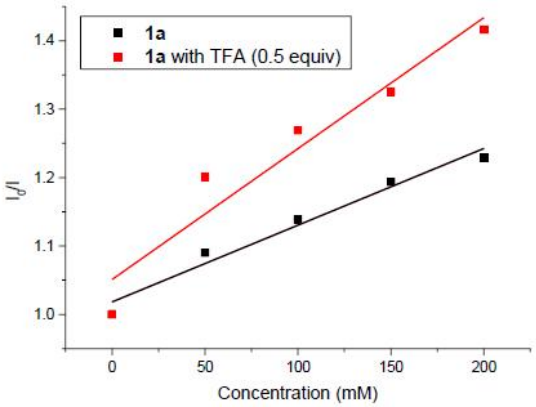

Figure S9. Stern–Volmer plot 1a and 1a with TFA

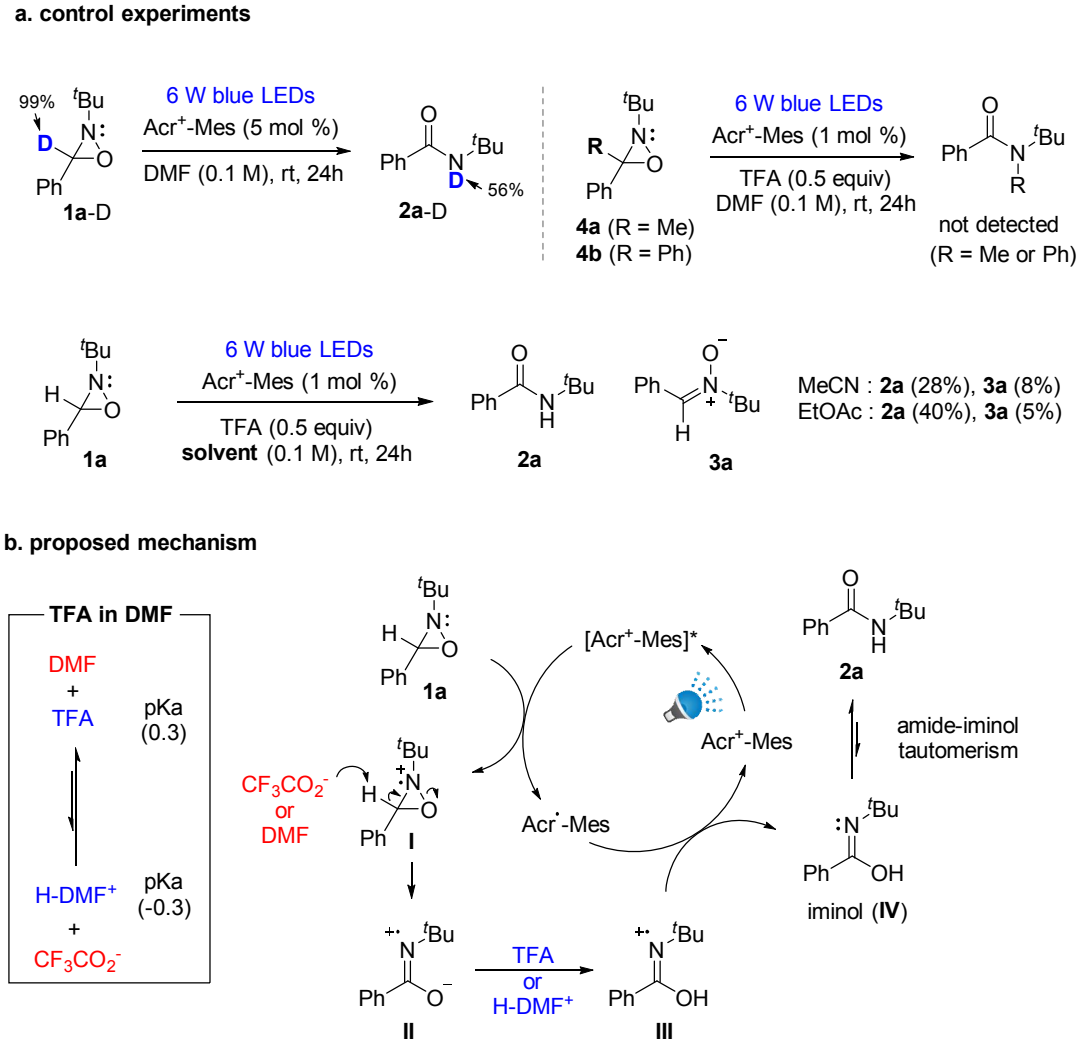

Scheme 3. Control experiments and proposed mechanism.

4.1.5. Density functional theory (DFT) calculations

Density functional theory (DFT) calculations were performed to verify the experimentally proposed rearrangement mechanism, which can be described as a Brønsted–Lowry acid–base reaction. The cation radical intermediate I and DMF (or trifluoroacetate) serve as the acid and base, respectively.

Nevertheless, the most straightforward route for the direct conversion of I to its amide form can occur via the intramolecular hydrogen transfer from carbon to nitrogen in a three-membered ring, followed by ring opening via N–O bond cleavage. The reaction energy profile was thus evaluated for the two reaction mechanisms (Fig. S12, ESI†): (i) the Brønsted–Lowry acid–base reaction of intermediate I with DMF (or trifluoroacetate) and (ii) the intramolecular hydrogen transfer followed by ring opening. All the optimized geometries and corresponding spin densities are presented in Fig. S13 (ESI†). As expected, the intramolecular hydrogen transfer process requires an overall high activation energy (DGTS = 39.1 kcal/mol), although the following ring-opening step can proceed easily. The DGTS values for the base-promoted rearrangement after binding with the base species, i.e., DMF and $CF_3CO_2^-$, are considerably reduced to 17.9 and 9.4 kcal/mol, respectively (Fig. S12 and Fig. 1c, ESI†), thereby supporting the reliability of the experimentally proposed reaction mechanism. Our DFT calculations revealed that the ratedetermining step corresponds to deprotonation from the ring carbon of intermediate I by the base species. As the chemical reactivity is substantially improved with $CF_3CO_2^-$, the conjugated base of the TFA additive, compared with that of the solvent DMF, we employed one more base species, acetonitrile (MeCN), to elucidate the dependence of chemical reactivity on the base species with different levels of basicity. Their pKa values indicate that the order of their basicity is MeCN < DMF < $CF_3CO_2^-$. The electrostatic potential (ESP) maps for I and the base species suggest acidic and basic sites on the molecular electron densities (Fig. 1a). The binding structures between I and the base species were optimized based on the distribution of estimated ESP maps (Fig. 1b). The binding energies (DGBE) between I and the base species for MeCN, DMF, and $CF_3CO_2^-$ were 3.95, 2.54, and 4.14 kcal/mol, respectively. In addition to the calculated ΔG_{BE} values and binding distances (Fig. 1b), the estimated ΔG^{TS} values show good agreement with the basicity of the base species (Fig. 1c and

refer to Fig. S14 for the optimized geometries, ESI†). The less-basic MeCN achieves a larger ΔG^{TS} value than those of DMF and $CF_3CO_2^-$ (increased by 9.4 and 17.9 kcal/mol, respectively). Therefore, the DFT results not only agree well with our experimental observations but also imply the importance of the solvent components in controlling the reactivity of the photocatalytic SET process.

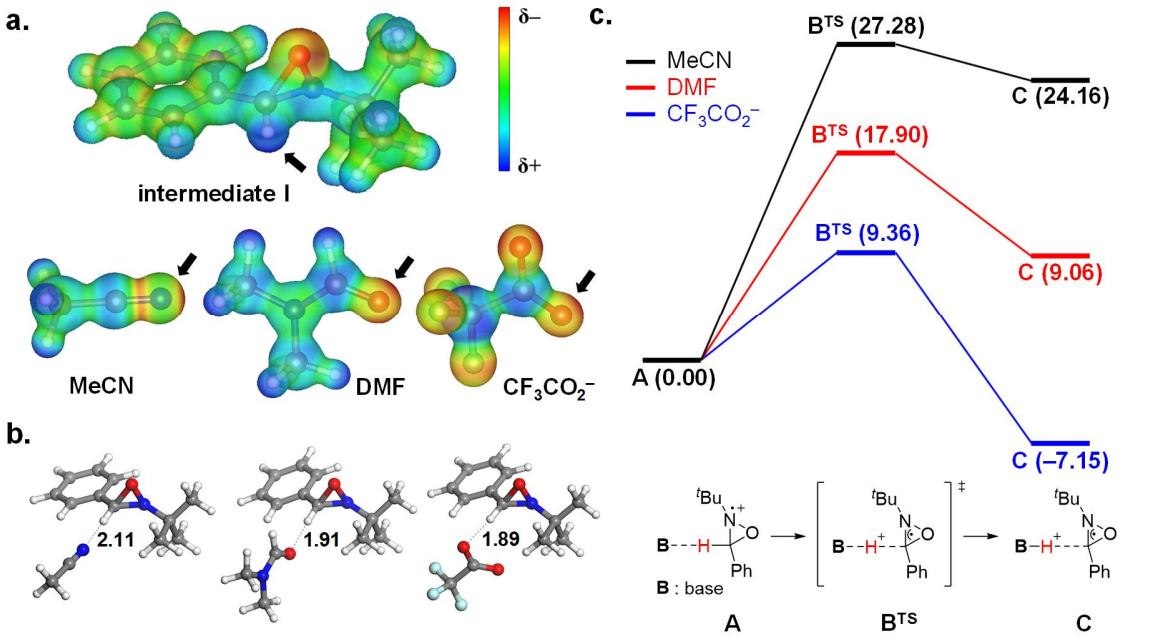

Fig. 1 (a) Electrostatic potential maps for intermediate I, MeCN, DMF, and trifluoroacetate; (b) binding geometries and binding distances (A); and (c) energy profile (DG, kcal mol_1) for the deprotonation of I depending on the base species.

4. 2. Simultaneous CO_2 conversion

4.2.1. Optimization catalyst from Transfer Hydrogenation of K2CO3 in Glycerol

For the transfer hydrogenation of inorganic carbonates in glycerol, Ir(I) complexes including commercially available complexes were examined As metal catalysts possessing carbene ligands showed significant catalytic performances in glycerol dehydrogenation,[55,56] Ir(I) complexes possessing bidentate carbene ligands (1−3, 1′, 2′, 1″, and 6) were examined and compared with commercially available Ir(I) complexes without carbene ligands (4 and 5). In addition to the electronic effect of carbene ligands, the steric effect of wing-tip substituents, the tether length of biscarbene ligands, the anion effect, and cyclooctadiene (COD) vs CO substitution in the iridium complexes were examined using catalysts 1−3, 1′, 2′, 1″, and 6.

The catalytic activity of various Ir catalysts in Figure 1 was studied as shown in Table 1. The turnover numbers (TONs) of each product were quantitated with ^1H nuclear magnetic resonance (NMR) with an internal standard (see Supporting Information). In addition to formates and lactates, only propylene glycol was observed as a by-product. By optimally varying the amount of ethanol and the ratio of K_2CO_3/glycerol (see Supporting Information, Table S1), the reaction conditions involving K_2CO_3 (4 mmol), glycerol (1 mL, 13.7 mmol), and EtOH (0.05 mL) in the presence of Ir(I) catalysts (0.14 μmol) at 150 °C were chosen. Catalysts were soluble in alcohols such as ethanol and glycerol, resulting in good reactivities in the reaction. Catalysts 1−3 possessing a bidentate biscarbene ligand, COD, and anions (Br^-, I^-, $PF6^-$) showed slightly different catalytic activities. Catalyst 1 possessing Br^- showed the highest TONs of formates and lactates. A similar trend was observed in the catalytic activities of 1′ and 2′. Based on the results of entries 1−5, the Ir(biscarbene) catalyst 1 possessing COD and Br^- was selected as the most reactive catalyst. Commercial iridium complexes possessing phenanthroline and acetonitrile showed inferior activities compared with Ir(biscarbene) catalysts (entries 6 and 7). The structure of the carbene ligands is critical; replacing the methyl group at the wing-tip of **1** with an ethyl group lowered TONs of formates (entry 8), and the shorter tether of biscarbene ligands (C3 to C1) decreased TONs of formats and lactates significantly, as shown in the result of catalyst 6 (entry 9). The theoretical calculation

accounting for the result of entry 9 is provided later. Using the most effective catalyst 1, a higher temperature was applied, demonstrating higher TONs (16856 for formates and 32609 for lactates) (entry 10). The turnover frequency (TOF) values are 843 and 1630 h^{-1} for formates and lactates, respectively. At 180 °C, the dramatic stability of Ir(biscarbene) catalysts was attributed to the chelation effect of bidentate carbene ligands.[57] The Ir-(monodentate carbene) 7[12] catalyzed reaction showed lower TONs for the formation of both products; TON 8167 (formates) and TON 18802 (lactates) were observed with catalyst 7 (entry 11). The conversions of glycerol of Table 1 were ~25−35% with catalysts 1, 2, 3, 1′, 2′, and 1″, 9% with catalyst 6, and 3% with catalysts 4 and 5 (Table 1). Glycerol was used as an excess reactant and the solvent

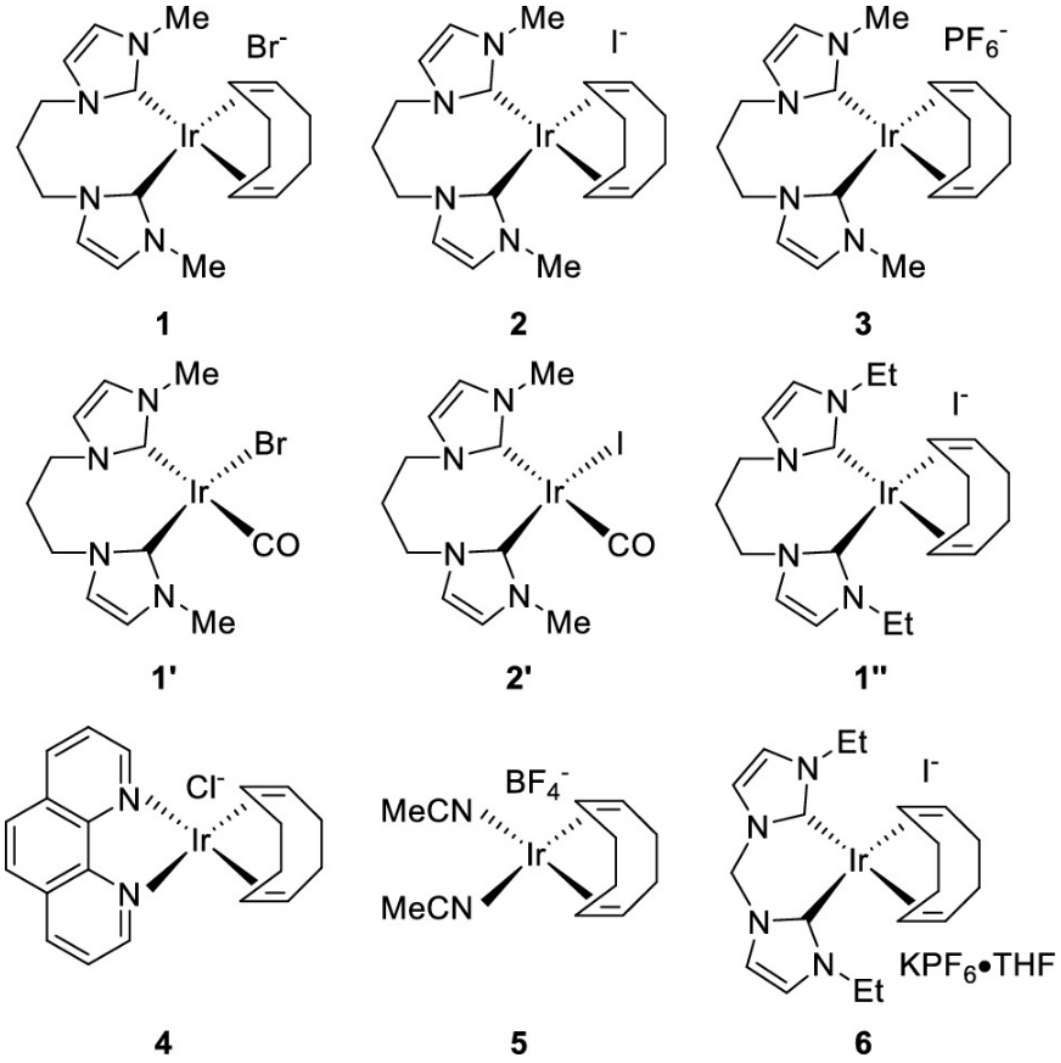

Figure 1. Ir(I) catalysts used for the transfer hydrogenation of K_2CO_3 in glycerol.

Table 1. Results of the Transfer Hydrogenation of K_2CO_3 in Glycerol[a]

entry	catalyst	temp	formate (TON[b])	lactate (TON[b])	conv[b,c] (selectivity[d])
1	**1**	150 °C	13406	25517	31% (84%)
2	**2**	150 °C	9225	23115	30% (80%)
3	**3**	150 °C	11046	21998	25% (88%)
4	**1′**	150 °C	10764	22245	28% (82%)
5	**2′**	150 °C	8874	22130	28% (82%)
6	**4**	150 °C	877	3210	3% (>99%)
7	**5**	150 °C	3444	1448	3% (50%)
8	**1″**	150 °C	8111	19853	25% (80%)
9	**6**	150 °C	4839	9055	9% (98%)
10	**1**	180 °C	16856	32609	35% (94%)
11	**7**	180 °C	8167	18802	19% (99%)

[a]The mixture of catalysts (0.14 μmol, 0.0035 mol %), K_2CO_3 (4 mmol), and ethanol (0.05 mL) in glycerol(1 mL, 13.7 mmol) was heated for 20 h. [b]The turnover numbers (TONs) of each product and conversion of glycerol were quantitated with ^1H nuclear magnetic resonance (NMR) with an internal standard (isoniconitic acid). [c]Glycerol conversion. [d]Lactate selectivity over propylene glycol (PG).

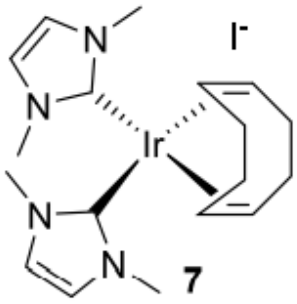

7

4.2.2. Proposed reaction mechanism and corresponding reaction energy diagram for two catalysts

To understand the strong dependence of the dramatic change of catalytic activity on the structure of Ir(biscarbene) catalysts, i.e., the tether length of biscarbene ligands, we theoretically elucidated the reaction mechanism for the catalytic conversion of inorganic carbonate/glycerol to formates/lactates using density functional theory (DFT) calculations (see Supporting Information for computation details). Since the reaction was conducted in glycerol, the polarizable continuum model using the integral equation formalism (IEFPCM) was employed to take account of the influence of glycerol (dielectric constant $\varepsilon = 42.5$). The reaction energy profiles for two catalysts, 1 and its tether-modified catalyst, were computationally examined as shown in Figures 3 and Figure S3 (Supporting Information), where we modified the length of the alkyl chain tether from n = 3 (1) to n = 1 (see Figures S5 and S6 for the optimized structures of 1 (C3) and its tether-modified catalyst (C1) during their catalytic reactions, respectively). As the COD ligand is substituted with the glycerol alkoxide at the initial step of the catalytic reaction (A → B),[55] a reaction energy diagram was constructed from the Ir(I)−alkoxy intermediate species B, where the glycerol alkoxide binds to an Ir(I) ion in a bidentate manner (Figures S3 and S4). The glycerol alkoxide in Ir(I)−alkoxy intermediate B was converted to Ir(I)−H possessing dihydroxy acetone (DHA) through a β-hydride elimination process (B → C^{TS} → D). Subsequently, an Ir(I)−H species E is formed through the detachment of DHA from the Ir(I) complex (D → E). The liberated DHA undergoes the remaining steps, i.e., dehydration, tautomerization, and intramolecular Cannizzaro reaction, to produce lactic acid.[58] The reaction barrier for the β-hydride elimination process is slightly higher for the C1 catalyst compared with that for the C3 catalyst (1) by ~3 kcal/mol, and the formation of species D for the C1 catalyst is more endothermic than that for the C3 catalyst (1) with an identical energy difference, whose value is maintained during the detachment of DHA. Therefore, the thermodynamic feature during the formation of the Ir(I)−H complex does not explain the strong dependence of the catalytic activity for the formation of formates on the length of the hydrocarbon tether as experimentally observed with 1″ and 6 (entries 8 and 9 in Table 1). The instability of the Ir(I)−H species E owing to the

endothermic DHA detachment process is compensated via binding with an inorganic bicarbonate $KHCO_3$ generated from K_2CO_3 in protic media (E → F), in which almost identical energies for the C3 and C1 catalysts, i.e., 9.8 and 9.1 kcal/mol, respectively, are released. For the reduction of inorganic bicarbonates with Ir(I)−H, two different routes are possible: (1) the direct reduction of bicarbonates via hydride transfer from the Ir(I)−H complex (see Figures 3 and S3) and (2) dehydroxylation (releasing KOH) followed by the reduction of CO_2 by the Ir(I)−H complex (Figure 3, F → G^{TS} → H).[59−61] Therefore, we investigated both pathways beginning with F to probe an energetically favorable route. Our computational result indicates that the dehydroxylation of bicarbonate (F → G^{TS} → H) to form CO_2-bound iridium complex H is a kinetically more favorable process than the direct reduction of bicarbonates on the iridium ion (Figure S3, F → K^{TS} → L) because the reaction barrier of 38.4 (46.3) kcal/mol for the dehydroxylation of the C3 (C1) catalyst is lower than that for its hydride transfer by 55.7 (57.9) kcal/mol. This result provides a crucial insight into the actual reduction reaction occurring with CO_2 bound on the iridium catalysts, not the direct reduction of bicarbonates bound on the iridium catalysts. CO_2 liberated from H was observed during the catalytic reaction (see Supporting Information). The catalytic activity dependence on the length of the hydrocarbon tether is also explained by the calculation results. The reaction barrier for the C3 catalyst is 38.4 kcal/mol, which is 7.9 kcal/mol lower than that for the C1 catalyst (46.3 kcal/mol). The overall energy change (ΔG) of G^{TS} with respect to B is also much lower for C3 (48.5 kcal/mol) than that for C1 (60.4 kcal/mol) by 11.9 kcal/mol. The dehydroxylation of bicarbonate produces a CO_2 molecule and thus results in a CO_2-coordinated Ir(I)−H complex (H). The formation of H with respect to B for the C3 catalyst (28.0 kcal/mol) is less endothermic compared with that for the C1 catalyst (34.4 kcal/mol), which also supports the higher catalytic performance of the C3 catalyst observed in the experiment. In addition, the reaction energy profile from E to H can be directly influenced by replacing the inorganic bicarbonate $KHCO_3$ with $NaHCO_3$ (Figure 3). The variations in the reaction energies with $NaHCO_3$ compared to those with $KHCO_3$ are overall within 2.5 (4.6) kcal/mol for the C3 (C1) catalyst (Figure S7). Although the difference between reaction barriers of C3 and C1 catalysts is slightly reduced by ~3 kcal/mol due to $NaHCO_3$, the C3 catalyst consistently shows higher reactivity than the C1 catalyst. The CO_2 molecule bound on the Ir ion is reduced by the hydride

transfer from the Ir(I)−H complex with the reaction barrier of 59.5 (56.8) kcal/mol for the C3 (C1) catalyst and leads to the formation of formates, which are further replaced with a glycerol molecule in the medium (H → I^{TS} → J → B′). Based on the DFT calculation of key intermediates, we propose a general mechanism of Ir-(biscarbene)-catalyzed transfer hydrogenation of carbonates and glycerol, in addition to the effect of the ligand structure. This transfer hydrogenation is composed of two critical steps: β-hydride elimination of glycerol and the reduction of CO_2 derived from bicarbonates. Comparing reaction barriers of each step, it appears CO_2 reduction is more challenging than β-hydride elimination of glycerol, which is reflected on the lower TON of formates than lactates.

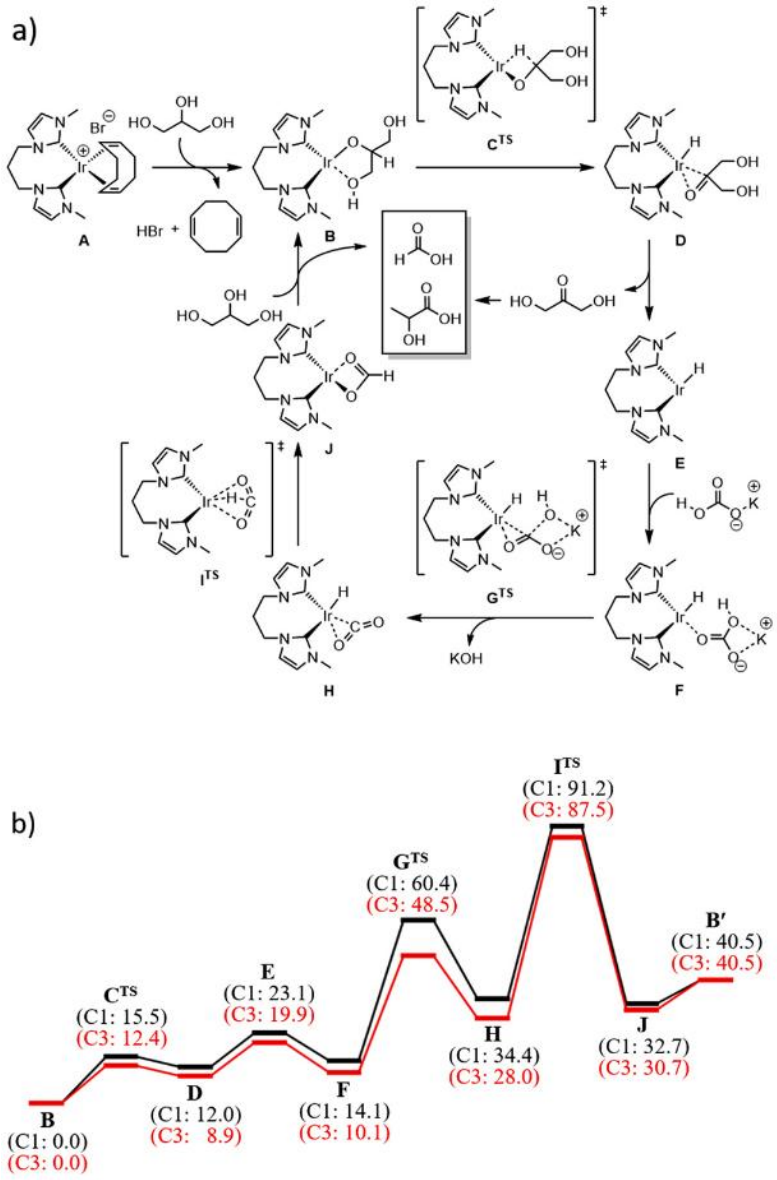

Figure 3. (a) Proposed reaction mechanism for the simultaneous conversion of inorganic carbonate/glycerol to formate/lactate and (b) the corresponding reaction energy diagram for two catalysts, 1 and its tether-modified catalyst, where we modified the length of the alkyl chain tether from n = 3 (1) to n = 1. C3 and C1 denote catalyst 1 and its tether-modified catalyst, respectively (see Figure S1 for the reaction energy diagram including the direct reduction of bicarbonates on the iridium ion). A reaction energy diagram was constructed using PBE0-D3/6-311++G(d,p)//PBE0-D3/6-31G(d,p) calculations (see Figure S4 for the reaction energy diagram constructed using MN15/6-311++G(d,p)//MN15/6-31G(d,p) calculations). All the energy values are related to the Gibbs free energy (ΔG in kcal/mol) at 298.15 K and 1 atm.

4.2.3. The dependence of the catalytic activity on the length of the hydrocarbon tether of the C3 and C1 catalysts

The dependence of the catalytic activity on the length of the hydrocarbon tether of the C3 and C1 catalysts was explained with the difference in energy during the formation of CO_2 by dehydroxylation of bicarbonates as above-mentioned. Furthermore, we investigated the influence of the tether length on the geometry of Ir(biscarbene) catalysts and on its binding character with bicarbonates and CO_2 for further clarifying experimental observation. The prominent geometric difference between the C3 and C1 catalysts depending on the tether length was examined with the geometry of Ir(I)−H complex (E). The square-planar (*sq*) plane of the central Ir(I) ion including a vacant site in the C3 catalyst is perpendicular to the five-membered rings of carbene moieties whereas the corresponding Ir(I) sq-plane of the C1 catalyst is roughly coplanar to the carbene moieties (Figure 4a,b). These differences in geometric features may influence the binding property of the Ir(I) ion toward incoming reactants. The vacant site of the C3 catalyst is sterically less hindered, resulting in more accessible coordination with incoming reagents compared with that for the C1 catalyst. Although an N-heterocyclic carbene (NHC) ligand is known to be a strong σ-donor and weak π-acceptor,[62] the electron density of the Ir(I) ion of the C1 catalyst can be reduced owing to the coplanarity between the Ir(I) *sq*-plane and the five-membered rings of the carbene moieties, whose geometry is favorable for π-conjugation. In contrast, the perpendicular orientation between them in the C3 catalyst prevents the decrease in the electron density of the central Ir(I) ion (Figure S8). The estimated binding energies of the C3 Ir(I)−H complex with $KHCO_3$ and CO2 are 9.8 and 23.4 kcal/mol for the C3 catalyst, respectively, which are larger than those for the C1 catalyst by 0.8 and 3.2 kcal/mol, respectively. Therefore, the stronger binding of the C3 Ir(I)−H complex with the CO_2 molecule causes its higher catalytic activity compared with that of the C1 Ir(I)−H complex. The CO_2-coordinated Ir(I)−H complexes (H) for both C3 and C1 catalysts can be described with an η^2-type π-bonding complex, in which the molecular plane of CO_2 is perpendicular to the Ir(I) *sq*-plane. The Ir(I)− C* (C* denotes the C atom of CO_2 molecule) and Ir(I)−O bond lengths for the C3 (C1) catalysts are 1.96 (1.95) and 2.27 (2.31) Å, respectively. The bending angle of CO_2 bonding with the C3 (C1) Ir(I)−H

complex is 136.2° (134.9°). While the distance between Ir(I) and CO_2 and the bending angle do not show significant differences between the C3 and C1 catalysts, the relative orientation of CO_2 to the *sq*-geometry of the Ir(I) ion shows a distinct difference between the C3 and the C1 catalysts. The angular displacement of CO_2 from the Ir(I) sq-plane for the C3 (C1) catalyst, i.e., the angle between the Ir(I) *sq*-plane and the bond between Ir(I) and the closest O atom, is 20.9° (29.9°), which indicates that the binding orientation of the CO_2 molecule to the vacant site of the C3 Ir(I)−H complex is closer to the sq-geometry than that of the C1 CO_2-coordinated Ir(I)−H complex (Figure 4c,d). The favorable formation of *sq*-geometry in the C3 catalyst can contribute to a more efficient orbital interaction than in the C1 catalyst (Figure S9). Strong tether length effects of chelating biscarbene−Rh complexes were reported.[63,64] The C−H···O hydrogen bonding between CO_2 and the wing-tip methyl groups may also have an influence on the formation of sqgeometry during complexation. The role of C−H···O hydrogen bonding is more prominent in determining the stability of the transition state for the dehydroxylation of bicarbonate (G^{TS}). While only the KOH moiety interacts with a wing-tip methyl group in the C1 catalyst, two wing-tip methyl groups of the C3 catalyst can effectively stabilize both CO_2 and KOH moieties and thus lead to the low activation barrier for dihydroxylation (Figure 4e,f). Our computational results revealed that the catalytic activity of the C3 catalyst superior to that of the C1 catalyst depending on the tether length between two carbene groups can be reasonably interpreted with the properties resulting from their geometries, such as the higher electron density of the central Ir(I) ion, a lower steric hindrance favorable for the approach of reagents, and more efficient hydrogen bonding with reagents in contrast to those for the C1 catalyst.

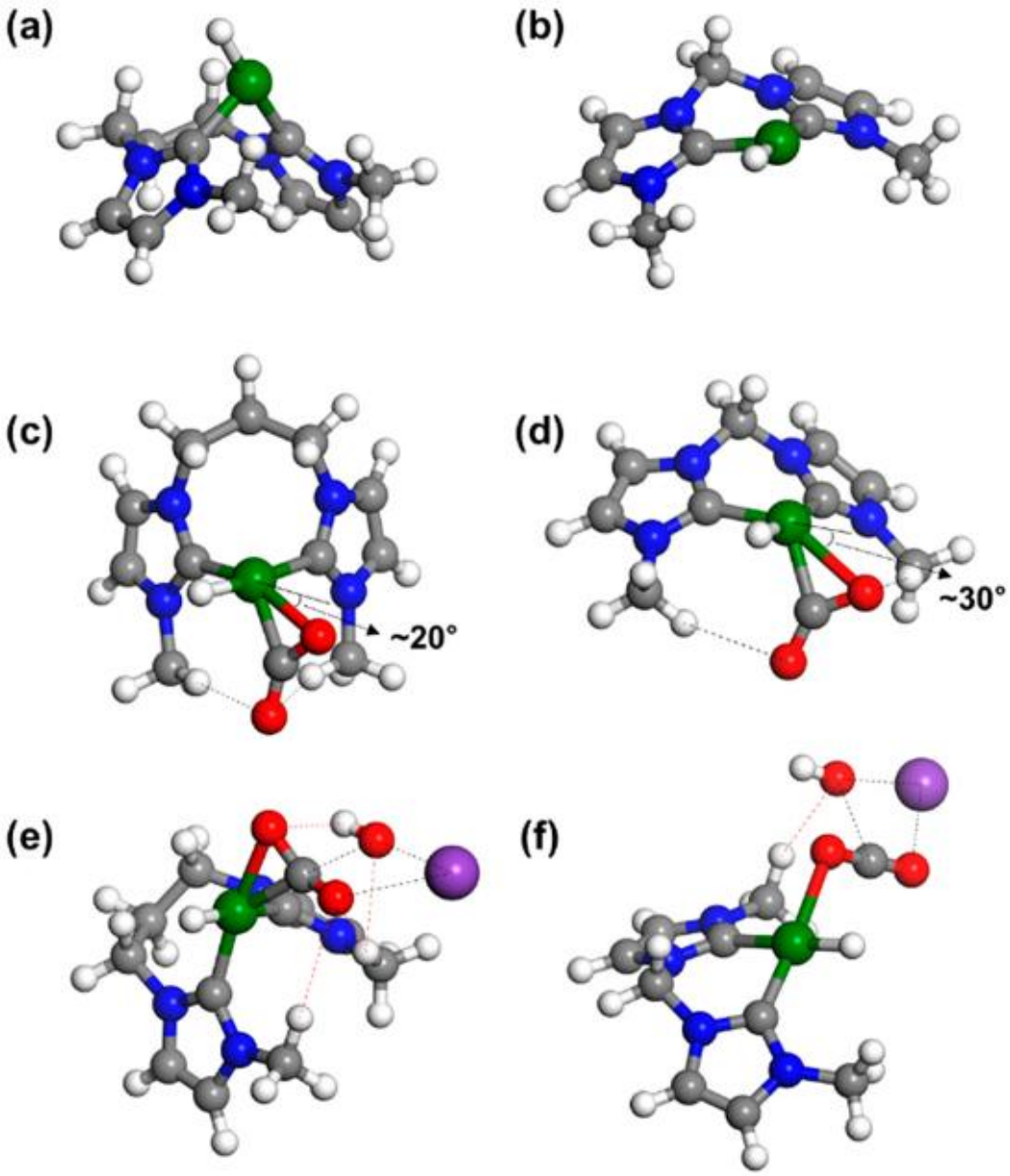

Figure 4. Optimized geometries of (a, b) Ir(I)−H complex E, (c, d) CO2-coordinated Ir(I)−H complex H, and (e, f) transition state for the dehydroxylation of bicarbonate GTS for (a, c, e) C3 (1) catalyst and (b, d, f) C1 catalyst. The O−H···O and C−H···O hydrogen bonds are indicated by red-colored dashed lines [Ir, green; K, purple; O, red; N, blue; C, gray; H, white].

5. Conclusion

In this paper, two topics related to eco-friendliness were dealt with. In the first topic, CO_2 conversion, among various methods for reusing the C1 source, a catalyst for simultaneously converting inorganic carbonate to formate and lactate through a catalytic reaction with waste glycerol was studied. Efficient and stable Ir-containing biscarbene ligand was studied. The formate production rate was improved by using a biscarbene catalyst. Through computational research using the DFT method, it was confirmed that the formation of CO_2 molecules occurs through b-hydride elimination of glycerol and dehydroxylation of bicarbonate during the catalytic reaction. Based on this, the mechanism of conversion of carbonate and glycerol through hydrogen catalytic conversion presented. In addition, it was confirmed that the number of carbons linking the biscarbene ligand was closely related to the catalytic activity. When there were three linker carbons, the ligand-coordinated Ir-complex showed coordinated sites more accessible to bicarbonate and high electron density. , confirmed that C3-ligand was more preferred than C1-ligand due to the interaction between the wing-tip methyl group and CO_2, which is a key function to increase the CO_2 reduction efficiency for formate formation. Finally, a simultaneous conversion method that can reduce the use of toxic substances with milder conditions compared to the previously reported studies of recycling carbonate was developed, and it was confirmed that it can be used in the actual process.

In the second topic, rearrangement of oxaziridine to amide, a reaction in which selective rearrangement of oxaziridine to amide occurs under mild conditions and weak bases through visible light photoreduction catalysts through experimental and computational studies was introduced. The developed method made it possible to prepare various amides from oxaziridine with good functional group tolerance and good yield. The described approach offers several advantages as it addresses the limitations of existing methods by avoiding the use of high-energy light sources and stoichiometric amounts of strong bases. Additionally, control experiments and DFT calculations were performed to reveal a weak base-promoted (DMF or trifluoroacetate) selective rearrangement of oxaziridine to amide via the SET mechanism.

6. Supporting information

I. Reaction Setup

Irradiation of photochemical reactions was carried out using two MR16 3W blue LED spotlight lamp [*Specification of 3W blue LED: Power (3W), Voltage (12V), Wavelength (450 nm)]. The pictures of two utilized spotlight lamps and their description are given below:

MR16 3W blue LEDs spotlight

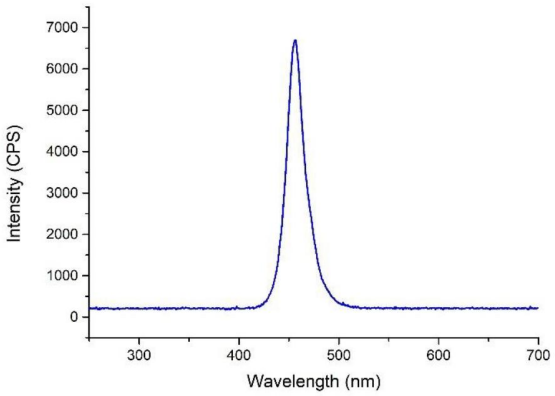

Emission spectrum of 3W blue LEDs

Figure S1. Description for 3 W blue LED spotlight lamp

To photoredox reactions, two MR16 3W blue LEDs spotlight lamp are positioned 3 cm away from the reaction vial using customized reactor that was made by acrylic plate.

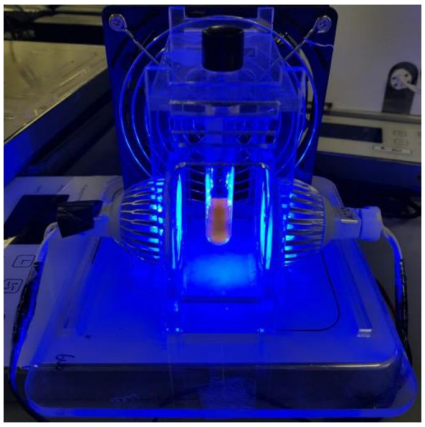

** A fan was used to maintain the internal and external temperature of the reaction vial at 20 ~ 30 °C.

Figure S2. reaction setup

III. Preparation of oxaziridines 1

All the utilized aryl and alkyl oxaziridines 1 had been prepared by following the reported protocol.[1]

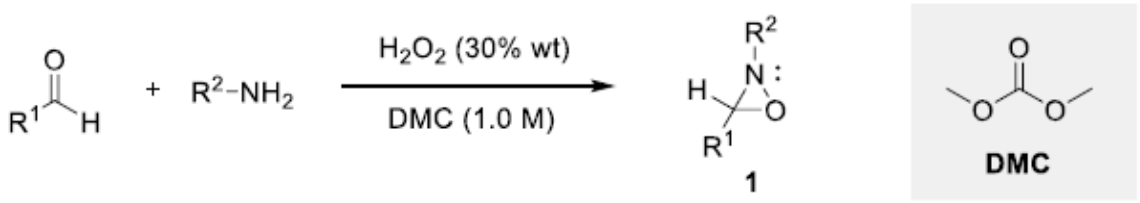

IV. General procedure and characterization data of products

A. General procedure for rearrangement oxaziridines 1 to amides 2

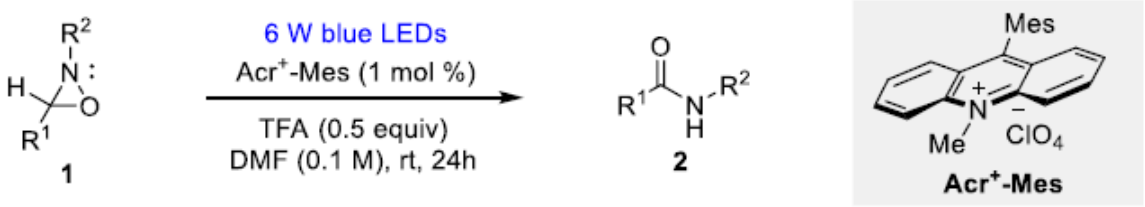

To a re-sealable pressure tube (13 x 100 mm) with a magnetic stir bar was charged with oxaziridine 1(0.2 mmol, 1.0 equiv) and 9-mesityl-10-methylacridinium perchlorate (Acr^+-Mes) (0.82 mg, 0.002 mmol, 1.0 mol %) under argon atmosphere. The reaction mixture was dissolved by degassed DMF (2 mL, 0.1 M for 1). The reaction mixture was irradiating with 2 x 3W blue LEDs using our customized milligram scale reaction set up (as shown in Figure S2) under constant stirring condition at room temperature for 24h. After the reaction was completed, the solvent was removed under reduced pressure and residue was purified by silica gel column chromatography contained ethyl acetate/hexanes as the eluent to afford the corresponding amide 2.

V. Control experiments

- Deuterium labelling experiment

To get insight about the proton transfer from carbon to nitrogen at oxaziridine 1a for our proposed mechanism, control experiments were performed using deuterated oxaziridine 1a-D as starting material keeping other parameters unchanged. By 1H NMR analysis of crude mixture, it was confirmed that deuterium shifts from carbon to the nitrogen of the amide 2a-D. The decrease in the deuterium ratio is expected to be due to the trace amount of water in the DMF. And w measured kinetic isotope effect (KIE) value for rearrangement from oxazridine 1a to amide 2a by compare reaction yield of oxaziridine 1a and oxaziridine 1a-D. The KIE values indicate that proton transfer steps are a late-determining step, which is consistent with the proposed mechanism.

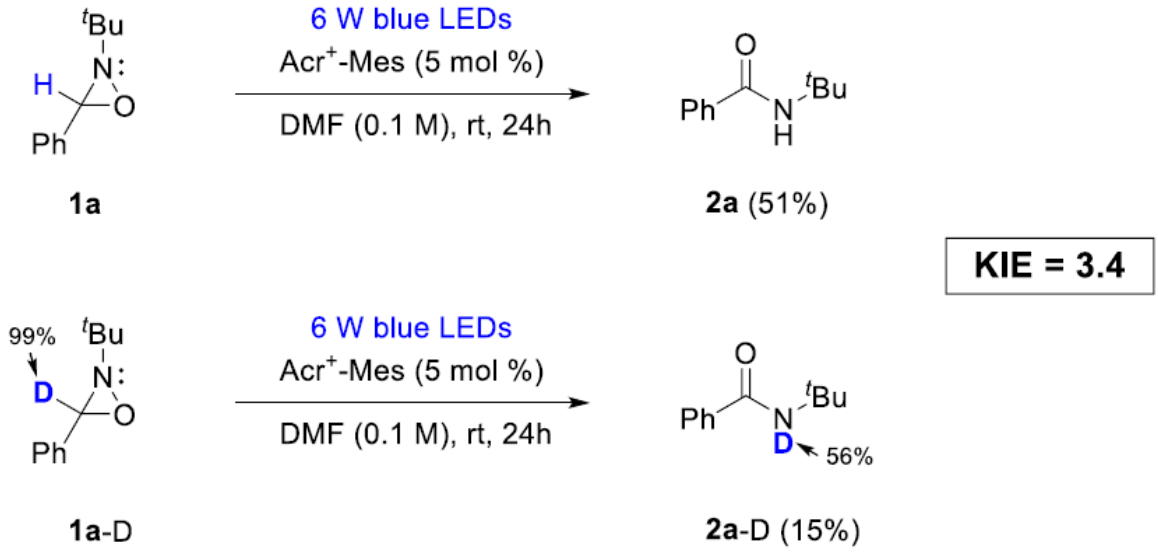

Scheme S1. Deuterium labelling experiment

VI. DFT calculation

- Computation details

A computational study based on density functional theory (DFT) was performed to verify the experimentally proposed reaction mechanism and the detailed dependence of chemical reactivity on the base species. The molecular geometries were optimized using the hybrid PBE0 functional[10] and 6-31G(d,p) basis set implemented in Gaussian 16 program suite.[11] The frequency calculations were carried out with the same functional and basis set as those used in the geometry optimization to confirm local minima and to obtain a thermal contribution to the reaction energy diagram which is corrected by Gibbs free energy obtained at 298.15 K and 1 atm. The polarizable continuum model using the integral equation formalism (IEFPCM) was employed to take account for the influence of solvent medium, dimethylformamide (DMF) [ε = 37.219] and acetonitrile (MeCN) [dielectric constant ε = 35.688], on geometric and electronic structures.[12] Spin density was analyzed to elucidate the spatial distribution of unpaired electron in oxidized oxaziridine radical species.

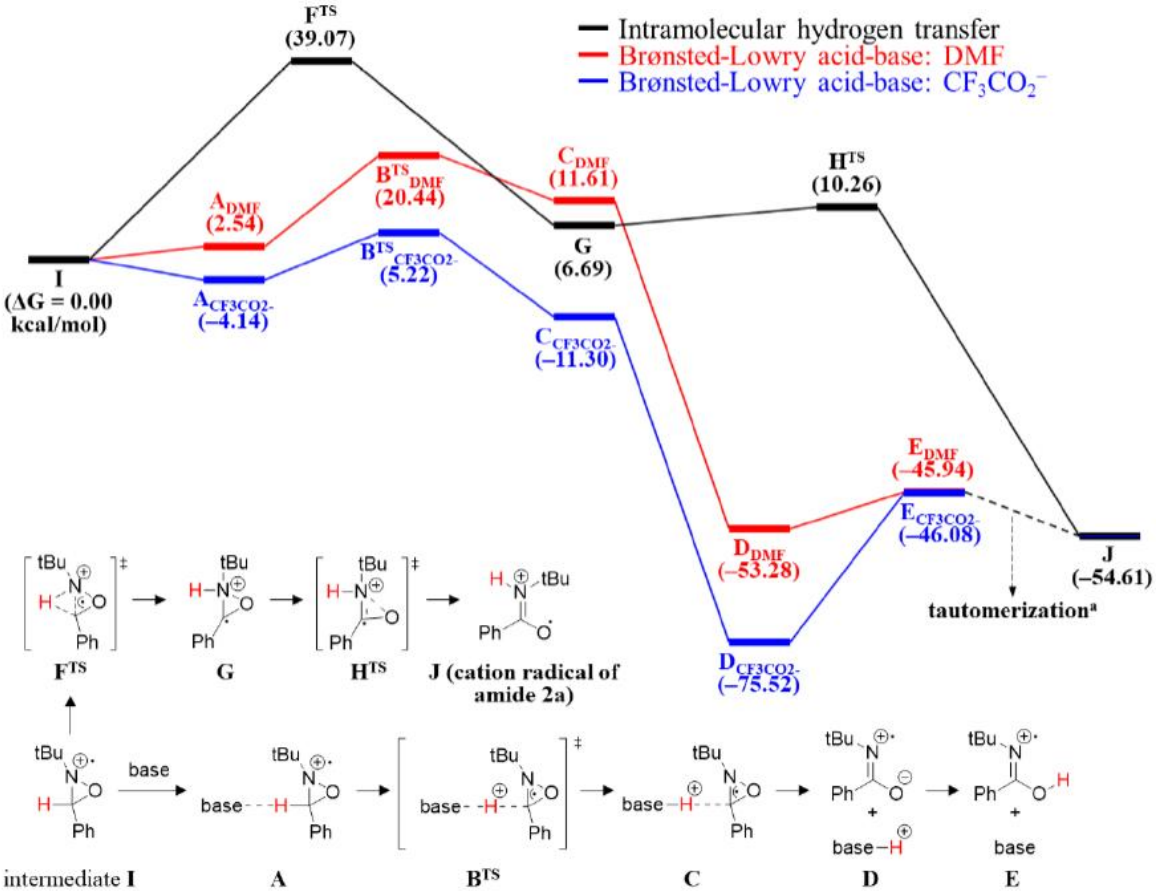

Figure S12. Reaction energy profiles for the rearrangement of cation radical intermediate I, i.e., oxidized oxaziridine 1a, via Brønsted–Lowry acid–base reaction mechanism (from I to E), where DMF (red line) and trifluoroacetate (blue line) were used as base species, and via intramolecular hydrogen transfer mechanism (from I to J, black line). The solvent medium of DMF was considered using the IEFPCM method for evaluating all reaction energy profiles. All energy values are related to the Gibbs free energy (ΔG in kcal/mol) at 298.15 K and 1 atm. ([a]Notably, it is expected that tautomerization from E to J did not occur in our experiment because the one-electron reduction of cation radical E is generally faster than tautomerization.)

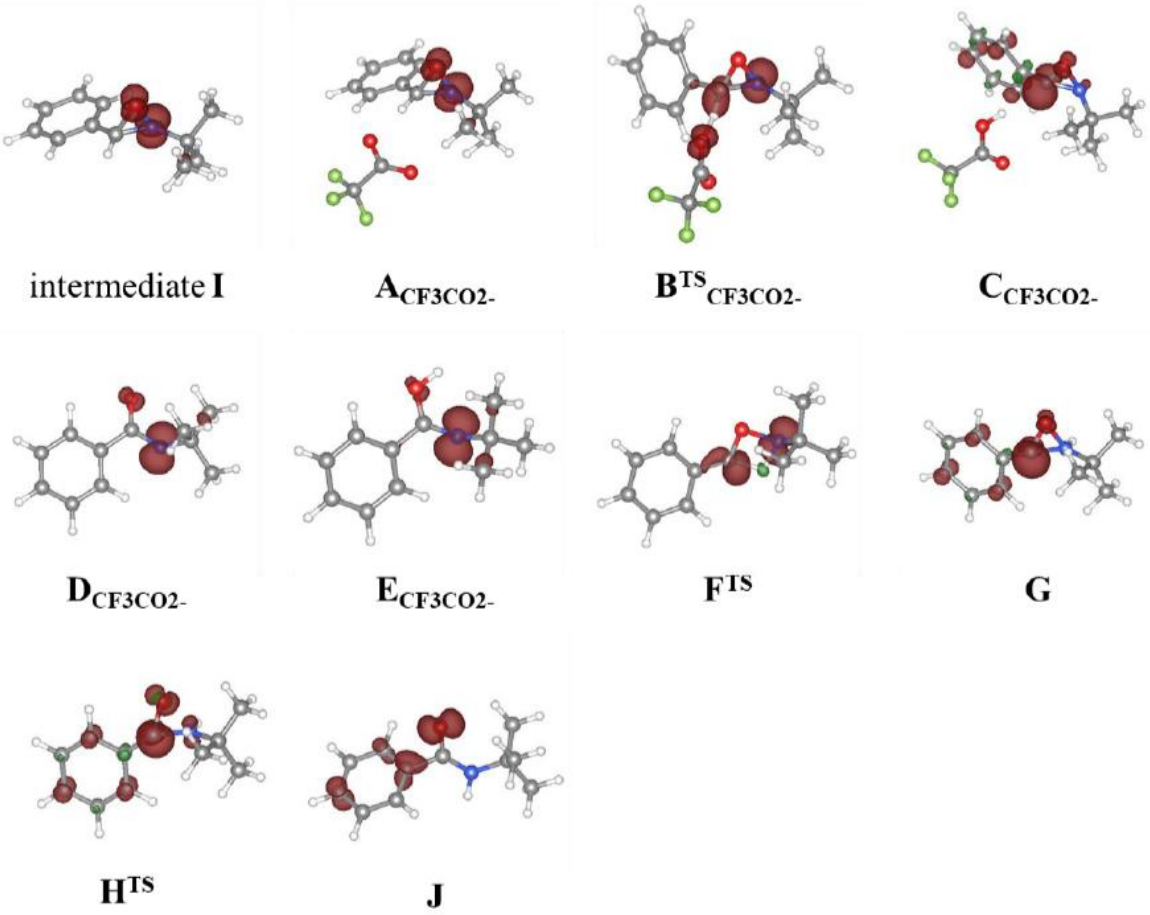

Figure S13. Optimized geometries and spin densities for the rearrangement of cation radical intermediate I, i.e., oxidized oxaziridine 1a, via Brønsted–Lowry acid–base reaction mechanism (from I to E), where trifluoroacetate was used as base species, and intramolecular hydrogen transfer mechanism (from I to J). See Figure S1 for corresponding reaction energy profiles.

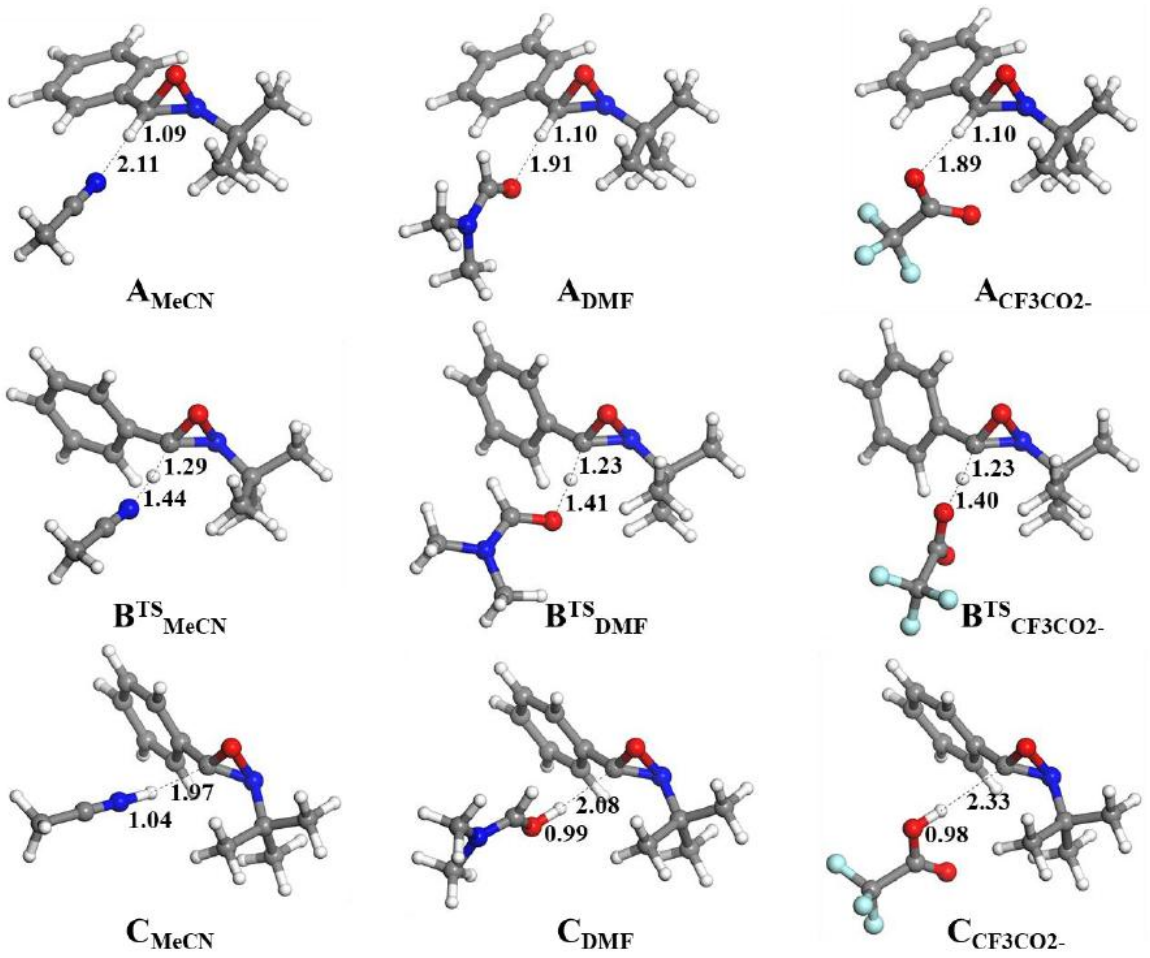

Figure S14. Optimized geometries for the deprotonation of intermediate I with base species, MeCN, DMF, and trifluoroacetate. Selected interatomic distances are in Å.

VII. Characterization data of amides 2

N-(tert-butyl)benzamide (2a).[2]

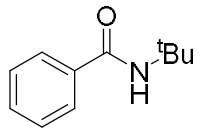

2a

Following the general procedure using 15% ethyl acetate in hexanes as eluant, **2a** was obtained as a white solid (33.7 mg, 95% yield); R_f= 0.35 (ethyl acetate:hexanes, 1:5); ^{1}H NMR (300 MHz, $CDCl_3$) δ 7.84 – 7.60 (m, 2H), 7.60 – 7.31 (m, 3H), 6.01 (s, 1H), 1.45 (s, 9H).; ^{13}C NMR (75 MHz, $CDCl_3$) δ 166.99, 135.96, 131.12, 128.51, 126.78, 51.65, 28.93.

N-(tert-butyl)-4-methylbenzamide (2b).[3]

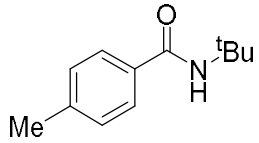

2b

Following the general procedure using 15% ethyl acetate in hexanes as eluant, **2b** was obtained as a white solid (26.8 mg, 70% yield); R_f= 0.30 (ethyl acetate:hexanes, 1:5); ^{1}H NMR (300 MHz, $CDCl_3$) δ 7.64 (d, *J* = 8.0 Hz, 2H), 7.22 (d, *J* = 8.0 Hz, 2H), 5.96 (s, 1H), 2.40 (s, 3H), 1.49 (s, 9H).; ^{13}C NMR (75 MHz, $CDCl_3$) δ 166.95, 141.48, 133.14, 129.20, 126.79,

N,4-di-tert-butylbenzamide (2c).[3]

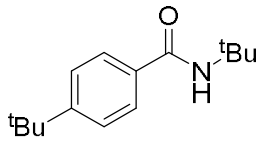

2c

Following the general procedure using 20% ethyl acetate in hexanes as eluant, **2c** was obtained as a white solid (25.3mg, 54% yield); R_f= 0.30 (ethyl acetate:hexanes, 1:5); ^{1}H NMR (300 MHz, $CDCl_3$) δ 7.71 – 7.57 (m, 2H), 7.49 – 7.33 (m, 2H), 5.96 (s, 1H), 1.49 (s, 9H), 1.35 (s, 9H).; ^{13}C NMR (75 MHz, $CDCl_3$) δ 166.97, 154.61, 133.17, 126.63, 125.50, 51.59, 34.96,

N-(tert-butyl)-[1,1'-biphenyl]-4-carboxamide (2d).[4]

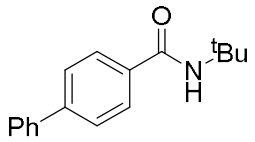

2d

Following the general procedure using 20% ethyl acetate in hexanes as eluant, **2d** was obtained as a white solid (45.6 mg, 90% yield); R_f= 0.30 (ethyl acetate:hexanes, 1:5); ^{1}H NMR (300 MHz, $CDCl_3$) δ 7.85 – 7.75 (m, 2H), 7.67 – 7.54 (m, 4H), 7.51 – 7.32 (m, 3H), 6.07 (s, 1H), 1.50 (s, 9H).; ^{13}C NMR (75 MHz, $CDCl_3$) δ 166.70, 143.90, 140.15, 134.63, 128.97,

N-(tert-butyl)-4-methoxybenzamide (2e).[3]

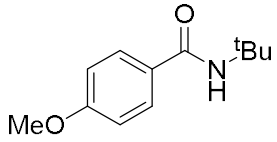

2e

Following the general procedure using 20% ethyl acetate in hexanes as eluant, **2e** was obtained as a white solid (12.5 mg, 30% yield); R_f= 0.30 (ethyl acetate:hexanes, 1:5); ^{1}H NMR (300 MHz, $CDCl_3$) δ 7.73 – 7.62 (m, 2H), 6.95 – 6.85 (m, 2H), 5.88 (s, 1H), 3.83 (s, 3H), 1.46 (s, 9H).; ^{13}C NMR (75 MHz, $CDCl_3$) δ 166.57, 161.98, 128.58, 128.32, 113.74, 55.53, 51.59,

N-(tert-butyl)-4-fluorobenzamide (2f).[3]

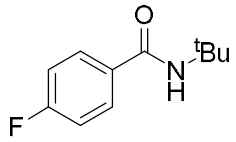

2f

Following the general procedure using 10% ethyl acetate in hexanes as eluant, **2f** was obtained as a white solid (25.0 mg, 64% yield); R_f= 0.40 (ethyl acetate:hexanes, 1:5); ^{1}H NMR (300 MHz, $CDCl_3$) δ 7.82 – 7.61 (m, 2H), 7.13 – 6.94 (m, 2H), 5.99 (s, 1H), 1.44 (s, 9H).; ^{13}C NMR (75 MHz, $CDCl_3$) δ 166.17, 165.98, 162.84, 132.17, 132.12, 129.16, 129.04, 115.59, 115.30,

N-(tert-butyl)-4-chlorobenzamide (2g).[3]

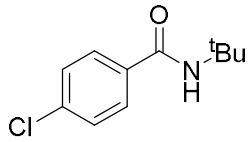

2g

Following the general procedure using 10% ethyl acetate in hexanes as eluant, **2g** was obtained as a white solid (40.7 mg, 96% yield); R_f = 0.40 (ethyl acetate:hexanes, 1:10); ^{1}H NMR (300 MHz, $CDCl_3$) δ 7.69 – 7.59 (m, 2H), 7.40 – 7.30 (m, 2H), 5.95 (s, 1H), 1.45 (s, 9H).; ^{13}C NMR (75 MHz, $CDCl_3$) δ 165.96, 137.32, 134.36, 128.76, 128.29, 51.90, 28.93.

4-bromo-N-(tert-butyl)benzamide (2h).[3]

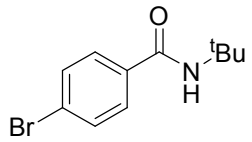

2h

Following the general procedure using 10% ethyl acetate in hexanes as eluant, **2h** was obtained as a white solid (45.1 mg, 88% yield); R_f = 0.40 (ethyl acetate:hexanes, 1:10); ^{1}H NMR (300 MHz, $CDCl_3$) δ 7.62 – 7.46 (m, 4H), 5.95 (s, 1H), 1.45 (s, 9H).; ^{13}C NMR (75 MHz, $CDCl_3$) δ 166.04, 134.82, 131.73, 128.49, 125.74, 51.91, 28.92.

N-(tert-butyl)-4-nitrobenzamide (2i).[2]

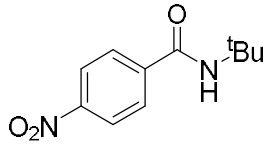

2i

Following the general procedure using 25% ethyl acetate in hexanes as eluant, **2i** was obtained as a white solid (33.8 mg,76% yield); R_f= 0.20 (ethyl acetate:hexanes, 1:5); ^{1}H NMR (300 MHz, $CDCl_3$) δ 8.27 – 8.16 (m, 2H), 7.91 – 7.80 (m, 2H), 6.10 (s, 1H), 1.47 (s, 9H).; ^{13}C NMR (75 MHz, $CDCl_3$) δ 165.01, 149.35, 141.63, 128.06, 123.79, 52.38, 28.81.

methyl 4-(tert-butylcarbamoyl)benzoate (2j).[2]

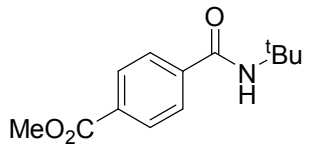

2j

Following the general procedure using 25% ethyl acetate in hexanes as eluant, **2j** was obtained as a white solid (46.9 mg, 99% yield); R_f= 0.25 (ethyl acetate:hexanes, 1:5); ^{1}H NMR (300 MHz, $CDCl_3$) δ 8.13 – 8.03 (m, 2H), 7.87 – 7.72 (m, 2H), 5.96 (s, 1H), 3.94 (s, 3H), 1.48 (s, 9H).; ^{13}C NMR (75 MHz, $CDCl_3$) δ 166.44, 166.14, 139.93, 132.33, 129.79, 126.89, 52.43,

N-(tert-butyl)-2-methylbenzamide (2k).[3]

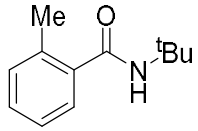

2k

Following the general procedure using 20% ethyl acetate in hexanes as eluant, **2k** was obtained as a white solid (25.2 mg, 66% yield); R_f= 0.30 (ethyl acetate:hexanes, 1:5); ^{1}H NMR (300 MHz, $CDCl_3$) δ 7.35 – 7.22 (m, 2H), 7.22 – 7.11 (m, 2H), 5.56 (s, 1H), 2.43 (s, 3H), 1.46 (s, 9H).; ^{13}C NMR (75 MHz, $CDCl_3$) δ 169.81, 138.01, 135.58, 130.92, 129.51, 126.54, 125.76,

N-(tert-butyl)-2-methoxybenzamide (2l).[3]

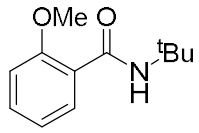

2l

Following the general procedure using 20% ethyl acetate in hexanes as eluant, **2l** was obtained as a white solid (37.3 mg, 90% yield); R_f= 0.30 (ethyl acetate:hexanes, 1:5); ^{1}H NMR (300 MHz, $CDCl_3$) δ 8.23 – 8.13 (m, 1H), 7.84 (s, 1H), 7.48 – 7.36 (m, 1H), 7.13 – 7.01 (m, 1H), 6.99 – 6.90 (m, 1H), 3.95 (s, 3H), 1.46 (s, 9H).; ^{13}C NMR (75 MHz, $CDCl_3$) δ 164.20,

N-(tert-butyl)-2-chlorobenzamide (2m).[3]

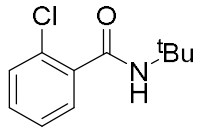

2m

Following the general procedure using 10% ethyl acetate in hexanes as eluant, **2m** was obtained as a white solid (37.3 mg, 88% yield); R_f= 0.4 (ethyl acetate:hexanes, 1:10); ^{1}H NMR (300 MHz, $CDCl_3$) δ 7.64 – 7.54 (m, 1H), 7.41 – 7.27 (m, 3H), 5.91 (s, 1H), 1.48 (s, 9H).; ^{13}C NMR (75 MHz, $CDCl_3$) δ 165.98, 136.60, 130.94, 130.51, 130.15, 129.85, 127.14, 52.31,

N-(tert-butyl)-3-methylbenzamide (2n).[3]

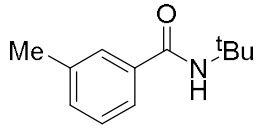

2n

Following the general procedure using 20% ethyl acetate in hexanes as eluant, **2n** was obtained as a white solid (32.9 mg, 86% yield); R_f= 0.30 (ethyl acetate:hexanes, 1:5); ^{1}H NMR (300 MHz, $CDCl_3$) δ 7.58 – 7.44 (m, 2H), 7.34 – 7.22 (m, 2H), 5.96 (s, 1H), 2.38 (s, 3H), 1.47 (s, 9H).; ^{13}C NMR (75 MHz, $CDCl_3$) δ 167.20, 138.38, 135.99, 131.87, 128.43, 127.59, 123.74,

N-(tert-butyl)-3-methoxybenzamide (2o).[3]

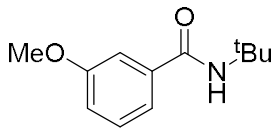

2o

Following the general procedure using 20% ethyl acetate in hexanes as eluant, **2o** was obtained as a white solid (40.2 mg, 97% yield); R_f= 0.30 (ethyl acetate:hexanes, 1:5); ^{1}H NMR (300 MHz, $CDCl_3$) δ 7.37 – 7.20 (m, 3H), 7.10 – 6.96 (m, 1H), 5.94 (s, 1H), 3.85 (s, 3H), 1.47 (s, 9H).; ^{13}C NMR (75 MHz, $CDCl_3$) δ 166.79, 159.84, 137.46, 129.46, 118.49, 117.40, 112.18,

N-(tert-butyl)-3-chlorobenzamide (2p).[3]

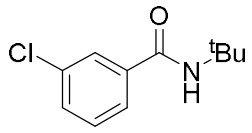

2p

Following the general procedure using 10% ethyl acetate in hexanes as eluant, **2p** was obtained as a white solid (38.1mg, 90% yield); R_f = 0.40 (ethyl acetate:hexanes, 1:10); ^{1}H NMR (300 MHz, $CDCl_3$) δ 7.70 – 7.63 (m, 1H), 7.60 – 7.50 (m, 1H), 7.43 – 7.32 (m, 1H), 7.34 – 7.23 (m, 1H), 6.14 (s, 1H), 1.45 (s, 9H).; ^{13}C NMR (75 MHz, $CDCl_3$) δ 165.66, 137.74,

N-(tert-butyl)furan-2-carboxamide (2q).[2]

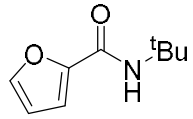

2q

Following the general procedure using 30% ethyl acetate in hexanes as eluant, **2q** was obtained as a white solid (20.1 mg, 60% yield); R_f= 0.20 (ethyl acetate:hexanes, 1:4); ^{1}H NMR (300 MHz, $CDCl_3$) δ 7.42 – 7.31 (m, 1H), 7.04 (d, *J* = 3.5 Hz, 1H), 6.46 (dd, *J* = 3.5, 1.8 Hz, 1H), 6.19 (s, 1H), 1.45 (s, 9H).; ^{13}C NMR (75 MHz, $CDCl_3$) δ 157.92, 148.94, 143.41, 113.58,

N-(tert-butyl)isonicotinamide (2r).[5]

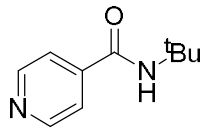

2r

Following the general procedure using 30% ethyl acetate in hexanes as eluant, **2r** was obtained as a white solid (28.6 mg, 80% yield); R_f= 0.20 (ethyl acetate:hexanes, 1:4); ^{1}H NMR (300 MHz, $CDCl_3$) δ 8.70 – 8.62 (m, 2H), 7.57 – 7.49 (m, 2H), 6.14 (s, 1H), 1.44 (s, 9H).; ^{13}C NMR (75 MHz, $CDCl_3$) δ 164.97, 150.49, 143.02, 120.90, 52.22, 28.79.

N-(tert-butyl)hexanamide (2s).

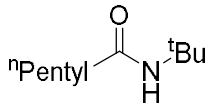

2s

Following the general procedure using 5% ethyl acetate in hexanes as eluant, **2s** was obtained as a white solid (27.5 mg, 80% yield); R_f = 0.40 (ethyl acetate:hexanes, 1:15); ^{1}H NMR (300 MHz, $CDCl_3$) δ 5.30 (s, 1H), 2.06 (d, *J* = 7.1 Hz, 2H), 1.57 (tt, *J* = 7.6, 7.1 Hz, 2H), 1.34 (d, *J* = 7.3 Hz, 9H), 1.30 – 1.18 (m, 4H), 0.87 (t, *J* = 6.7 Hz, 3H).; ^{13}C NMR (75 MHz, $CDCl_3$) δ

N-(tert-butyl)heptanamide (2t).

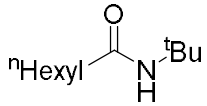

2t

Following the general procedure using 5% ethyl acetate in hexanes as eluant, **2t** was obtained as a white solid (26.3 mg, 71% yield); R_f = 0.40 (ethyl acetate:hexanes, 1:15); ^{1}H NMR (300 MHz, $CDCl_3$) δ 5.28 (s, 1H), 2.06 (t, *J* = 7.5 Hz, 2H), 1.65 – 1.49 (m, 2H), 1.32 (s, 9H), 1.30 – 1.23 (m, 6H), 0.86 (t, *J* = 6.6 Hz, 3H).; ^{13}C NMR (75 MHz, $CDCl_3$) δ 172.67, 51.12, 37.86,

N-(tert-butyl)isobutyramide (2u).[6]

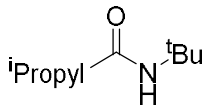

2u

Following the general procedure using 15% ethyl acetate in hexanes as eluant, **2u** was obtained as a white solid (15.5 mg, 54% yield); R_f = 0.40 (ethyl acetate:hexanes, 1:15); ^{1}H NMR (300 MHz, $CDCl_3$) δ 5.24 (s, 1H), 2.20 (h, *J* = 6.8 Hz, 1H), 1.33 (s, 9H), 1.10 (d, *J* = 6.9 Hz, 6H).; ^{13}C NMR (75 MHz, $CDCl_3$) δ 176.54, 50.94, 36.47, 28.95, 19.82.

N-(tert-butyl)-3-methylbutanamide (2v).[2]

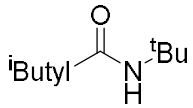

2v

Following the general procedure using 5% ethyl acetate in hexanes as eluant, **2v** was obtained as a white solid (18.9 mg, 60% yield); R_f = 0.40 (ethyl acetate:hexanes, 1:15); ^{1}H NMR (300 MHz, $CDCl_3$) δ 5.22 (s, 1H), 2.17 – 2.01 (m, 1H), 1.93 (d, *J* = 7.2 Hz, 2H), 1.34 (s, 9H), 0.93 (d, *J* = 6.5 Hz, 6H).; ^{13}C NMR (75 MHz, $CDCl_3$) δ 172.04, 51.08, 47.10, 28.87, 26.26, 22.40.

N-(tert-butyl)cyclohexanecarboxamide (2w).[7]

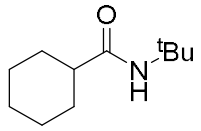

2w

Following the general procedure using 10% ethyl acetate in hexanes as eluant, **2w** was obtained as a white solid (31.6 mg, 86% yield); R_f = 0.30 (ethyl acetate:hexanes, 1:15); ^{1}H NMR (300 MHz, $CDCl_3$) δ 5.28 (s, 1H), 1.95 (tt, *J* = 11.7, 3.4 Hz, 1H), 1.86 – 1.72 (m, 4H), 1.70 – 1.60 (m, 1H), 1.50 – 1.35 (m, 2H), 1.33 (s, 9H), 1.29 – 1.18 (m, 3H).; ^{13}C NMR (75 MHz, $CDCl_3$) δ 175.70, 50.85, 46.41, 29.87, 28.96, 25.87.

N-(tert-butyl)cinnamamide (2x).[2]

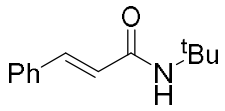

2x

Following the general procedure using 20% ethyl acetate in hexanes as eluant, **2x** was obtained as a white solid (24.4mg, 60% yield); R_f = 0.30 (ethyl acetate:hexanes, 1:5);

N-propylbenzamide (2y).[8]

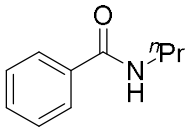

2y

Following the general procedure using 15% ethyl acetate in hexanes as eluant, **2y** was obtained as a white solid (30.1 mg, 92% yield); R_f= 0.35 (ethyl acetate:hexanes, 1:5); ^{1}H NMR (300 MHz, $CDCl_3$) δ 7.81 – 7.68 (m, 2H), 7.52 – 7.32 (m, 3H), 6.40 (s, 1H), 3.39 (q, *J* = 6.4 Hz, 2H), 1.70 – 1.50 (m, 2H), 0.96 (t, *J* = 7.4 Hz, 3H).; ^{13}C NMR (75 MHz, $CDCl_3$) δ 167.72,

N-isopropylbenzamide (2z).[2]

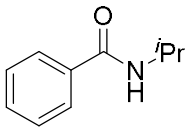

2z

Following the general procedure using 15% ethyl acetate in hexanes as eluant, **2z** was obtained as a white solid (31.0 mg, 95% yield); R_f= 0.35 (ethyl acetate:hexanes, 1:5); ^{1}H NMR (300 MHz, $CDCl_3$) δ 7.82 – 7.72 (m, 2H), 7.54 – 7.34 (m, 3H), 6.24 (s, 1H), 4.29 (h, *J* = 6.7 Hz, 1H), 1.26 (d, *J* = 6.6 Hz, 6H).; ^{13}C NMR (75 MHz, $CDCl_3$) δ 166.94, 134.87, 131.38,

N-cyclohexylbenzamide (2aa).[2]

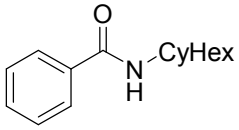

2aa

Following the general procedure using 20% ethyl acetate in hexanes as eluant, **2aa** was obtained as a white solid (34.6 mg, 85% yield); R_f= 0.25 (ethyl acetate:hexanes, 1:5); ^{1}H NMR (300 MHz, $CDCl_3$) δ 7.90 – 7.63 (m, 2H), 7.59 – 7.34 (m, 3H), 5.97 (s, 1H), 4.08 – 3.88 (m, 1H), 2.14 – 1.94 (m, 2H), 1.83 – 1.56 (m, 4H), 1.51 – 1.35 (m, 2H), 1.29 – 1.18 (m, 3H).; ^{13}C
N
M
R

(
7
5

M

N-benzylbenzamide (2ab).[9]

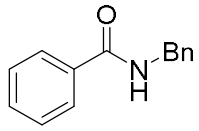

2ab

Following the general procedure using 25% ethyl acetate in hexanes as eluant, **2b** was obtained as a white solid (25.4 mg, 60% yield); R_f= 0.35 (ethyl acetate:hexanes, 1:2); ^{1}H NMR (300 MHz, $CDCl_3$) δ 7.89 – 7.69 (m, 2H), 7.55 – 7.22 (m, 8H), 6.57 (s, 1H), 4.63 (d, *J* = 5.7 Hz, 2H).; ^{13}C NMR (75 MHz, $CDCl_3$) δ 167.50, 138.30, 134.47, 131.67, 128.99, 128.90,

VIII.[1]H and [13]C NMR Spectral

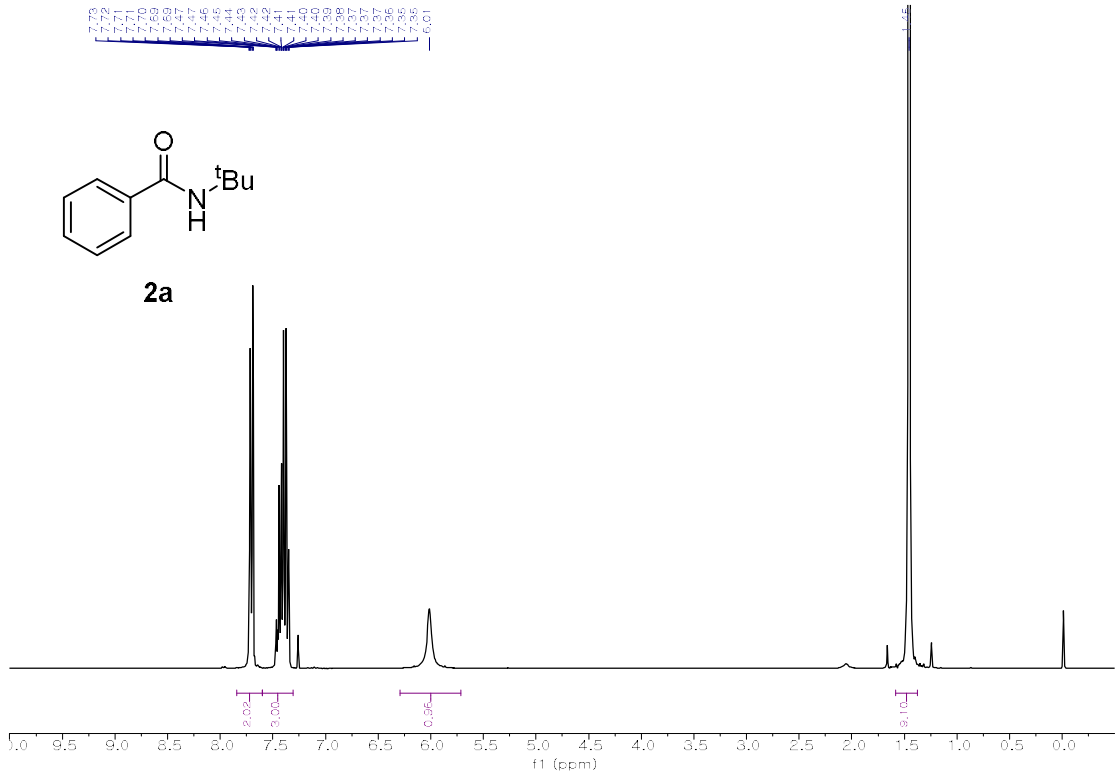

^{1}H-NMR (300 MHz, $CDCl_3$) of **2a**

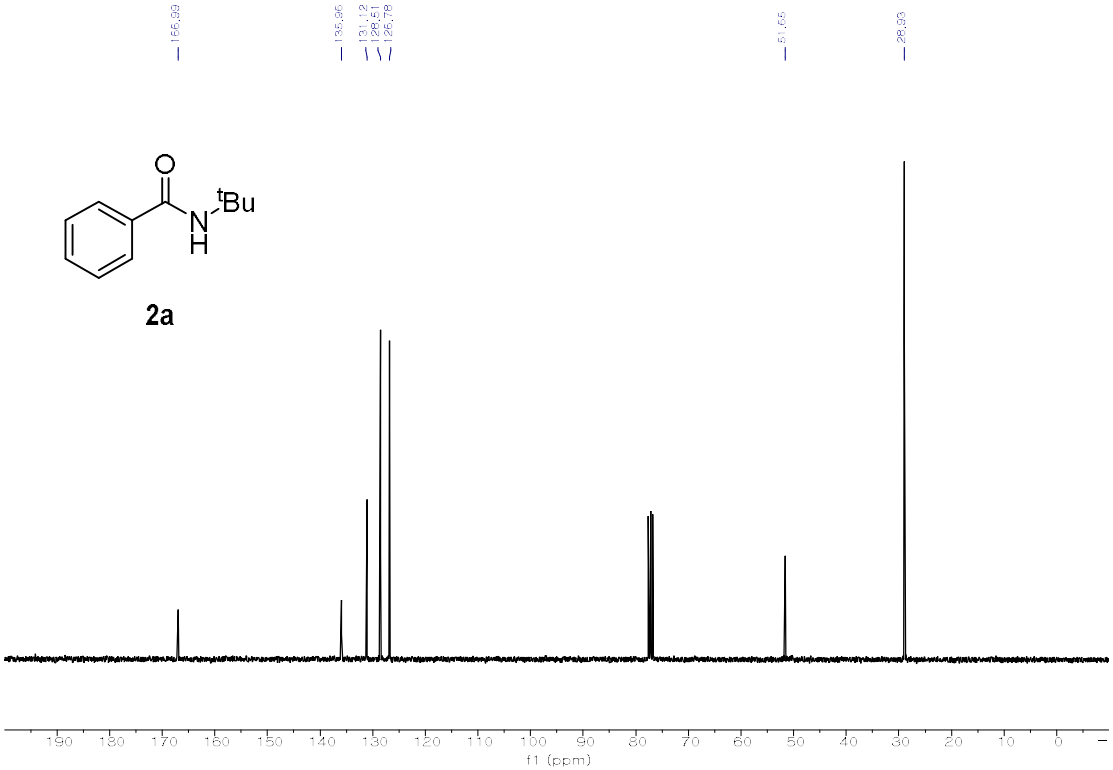

^{13}C-NMR (75Hz, $CDCl_3$) of **2a**

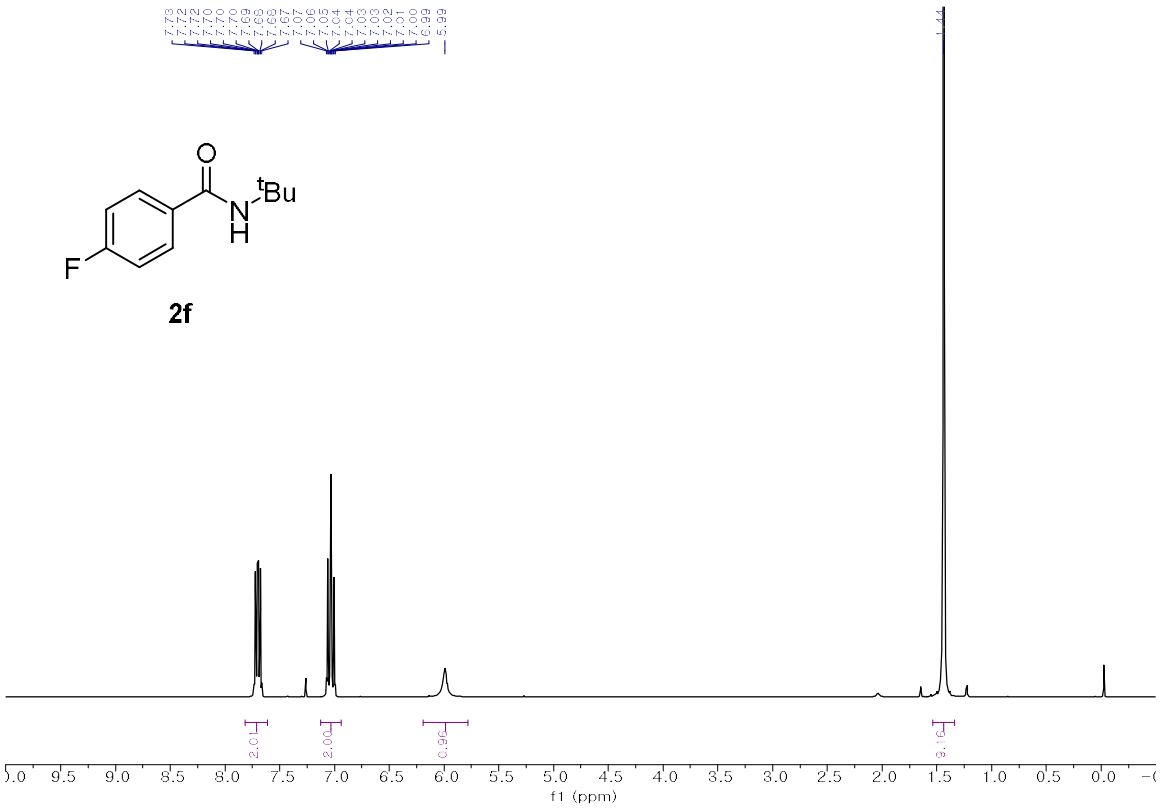

^{1}H-NMR (300 MHz, $CDCl_3$) of **2f**

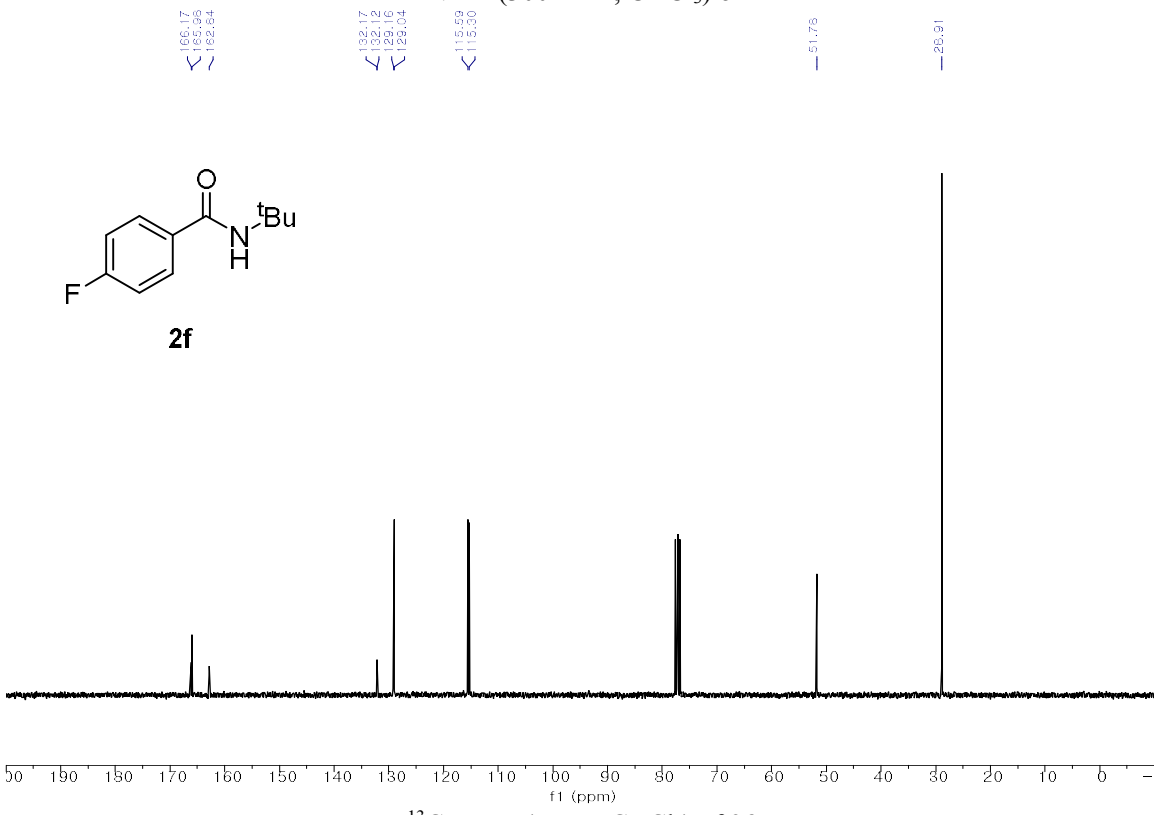

^{13}C-NMR (75Hz, $CDCl_3$) of **2f**

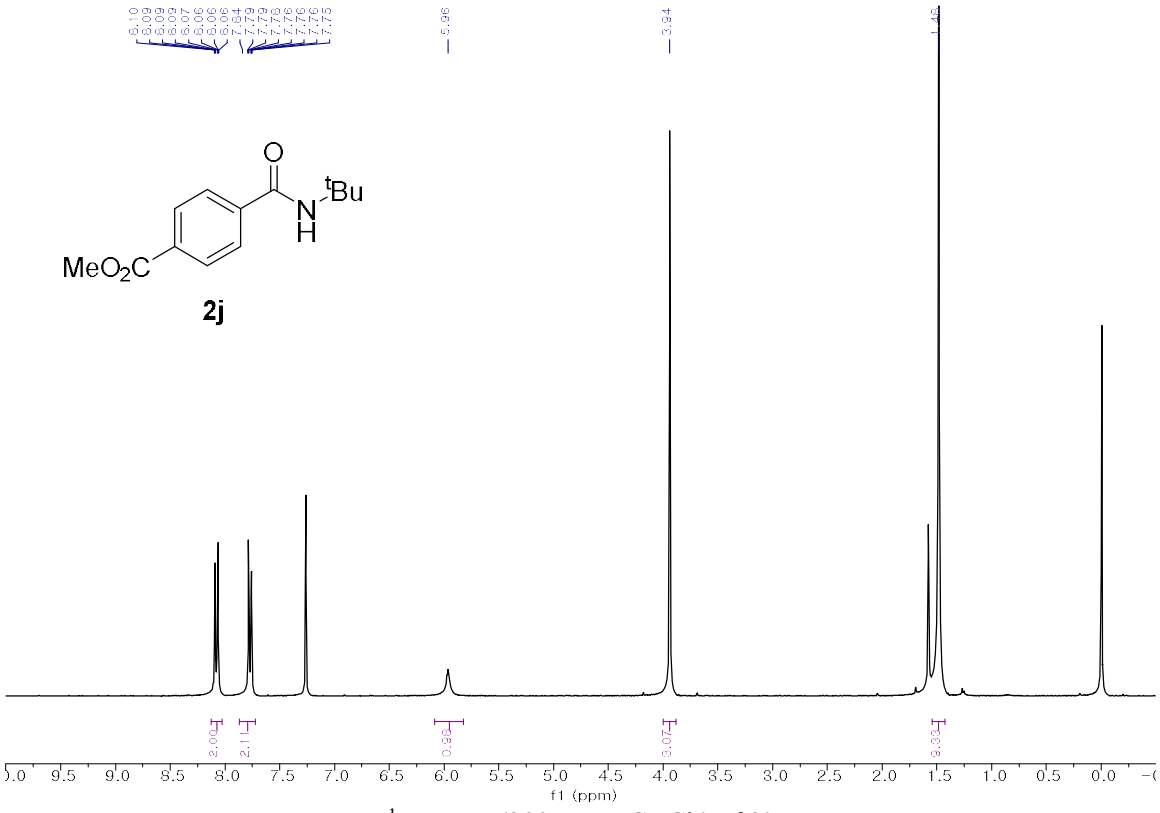

^{1}H-NMR (300 MHz, $CDCl_3$) of **2j**

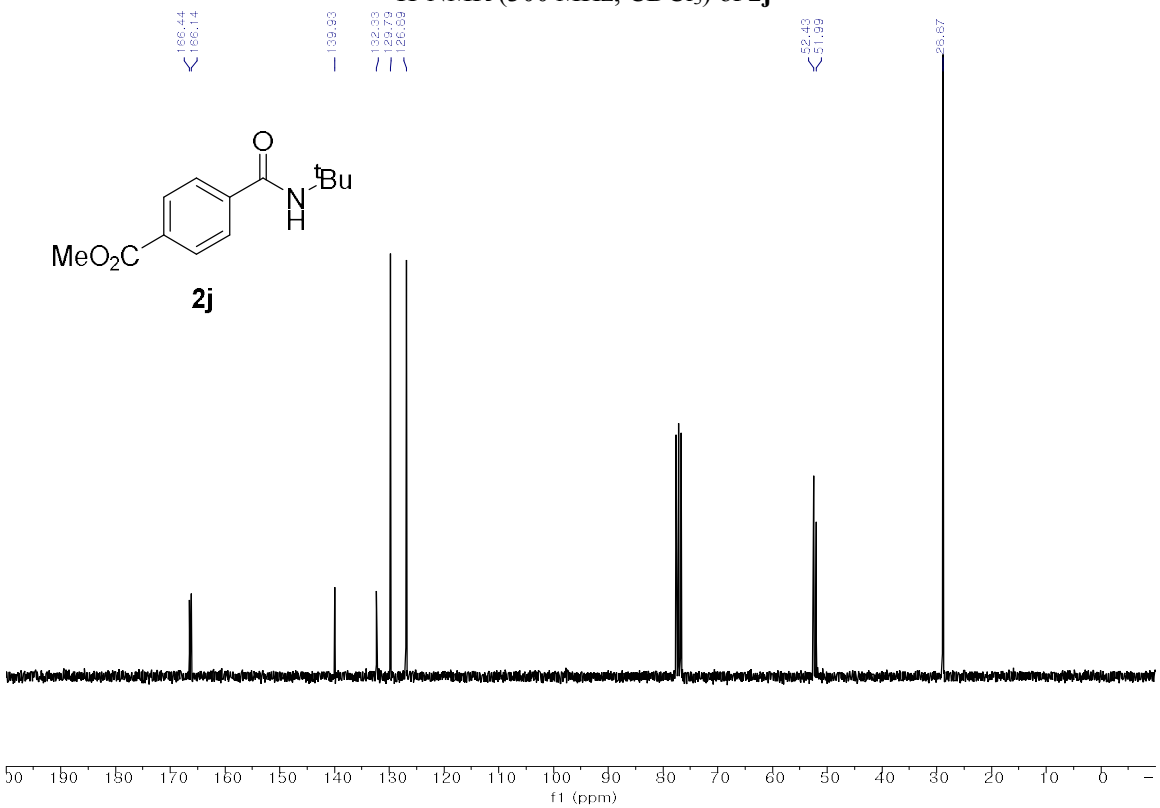

^{13}C-NMR (75Hz, $CDCl_3$) of **2j**

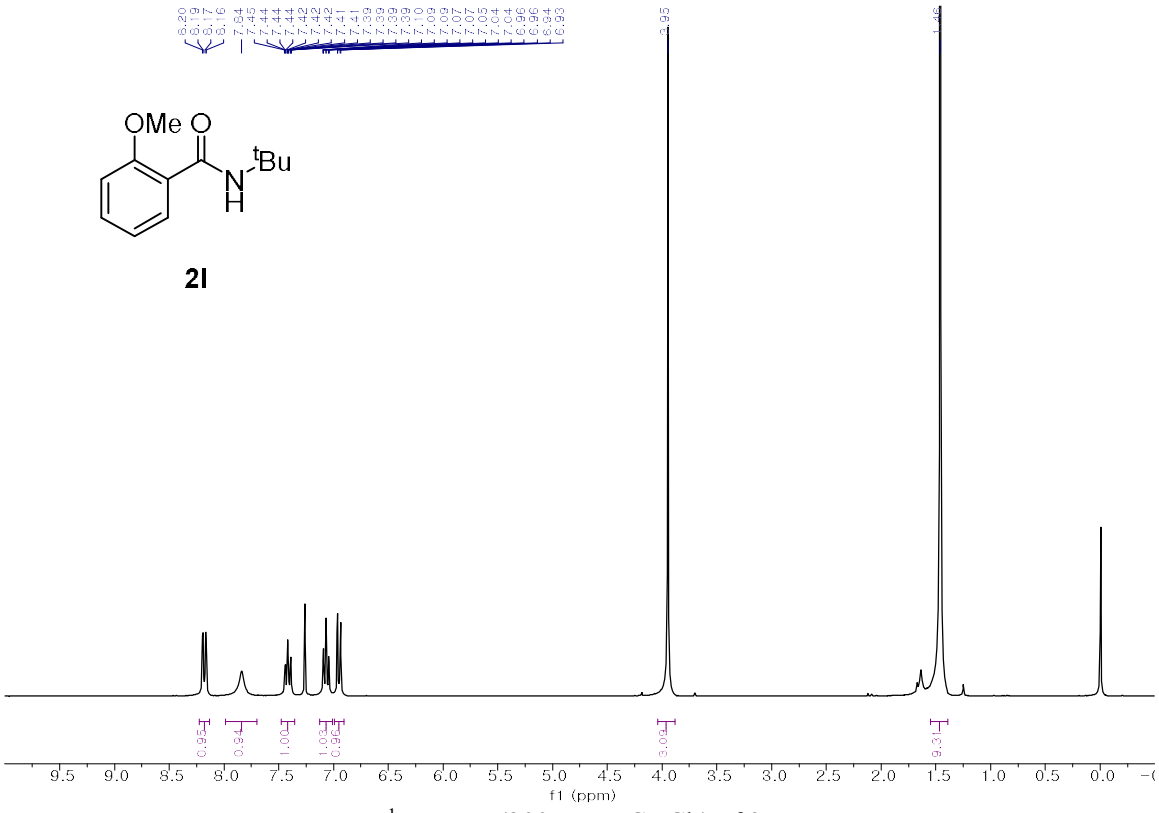

^{1}H-NMR (300 MHz, $CDCl_3$) of **2l**

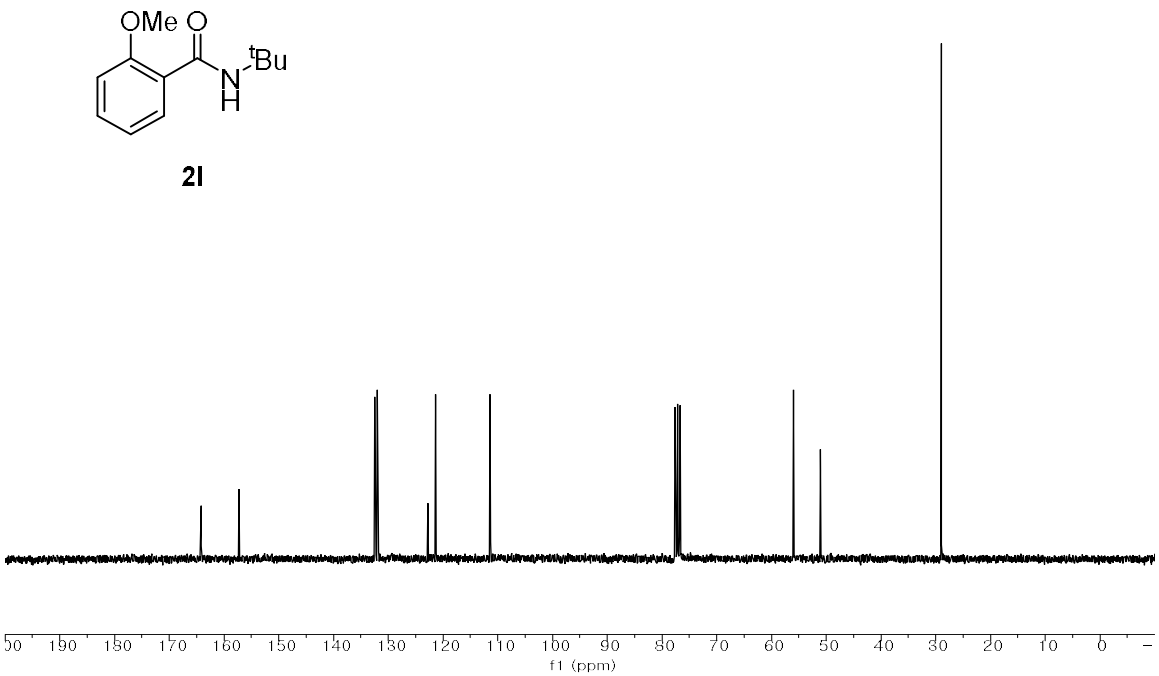

^{13}C-NMR (75Hz, $CDCl_3$) of **2l**

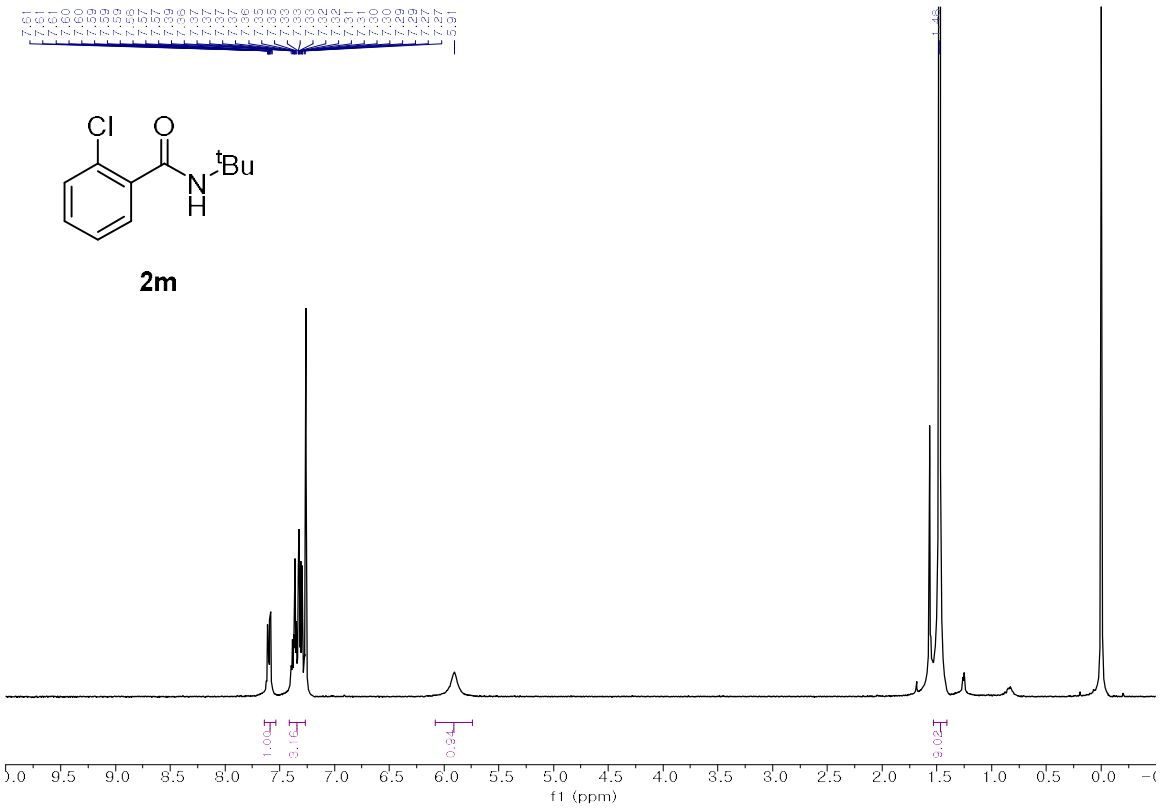

^{1}H-NMR (300 MHz, $CDCl_3$) of **2m**

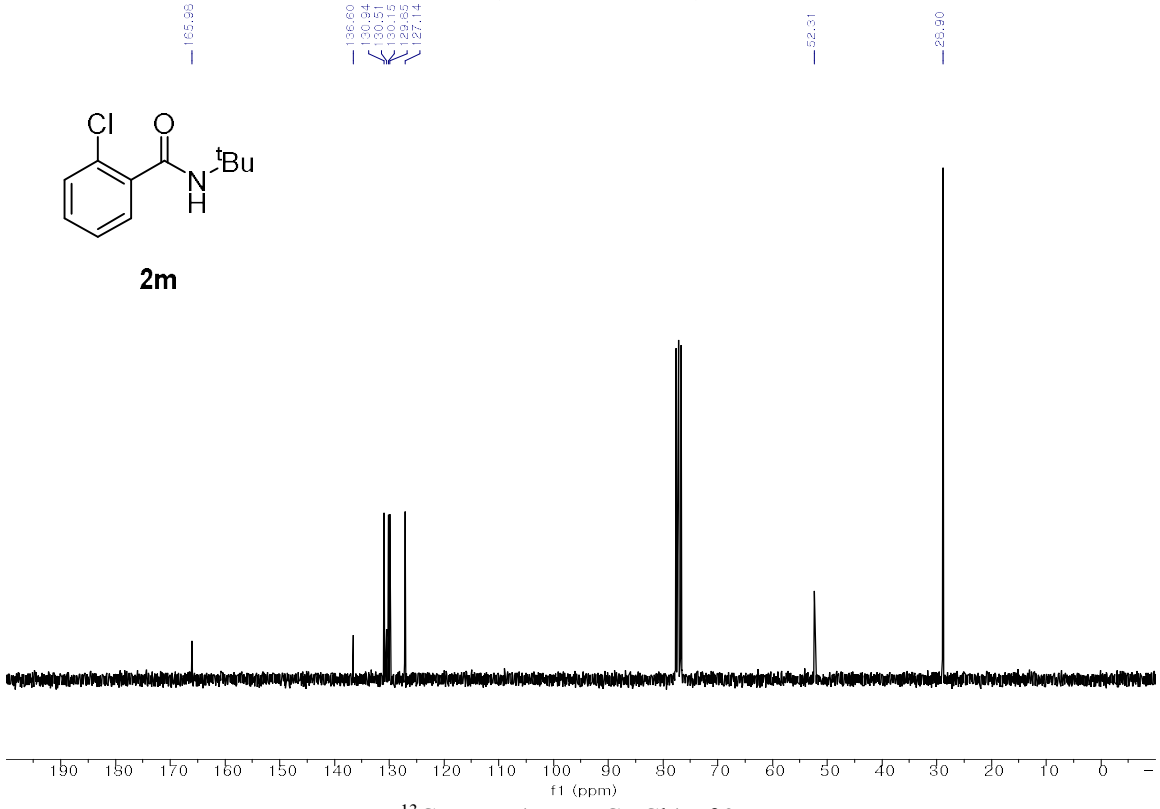

^{13}C-NMR (75Hz, $CDCl_3$) of **2m**

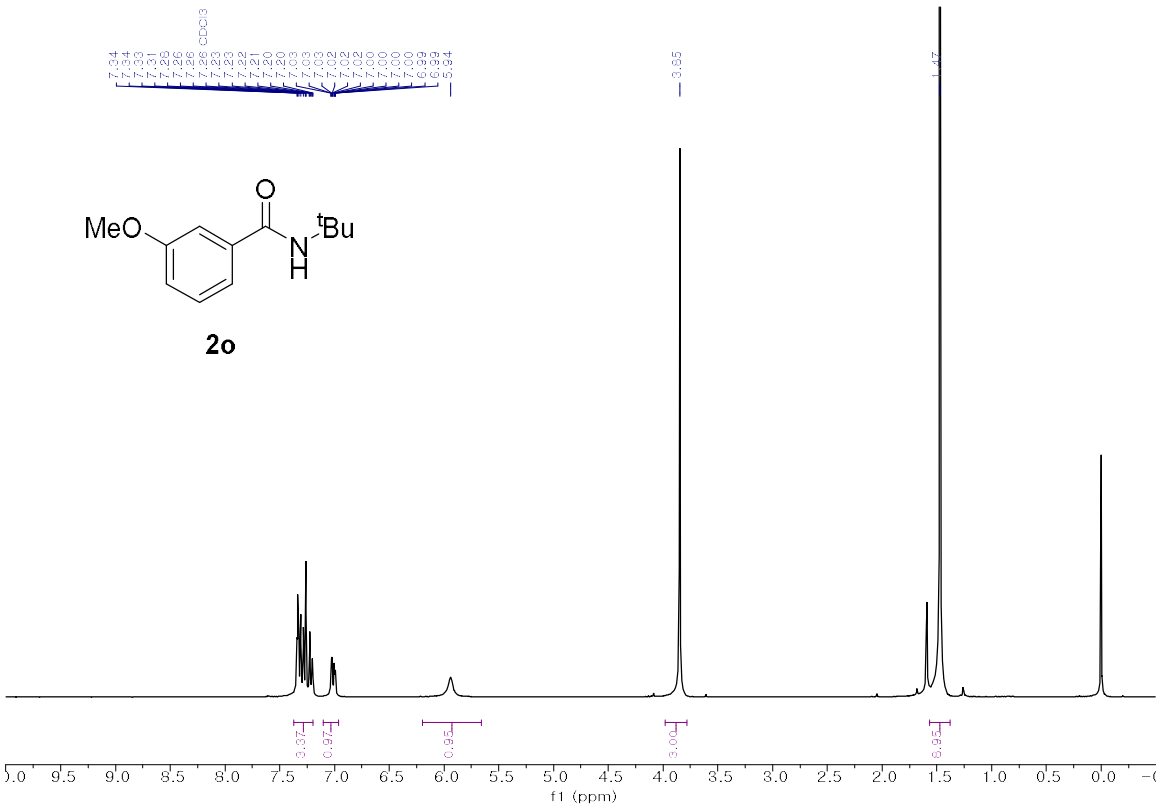

^{1}H-NMR (300 MHz, $CDCl_3$) of **2o**

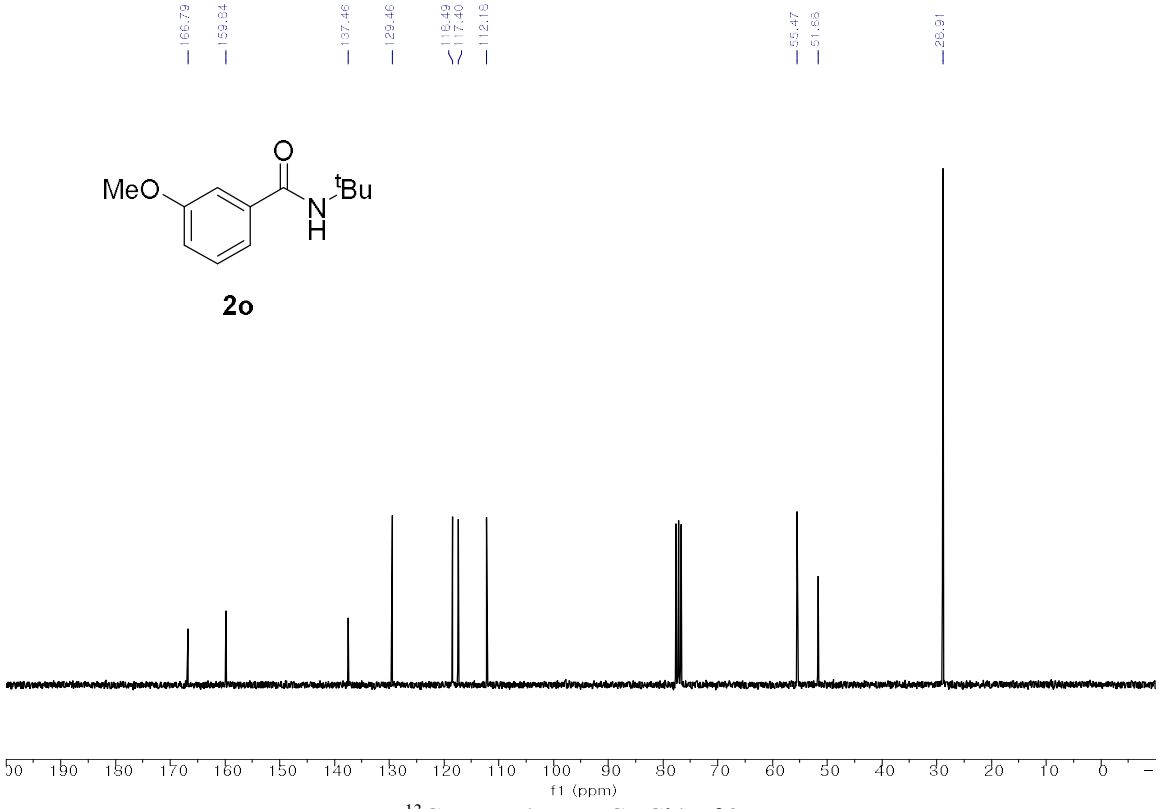

^{13}C-NMR (75Hz, $CDCl_3$) of **2o**

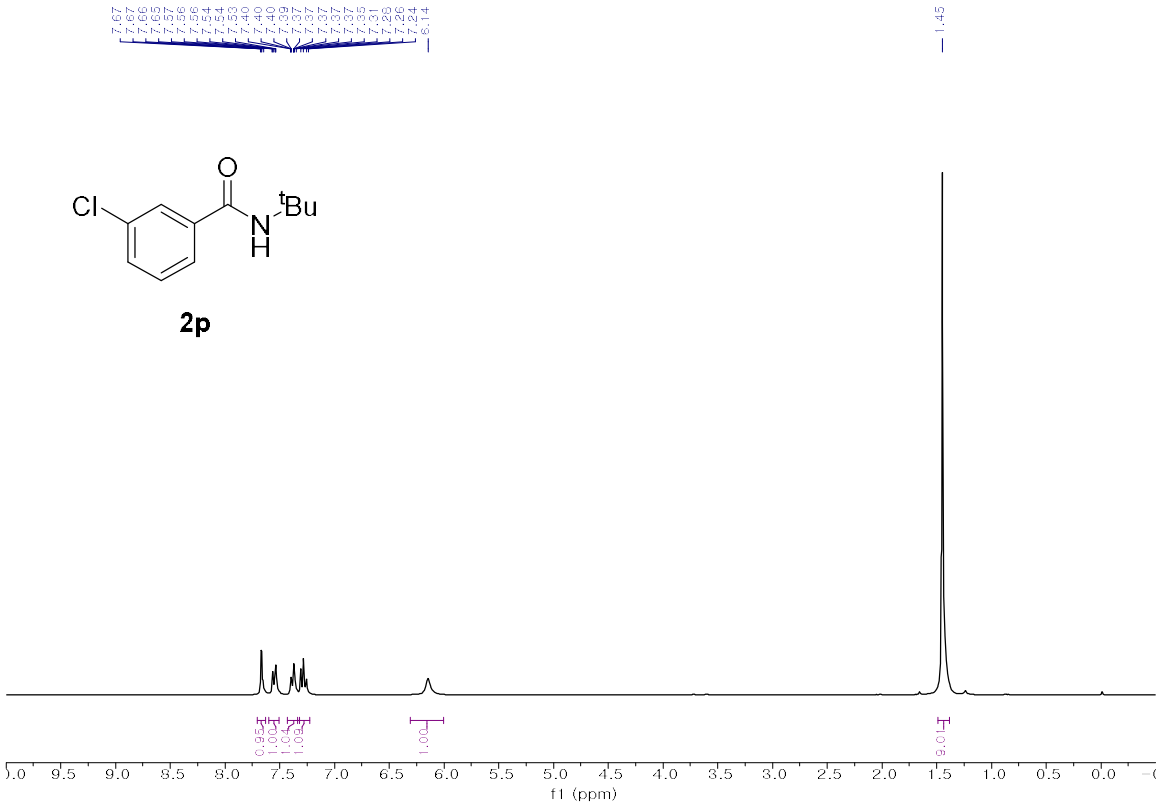

^{1}H-NMR (300 MHz, $CDCl_3$) of **2p**

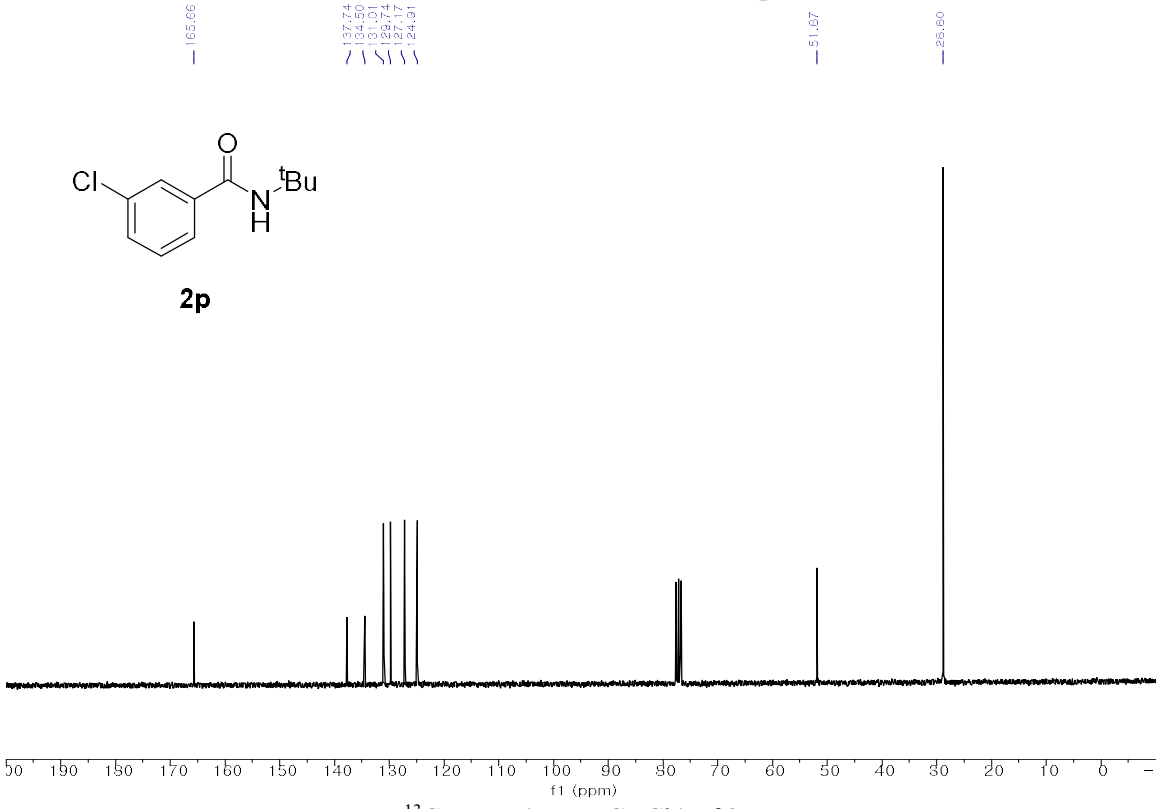

^{13}C-NMR (75Hz, $CDCl_3$) of **2p**

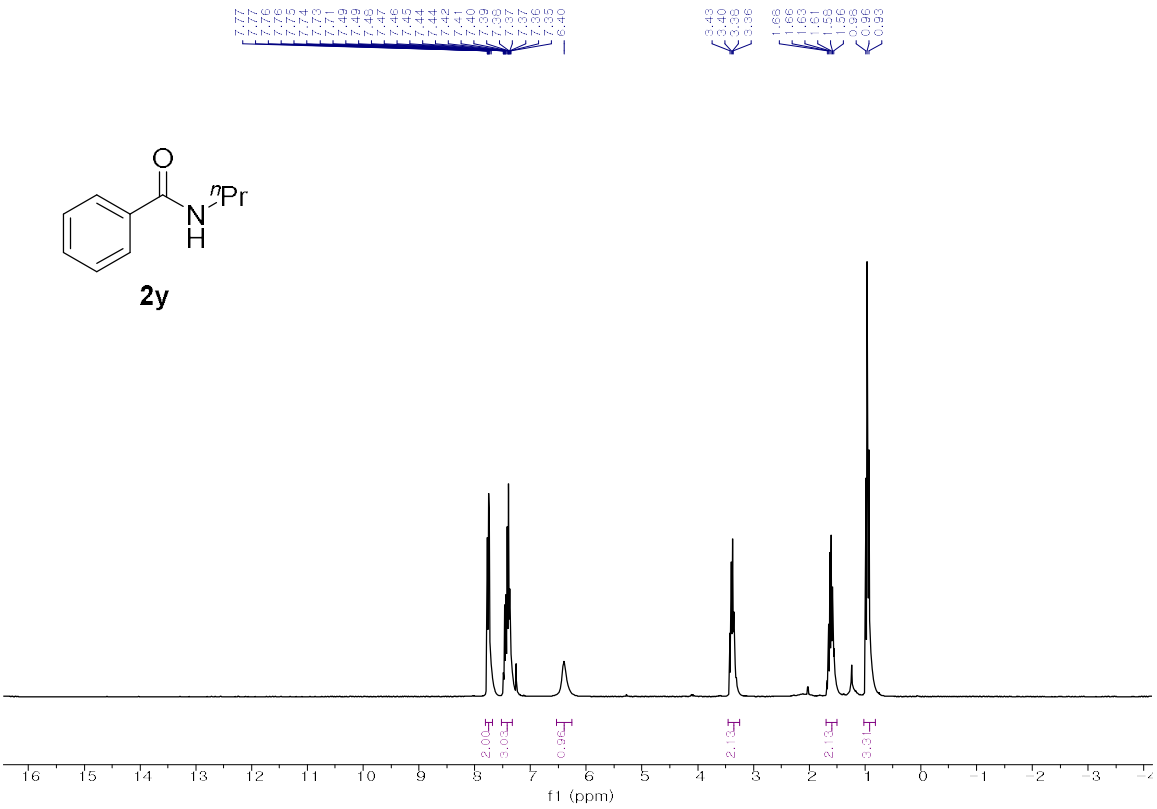

^{1}H-NMR (300 MHz, $CDCl_3$) of **2y**

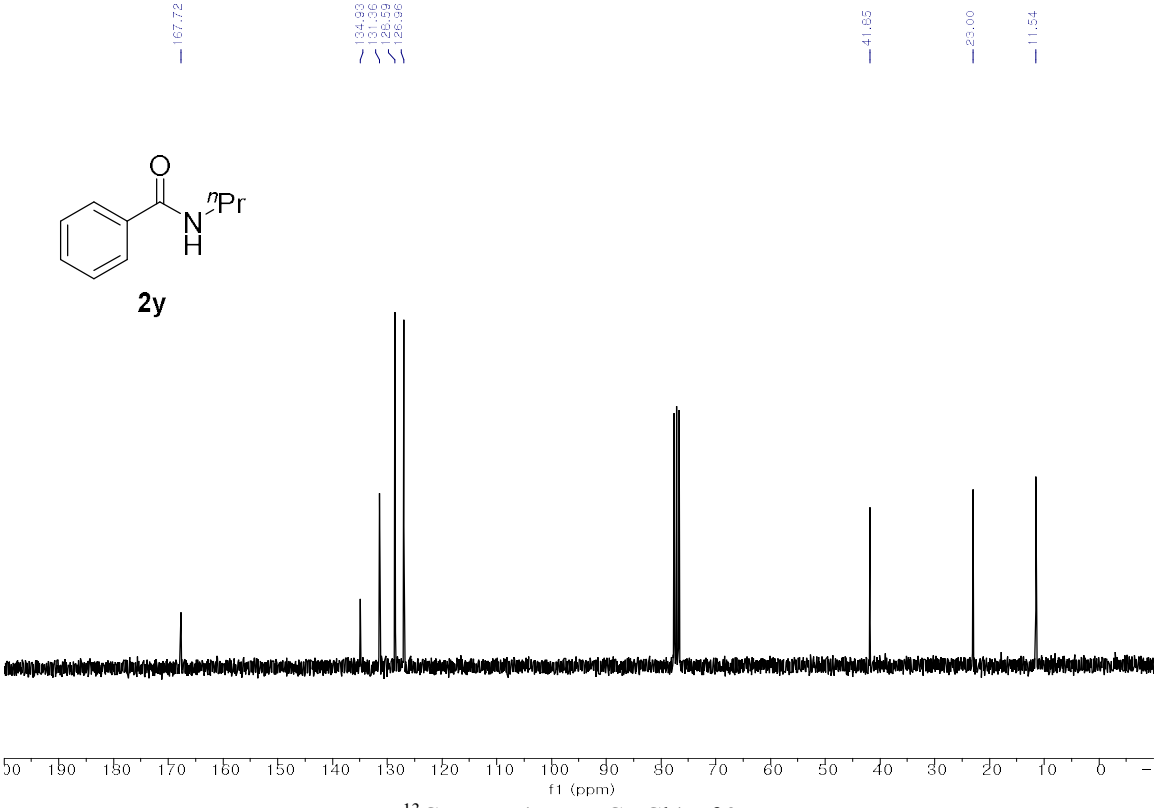

^{13}C-NMR (75Hz, $CDCl_3$) of **2y**

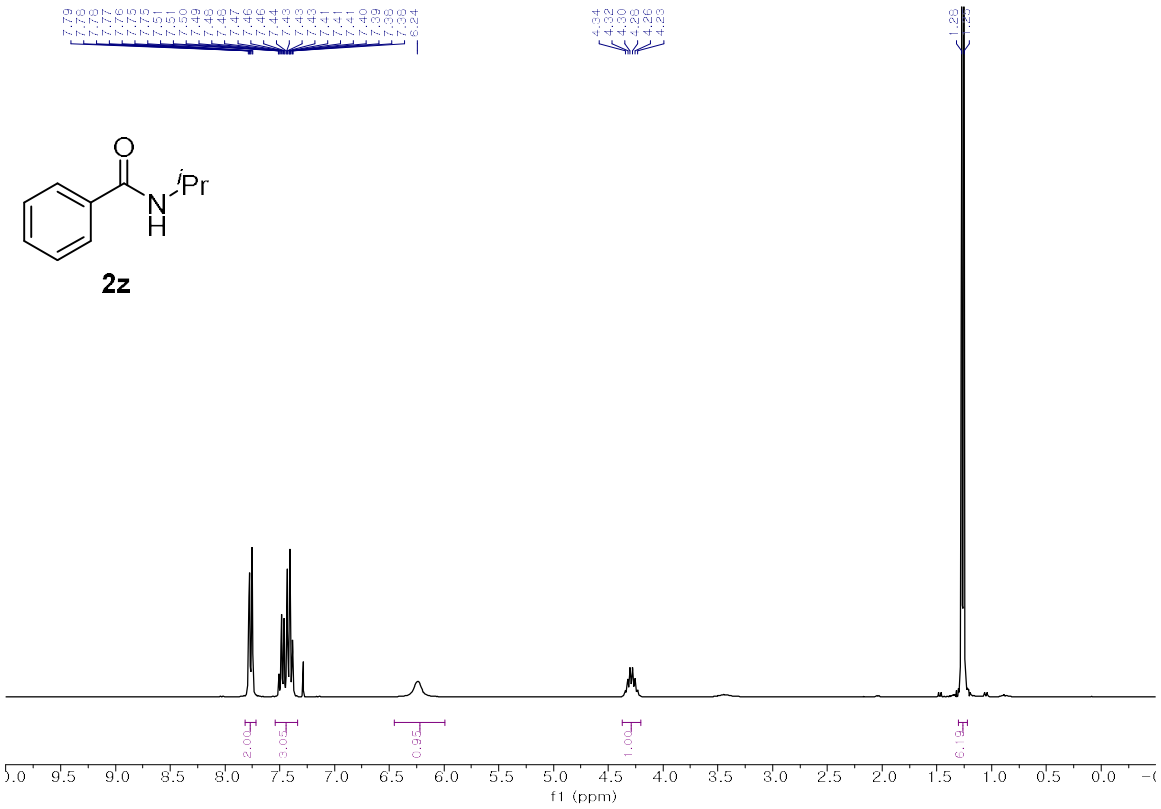

^{1}H-NMR (300 MHz, $CDCl_3$) of **2z**

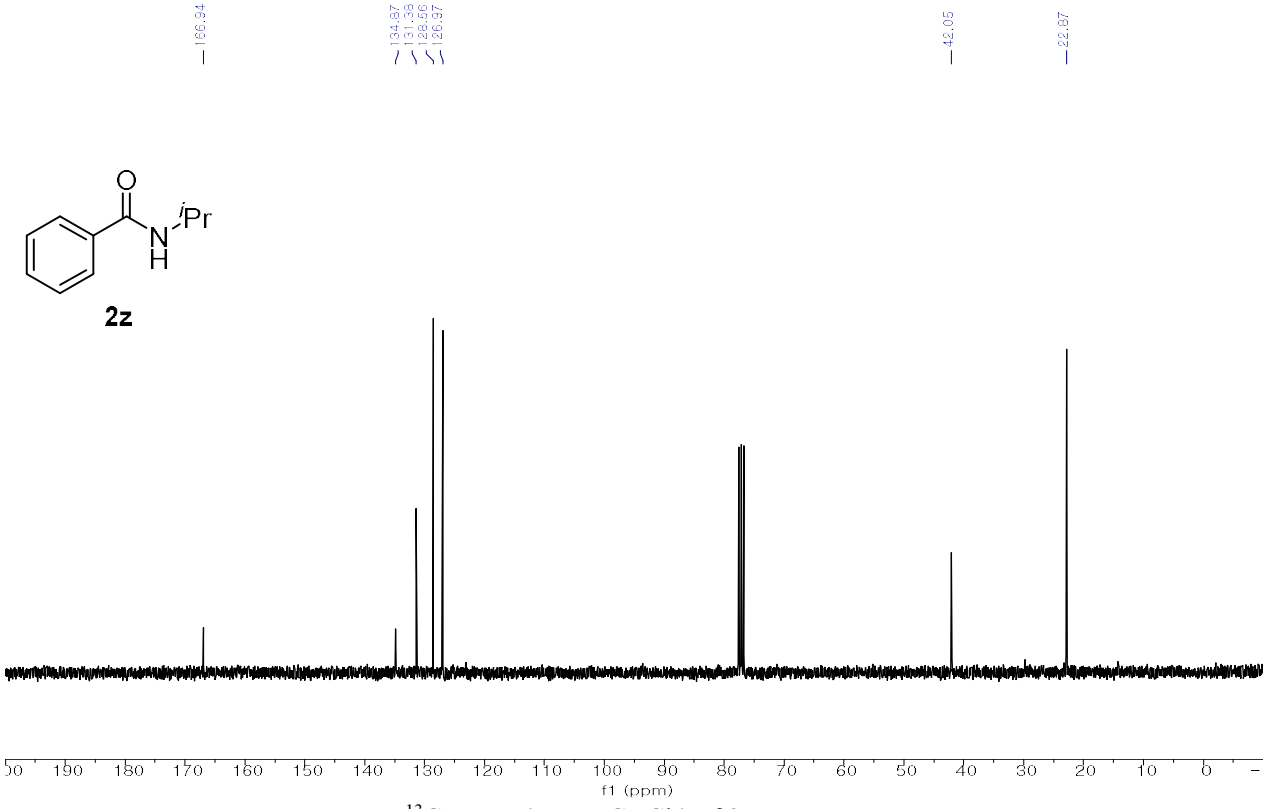

^{13}C-NMR (75Hz, $CDCl_3$) of **2z**

IX. DFT calculation about CO_2 conversion

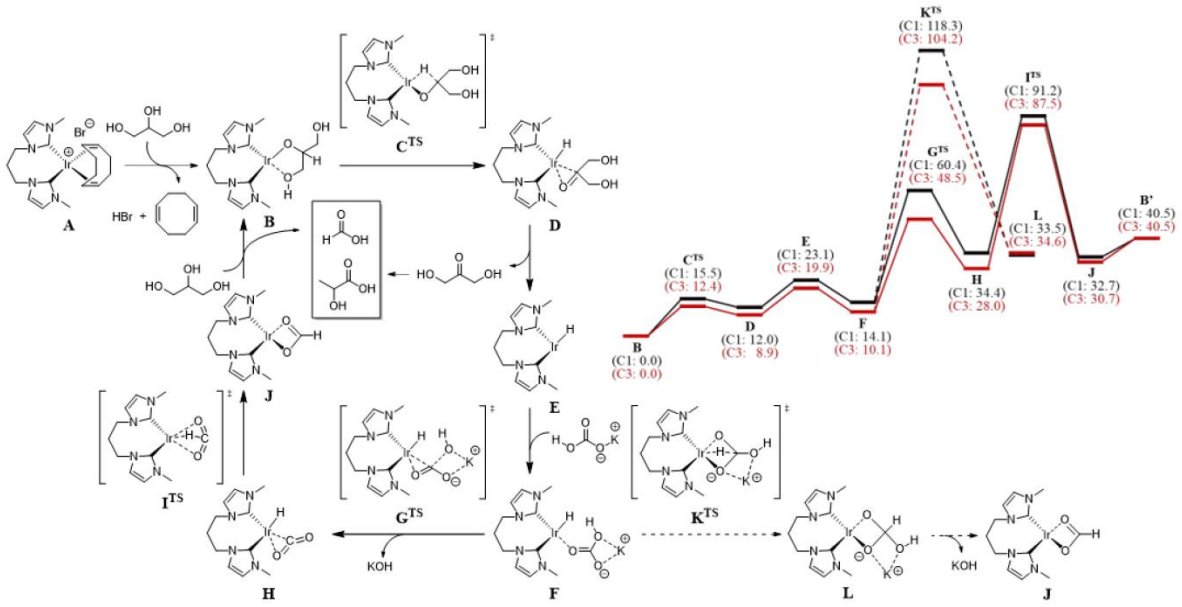

Figure S3. Proposed reaction mechanism for the simultaneous conversion of inorganic carbonate/glycerol to formate/lactate and the corresponding reaction energy diagram for two catalysts, 1 and its tether-modified catalyst, where we modified the length of the alkyl chain tether from n = 3 (1) to n = 1. C3 and C1 denote catalyst 1 and its tether-modified catalyst, respectively. The direct reduction process of bicarbonate bound on the iridium catalyst is indicated as F→K^{TS}→L, which should be followd by dihydroxylation (L→J) to produce formates. Because the reaction barrier for dihydroxylation (L→J) is expected to be lower than that for direct reduction of inorganic carbonate by hydride transfer (F→K^{TS}→L) as observed in F→G^{TS}→H→I^{TS}→J, the transition state between L and J was not elucidated. A reaction energy diagram was constructed using PBE0-D3/6-311++G(d,p)//PBE0-D3/6-31G(d,p) calculations (see Figure S4 for the reaction energy diagram constructed using MN15/6-311++G(d,p)//MN15/6-31G(d,p) calculations). All the energy values are related to the Gibbs free energy (ΔG in kcal/mol) at 298.15 K and 1 atm.

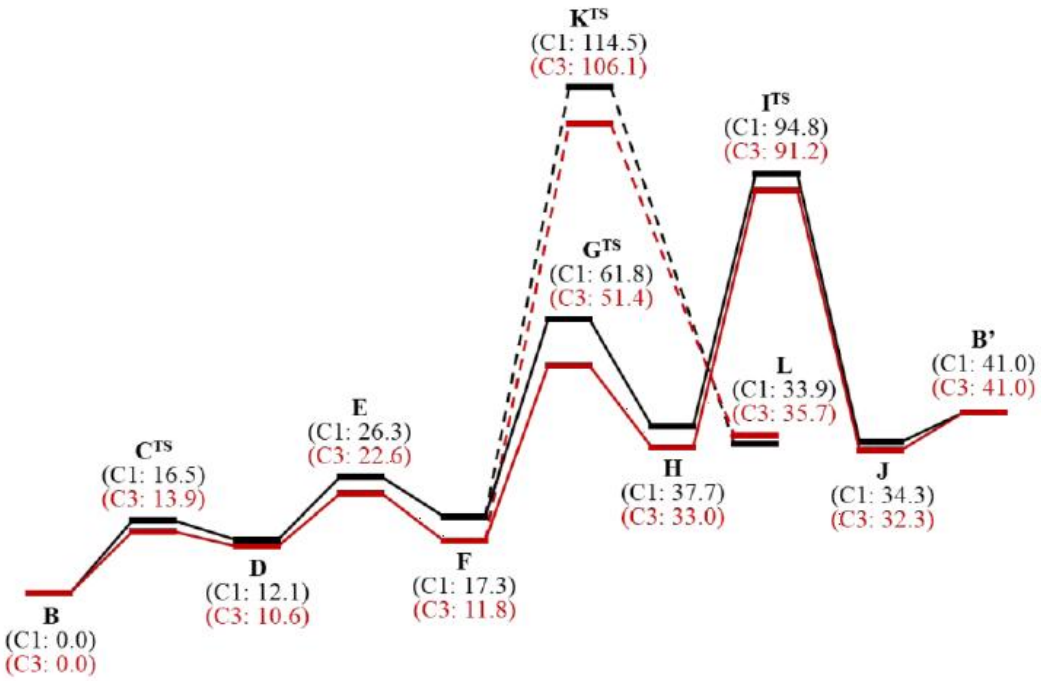

Figure S4. Reaction energy diagram for two catalysts, 1 and its tether-modified catalyst, where we modified the length of alkyl chain tether from n = 3 (1) to n = 1. The C3 and C1 denote catalyst 1 and its tether-modified catalyst. The reaction energy diagram was constructed using MN15/6 -311++G(d,p)//MN15/6-31G(d,p) calculations. All energy values are corrected with Gibbs free energy (ΔG in kcal/mol) at 298.15 K and 1 atm.

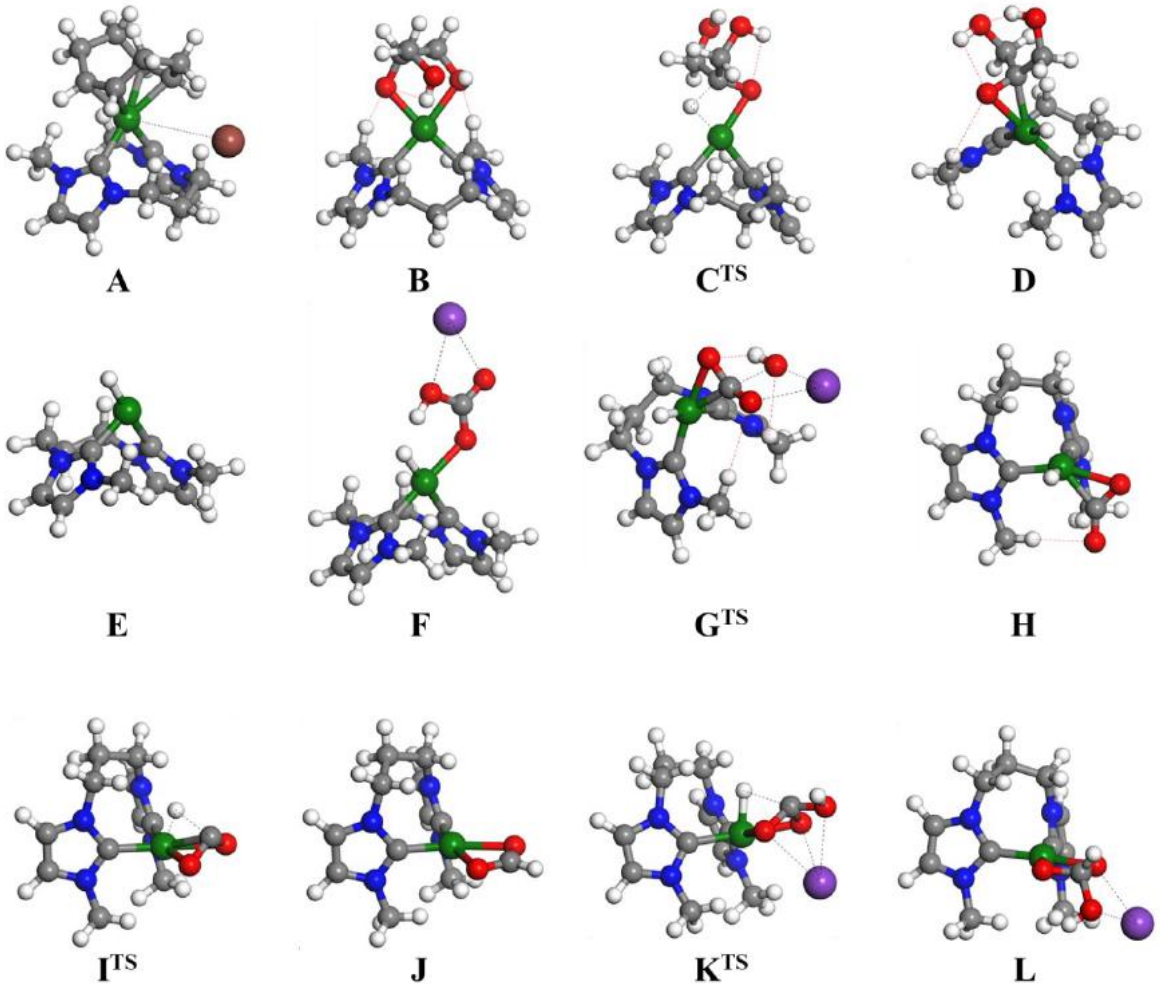

Figure S5. Optimized geometries of C3 (1) catalyst using PBE0-D3/6-31G(d,p) calculations along the proposed reaction mechanism for simultaneous conversion of inorganic carbonate/glycerol to formate/lactate (see Figure 3). The O-H…O and C-H…O hydrogen bonds are indicated with red-colored dashed lines. [Ir, green; Br, brown; K, purple; O, red; N, blue; C, gray; H, white]

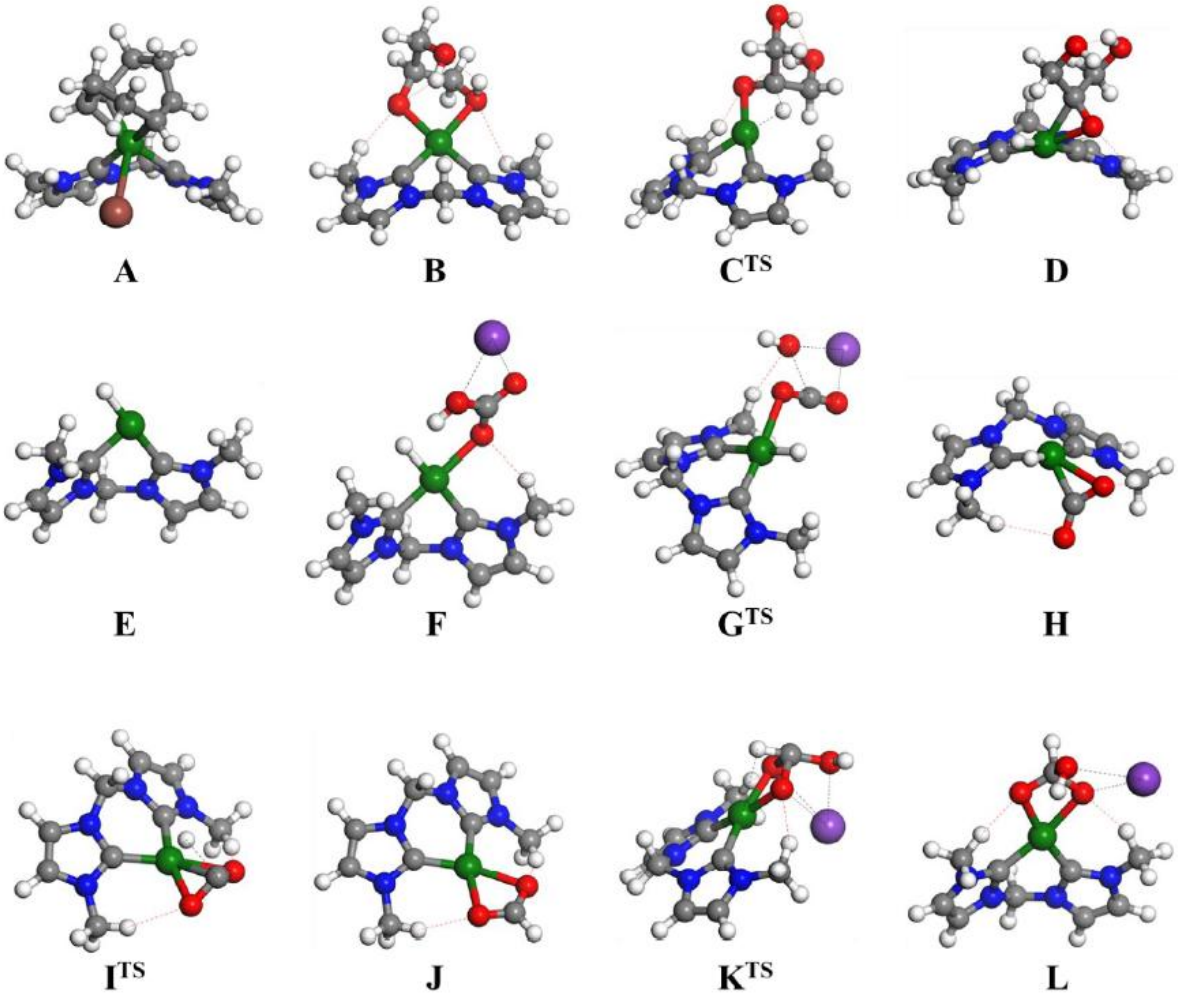

Figure S6. Optimized geometries of C1 catalyst using PBE0-D3/6-31G(d,p) calculations along the proposed reaction mechanism for simultaneous conversion of inorganic carbonate/glycerol to formate/lactate (see Figure 3). The O-H…O and C-H…O hydrogen bonds are indicated with red-colored dashed lines. [Ir, green; Br, brown; K, purple; O, red; N, blue; C, gray; H, white]

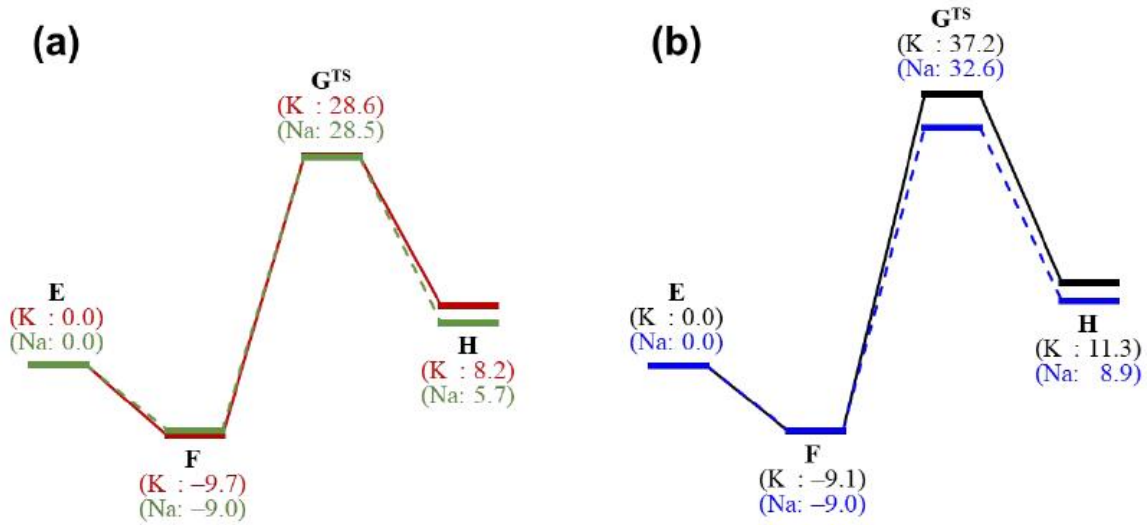

Figure S7. Reaction energy diagrams for E→F→G^{TS}→H depending on the kind of inorganic bicarbonate, (a) C3 catalyst (red solid line: $KHCO_3$, green dashed line: $NaHCO_3$) and (b) C1 catalyst (black solid line: $KHCO_3$, blue dashed line: $NaHCO_3$). All reaction energy diagrams were constructed using PBE0-D3/6 311++G(d,p)//PBE0-D3/6-31G(d,p) calculations, in which the relative energy values (ΔG in kcal/mol at 298.15 K and 1 atm) are obtained with respect to the energy of step E.

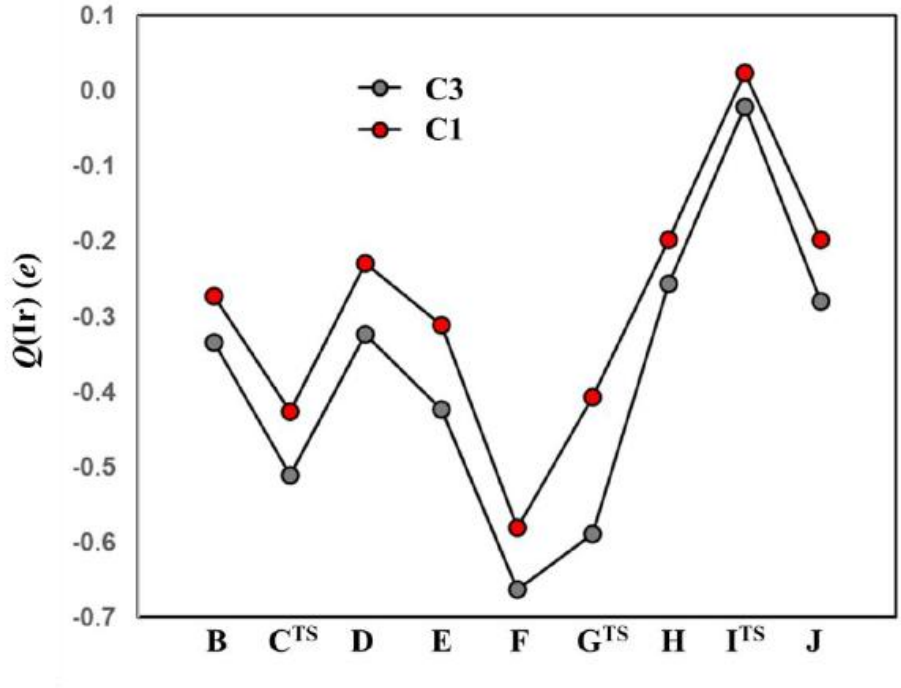

Figure S8. Atomic charge of central Ir atom during catalytic reaction. Natural population analysis was performed using electron density obtained from PBE0-D3/6-311++G(d,p)//PBE0-D3/6-31G(d,p) calculations. The LanL2DZ and SDD were employed as an effective pseudo-potential for iridium for geometry optimization and single point calculation, respectively.

7. Publications & Permission

1. Yeon-Joo Cheong, Kihyuk Sung, **Sehoon Park**, Jaehoon Jung,* and Hye-Young Jang*, Valorization of Chemical Wastes: Ir(biscarbene)-Catalyzed Transfer Hydrogenation of Inorganic Carbonates Using Glycerol. ACS Sustainable Chem. Eng. 2020, 8, 6972−6978
2. Jin Park,‡ **Sehoon Park,‡** Gwang Seok Jang, Ran Hui Kim, Jaehoon Jung * and Sang Kook Woo *, Weak base-promoted selective rearrangement of oxaziridines to amides via visible-light photoredox catalysis†. Chem. Commun., 2021,57, 9995-9998

This thesis adapted with permission from ACS Sustainable Chemistry & Engineering. Copyright 2020 American Chemical Society.

This thesis adapted with permission from RSC Chemical Communications Journal. Copyright 2021 Royal Society of Chemistry

8. Reference

1. (a) J. Aube´, Chem. Soc. Rev., 1997, 26, 269; (b) K. S. Williamson, D. J. Michaelis and T. P. Yoon, Chem. Rev., 2014, 114, 8016; (c) F. A. Davis, Tetrahedron, 2018, 74, 3198; (d) S. K. Woo, Oxaziridines and Oxazirines, 2020, DOI: 10.1016/B978-0-12-409547-2.14812-7.

2. (a) A. K. Ghose, V. N. Viswanadhan and J. J. Wendoloski, J. Comb. Chem., 1999, 1, 55; (b) J. S. Carey, D. Laffan, C. Thomson and M. T. Williams, Org. Biomol. Chem., 2006, 4, 2337; (c) R. M. de Figueiredo, J.-S. Suppo and J.-M. Campagne, Chem. Rev., 2016, 116, 12029.

3. (a) D. Leow, Org. Lett., 2014, 16, 5812; (b) Y. Kurose, Y. Imada, Y. Okada and K. Chiba, Eur. J. Org. Chem., 2020, 3844.

4. (a) A. J. Post and H. Morrison, J. Am. Chem. Soc., 1995, 117, 7812; (b) M. S. Wolfe, D. Dutta and J. Aube´, J. Org. Chem., 1997, 62, 654; (c) S. Wenglowsky and L. S. Hegedus, J. Am. Chem. Soc., 1998, 120, 12468; (d) Y. Zhang, M. L. Blackman, A. B. Leduc and T. F. Jamison, Angew. Chem., Int. Ed., 2013, 52, 4251.

5. F. A. Davis, N. V. Gaddiraju, N. Theddu, J. R. Hummel, S. K. Kondaveeti and M. J. Zdilla, J. Org. Chem., 2012, 77, 2345.

6. (a) G. M. Rubottom, Tetrahedron Lett., 1969, 10, 3887; (b) M. Newcomb and R. A. Reeder, J. Org. Chem., 1980, 45, 1489; (c) G.-I. An and H. Rhee, Synlett, 2003, 0876; (d) D. Xing, X. Xu and L. Yang, Synthesis, 2009, 3399.

7. D. S. C. Black and L. M. Johnstone, Angew. Chem., Int. Ed. Engl., 1981, 20, 669.

8. (a) C. H. Leung, A. M. Voutchkova, R. H. Crabtree, D. Balcells and O. Eisenstein, Green Chem., 2007, 9, 976; (b) J. Kraiem and T. Ollevier, Green Chem., 2017, 19, 1263.

9. (a) Y. Iwano, Y. Kawamura, H. Miyoshi, T. Yoshinari and T. Horie, Bull. Chem. Soc. Jpn., 1994, 67, 2348; (b) I. Yasunori, K. Yasuhiko and H. Tokunaru, Chem. Lett., 1995, 67.

10. E. Oliveros, M. Riviere, J. P. Malrieu and C. Teichteil, J. Am. Chem. Soc., 1979, 101, 318.

11. (a) C. K. Prier, D. A. Rankic and D. W. C. MacMillan, Chem. Rev., 2013, 113, 5322; (b) M. H. Shaw, J. Twilton and D. W. C. MacMillan, J. Org. Chem., 2016, 81, 6898; (c) I.

K. Sideri, E. Voutyritsa and C. G. Kokotos, Org. Biomol. Chem., 2018, 16, 4596; (d) N. F. Nikitas, P. L. Gkizis and C. G. Kokotos, Org. Biomol. Chem., 2021, 19, 5237.
12. G. S. Jang, J. Lee, J. Seo and S. K. Woo, Org. Lett., 2017, 19, 6448.

13. Barnard, C. F. J. Palladium-catalyzed carbonylation-a reaction come of age. Organometallics 2008, 27, 5402−5422.
14. Brennführer, A.; Neumann, H.; Beller, M. Palladium-catalyzed carbonylation reactions of aryl halides and related compounds. Angew. Chem., Int. Ed. 2009, 48, 4114−4133.
15. Gadge, S. T.; Bhanage, B. M. Recent developments in palladium catalysed carbonylation reactions. RSC Adv. 2014, 4, 10367−10389.
16. Zevenhoven, R.; Eloneva, S.; Teir, S. Chemical fixation of CO2 in carbonates: Routes to valuable products and long-term storage. Catal. Today 2006, 115, 73−79.
17. Sakakura, T.; Choi, J.-C.; Yasuda, H. Transformation of carbon dioxide. Chem. Rev. 2007, 107, 2365−2387.
18. Mikkelsen, M.; Jørgensen, M.; Krebs, F. C. The tetraton challenge. A review of fixation and transformation of carbon dioxide. Energy Environ. Sci. 2010, 3, 43−81.
19. Pagliaro, M.; Ciriminna, R.; Kimura, H.; Rossi, M.; Della Pina, C. From glycerol to value-added products. Angew. Chem., Int. Ed. 2007, 46, 4434−4440.
20. Zhou, C.-H.; Beltramini, J. N.; Fan, Y.-X.; Lu, G. Q. Chemoselective catalytic conversion of glycerol as a biorenewable source to valuable commodity chemicals. Chem. Soc. Rev. 2008, 37, 527−549.
21. Behr, A.; Eilting, J.; Irawadi, K.; Leschinski, J.; Lindner, F. Improved utilisation of renewable resources: New important derivatives of glycerol. Green Chem. 2008, 10, 13−30.
22. García, J. I.; García-Marín, H.; Pires, E. Glycerol based solvents: synthesis, properties and applications. Green Chem. 2014, 16, 1007−1033.
23. Based on U.S. monthly biodiesel production report 2016− 2018, the US biodiesel industry produces 2.4 billion gallons of biodiesel each year: http://www.eia.gov/biofuels/biodiesel/ production/ (accessed March 2018).
24. Sharninghausen, L. S.; Campos, J.; Manas, M. G.; Crabtree, R. H. Efficient selective and atom economic catalytic conversion of glycerol to lactic acid. Nat. Commun. 2014, 5, 5084−5092. ACS Sustainable Chemistry & Engineering pubs.acs.org/journal/ascecg

Research Article https://dx.doi.org/10.1021/acssuschemeng.0c00050 ACS Sustainable Chem. Eng. 2020, 8, 6972−6978 6977

25. Sharninghausen, L. S.; Mercado, B. Q.; Crabtree, R. H.; Hazari, N. Selective conversion of glycerol to lactic acid with iron pincer precatalysts. Chem. Commun. 2015, 51, 16201−16204.

26. Sun, Z.; Liu, Y.; Chen, J.; Huang, C.; Tu, T. Robust iridium coordination polymers: Highly selective, efficient, and recyclable catalysts for oxidative conversion of glycerol to potassium lactate with dihydrogen liberation. ACS Catal. 2015, 5, 6573−6578.

27. Lu, Z.; Demianets, I.; Hamze, R.; Terrile, N. J.; Williams, T. J. A prolific catalyst for selective conversion of neat glycerol to lactic acid. ACS Catal. 2016, 6, 2014−2017.

28. Finn, M.; Ridenour, J. A.; Heltzel, J.; Cahill, C.; Voutchkova-Kostal, A. Next-generation water-soluble homogeneous catalysts for conversion of glycerol to lactic acid. Organometallics 2018, 37, 1400− 1409.

29. Díaz-Álvarez, A. E.; Cadierno, V. Glycerol: A promising green solvent and reducing agent for metal-catalyzed transfer hydrogenation reactions and nanoparticles formation. Appl. Sci. 2013, 3, 55−69.

30. Brieger, G.; Nestrick, T. J. Catalytic transfer hydrogenation. Chem. Rev. 1974, 74, 567−580.

31. Zassinovich, G.; Mestroni, G.; Gladiali, S. Asymmetric hydrogen transfer reactions promoted by homogeneous transition metal catalyst. Chem. Rev. 1992, 92, 1051−1069.

32. Wang, D.; Astruc, D. The golden age of transfer hydrogenation. Chem. Rev. 2015, 115, 6621−6686.

33. Sordakis, K.; Tang, C.; Vogt, L. K.; Junge, H.; Dyson, P. J.; Beller, M.; Laurenczy, G. Homogeneous catalysis for sustainable hydrogen storage in formic acid and alcohols. Chem. Rev. 2018, 118, 372−433.

34. Bulushev, D. A.; Ross, J. R. H. Towards sustainable production of formic acid. ChemSusChem 2018, 11, 821−836.

35. Iglesias, M.; Oro, L. A. A leap forward in iridium-NHC catalysis: new horizons and mechanistic insights. Chem. Soc. Rev. 2018, 47, 2772−2808.

36. Lu, Z.; Cherepakhin, V.; Demianets, I.; Lauridsen, P. J.; Williams, T. J. Iridium-based hydride transfer catalysts: from hydrogen storage to fine chemicals. Chem. Commun. 2018, 54, 7711−7724.
37. Crabtree, R. H. Transfer hydrogenation with glycerol as Hdonor: catalyst activation, deactivation and homogeneity. ACS Sustainable Chem. Eng. 2019, 7, 15845−15853.
38. Heltzel, J. M.; Finn, M.; Ainembabazi, D.; Wang, K.; Voutchkova-Kostal, A. M. Transfer hydrogenation of carbon dioxide and bicarbonate from glycerol under aqueous conditions. Chem. Commun. 2018, 54, 6184−6187.
39. Kumar, A.; Semwal, S.; Choudhury, J. Catalytic conversion of CO2 to formate with renewable hydrogen donors: an ambientpressure and H2-independent strategy. ACS Catal. 2019, 9, 2164−2168.
40. Nathan A. Romero and David A. Nicewicz. Chem. Rev. 2016, 116, 10075−10166
41. Kazimer L. Skubi, Travis R. Blum, and Tehshik P. Yoon. Chem. Rev. 2016, 116, 17, 10035–10074
42. Tian-Yi Shang, Ling-Hui Lu, Zhong Cao, Yan Liu, Wei-Min He and Bing Yu. Chem. Commun., 2019,55, 5408-5419
43. Rehm,D.;Weller, A. Isr. J. Chem. 1970, 8 (2), 259-271.
44. Martin, R. M. Electronic Structure: Basic Theory and Practical Methods. (Cambridge University Press, 2004).
45. Jensen, F. Introduction to computational chemistry. (Wiley, 1999).
46. Szabo, A. & Ostlund, N. S. Modern Quantum Chemistry: Introduction to Advanced Electronic Structure Theory. (Dover Publications, 1996).
47. Chen, C. J. Introduction to scanning tunneling microscopy. (Oxford University Press, 1993).ty Press, 1989).
48. Kohn, W. & Sham, L. J. Self-consistent qquations including exchange and correlation effects. *Physical Review* **140**, (1965).
49. Parr, R. G. & Yang, W. *Density-functional theory of atoms and molecules*. (Oxford University Press, 1989).
50. Hohenberg, P. & Kohn, W. Inhomogeneous electron gas. Physical Review 136, (1964).
51. Becke, A. D. Density-functional exchange-energy approximation with correct asymptotic-behavior. Phys Rev A 38, 3098-3100 (1988).

52. Perdew, J. P. & Wang, Y. Accurate and simple analytic representation of the electron-gas correlation-energy. Phys Rev B 45, 13244-13249 (1992).
53. Perdew, J. P. et al. Atoms, molecules, solids, and surfaces - applications of the generalized gradient approximation for exchange and correlation. Phys Rev B 46, 6671-6687 (1992).
54. Perdew, J. P., Burke, K. & Ernzerhof, M. Generalized gradient approximation made simple. Phys Rev Lett 77, 3865-3868 (1996).
55. Lu, Z.; Demianets, I.; Hamze, R.; Terrile, N. J.; Williams, T. J. A prolific catalyst for selective conversion of neat glycerol to lactic acid. ACS Catal. 2016, 6, 2014−2017.
56. Finn, M.; Ridenour, J. A.; Heltzel, J.; Cahill, C.; VoutchkovaKostal, A. Next-generation water-soluble homogeneous catalysts for conversion of glycerol to lactic acid. Organometallics 2018, 37, 1400− 1409.influence of structure, ligand donor, strength and counter ion on catalytic activity. Green Chem. 2009, 11, 1610−1617.
57. Viciano, M.; Mas-Marzá, E.; Sanaú, M.; Peris, E. Synthesis and reactivity of new complexes of rhodium and iridium with bis- (dichloroimidazolylidene) ligands. Electronic and catalytic implications of the introduction of the chloro substituents in the NHC rings. Organometallics 2006, 25, 3063−3069.
58. Lux, S.; Siebenhofer, M. Synthesis of lactic acid from dihydroxyacetone: use of alkaline-earth metal hydroxides. Catal. Sci. Technol. 2013, 3, 1380−1385.
59. Laurenczy, G.; Joó, F.; Nádasdi, L. Formation and characterization of water-soluble hydrido-ruthenium(II) complexes of 1,3,5- triaza-7-phosphaadamantane and their catalytic activity in hydrogenation of CO2 and HCO3 − in aqueous solution. Inorg. Chem. 2000, 39, 5083−5088.
60. Erlandsson, M.; Landaeta, V. R.; Gonsalvi, L.; Peruzzini, M.; P h i l l i p s , A. D. ; D y s o n , P . J . ; La u r e n c z y , G. (Pentamethylcyclopentadienyl)iridium-PTA (PTA = 1,3,5-triaza-7-phosphaadamantane) complexes and their application in catalytic water phase carbon dioxide hydrogenation. Eur. J. Inorg. Chem. 2008, 2008, 620−627.
61. Kovács, G.; Schubert, G.; Joó, F.; Pápai, I. Theoretical investigation of catalytic HCO3 − hydrogenation in aqueous solutions. Catal. Today 2006, 115, 53−60.
62. Fillman, K. L.; Przyojski, J. A.; Al-Afyouni, M. H.; Tonzetich, Z. J.; Neidig, M. L. A combined magnetic circular dichroism and density functional theory approach for the

elucidation of electronic structure and bonding in three- and four-coordinate iron(II)-N-heterocyclic carbene complexes. Chem. Sci. 2015, 6, 1178−1188.
63. Mata, J. A.; Chianese, A. R.; Miecznikowski, J. R.; Poyatos, M.; Peris, E.; Faller, J. W.; Crabtree, R. H. Reactivity differences in the syntheses of chelating N-heterocyclic carbene complexes of rhodium are ascribed to ligand anisotropy. Organometallics 2004, 23, 1253− 1263.
64. Leung, C. H.; Incarvito, C. D.; Crabtree, R. H. Interplay of linker, N-substituent, and counterion effects in the formation and geometrical distortion of N-heterocyclic biscarbene complexes of rhodium(I). Organometallics 2006, 25, 6099−6107.